Computational Design of Nanostructured Materials with Renewable Energy Applications

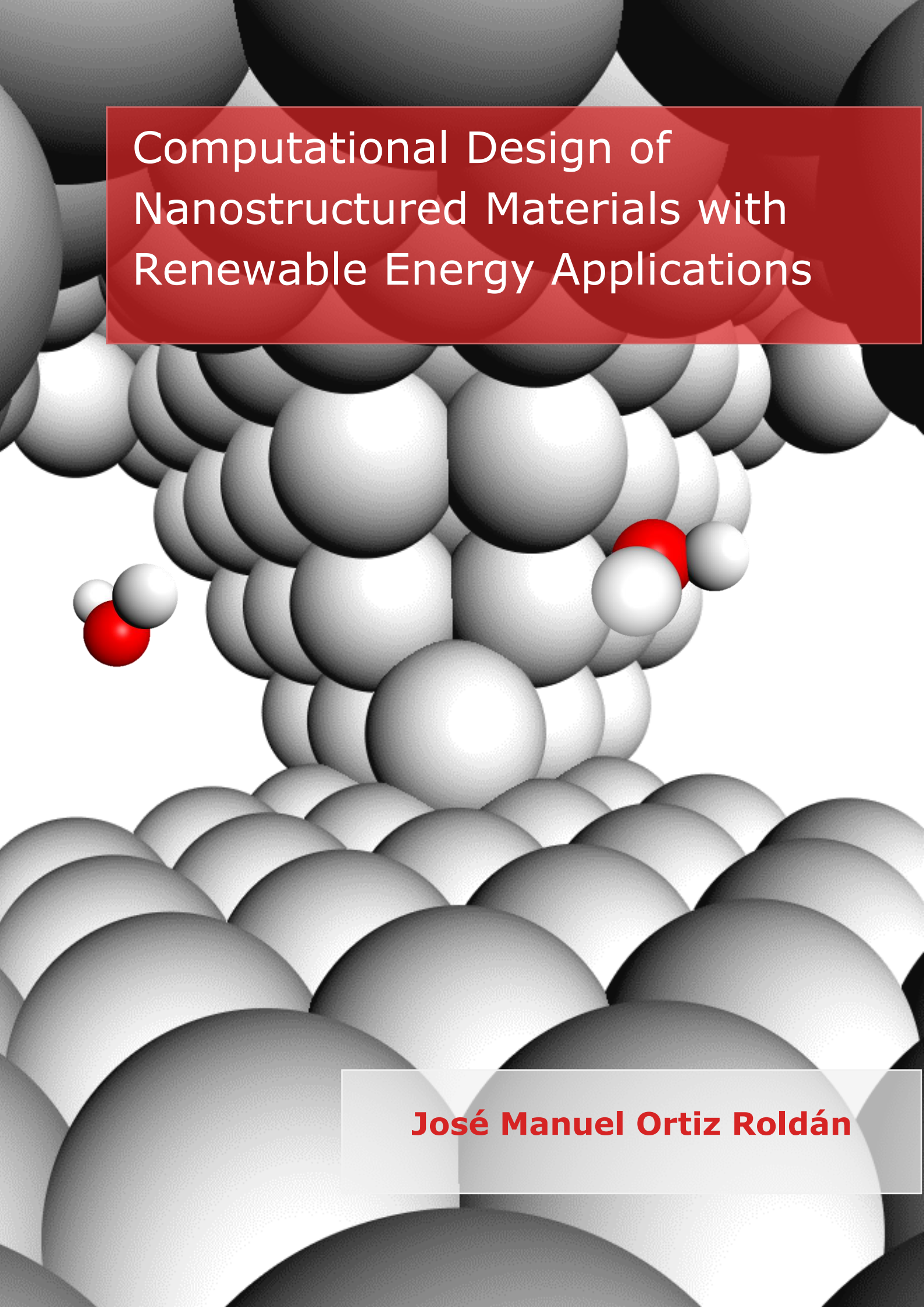

José Manuel Ortiz Roldán

Computational Design of Nanostructured Materials with Renewable Energy Applications

by

José Manuel Ortiz Roldán

UNIVERSIDAD PABLO DE OLAVIDE SEVILLA

Department of Physical, Chemical, and Natural Systems

Supervisors

Said Hamad

Dr. University Pablo de Olavide

Sofía Calero

Prof. University Pablo de Olavide

to obtain the degree of Doctor

Seville, FEBRUARY 2021

ISBN: 978-84-09-25978-6

PhD Supervisors

Prof. Dr. Said Hamad

Prof. Dr. Sofía Calero

Pablo de Olavide University: Department of Physical, Chemical and Natural Systems

Examination Committee

Prof. Dr. Norge Cruz Hernández

University of Seville, Department of Physical Chemistry, Faculty of Chemistry

Prof. Dr. Stefan T. Bromley

University of Barcelona: Dept. de Ciencia de Materials i Química Física & Institute of Computational and Theoretical Chemistry (IQTCUB)

Dr. Neyvis Almora Barrios

University of Valencia: Inorganic Chemistry / Institute of Molecular Science (ICMol)

The research reported in this thesis was carried out at the Department of Physical, Chemical and Natural Systems, University Pablo de Olavide (Seville, Spain), with financial support from the European Research Council -ERC Consolidator Grant- (ERC2011-StG-279520-RASPA), from the Spanish "Ministerio de Economía y Competitividad" -MINECO- (DPI2015-67667-C3-2-R), Spanish "Ministerio de Educación, Cultura y Deporte" (FPU14/01094) and from the Andalucía Region "Junta de Andalucía" -Proyecto de Excelencia-. This dissertation has been supported with a predoctoral fellowship from the Spanish "Ministerio de Educación, Cultura y Deporte".

Contents

Summary

This thesis studies the viability of various materials as key pieces in the construction of thermosolar power plants as well as for the storage of solar energy. As these materials are exposed to extreme pressure and temperature cycles, it is important to study their behavior under these conditions. To do this, we have used different techniques with classical and quantum calculations at the molecular level. These calculations are essential to understand the structural behavior of materials as well as to design and predict the behavior of new materials.

The purpose of the thesis is divided into two parts clearly related to each other: (1) to develop new methods to fit force fields of relevant materials in the energy plan, starting from the electronic density computed with DFT and avoiding the numerical dependence of the parameters of the potentials, and (2) design new nanostructured materials that can improve energy efficiency overcoming the adverse weather conditions of solar thermal power plants, using, where possible, models of force fields improved with our new methodology.

The thesis is divided into six chapters covering the following topics:

Chapter 1. In this chapter we begin with a summary of the thesis and continue presenting each and every one of the methods and materials used. We also present the theoretical basis behind this study, specific and detailed methodology as well as hardware and software specifications used for all analyzes.

Chapter 2. We developed a new method to fit the parameters of an interatomic potential for nickel-chromium alloys, improving the prediction of the structural properties of these materials. To do this, we have designed an algorithm that carries out a series of iterations, in which the parameters of an existing potential are fitted, in order to optimize them based on a series of experimental observables.

As an application, we study different structural properties of alloys with different concentrations of nickel-chromium, as well as nanoparticles of different sizes using the developed potential. We include at the end an example of the possible sintering of pairs of nanoparticles of this material.

Chapter 3. We improve the fitting method developed in Chapter 2 and the prediction of the properties of metallic alloys. The improvement resides in the quantum study of the electron density of these materials, from which we fit the parameters of the classical potentials corresponding to said density. The use of ab-initio observables represents a qualitative advance, since obtaining the force fields is not subject to the value of the experimental observables. In addition, we expanded the composition of the metallic alloys studied by adding iron and molybdenum to the model, with the intention of getting as close as possible to the composition of INCONEL 625.

Chapter 4. This chapter is the first of two focused on the search for new energetic materials. We have proposed, from a theoretical point of view, a new ordered nanoporous metal using as a model Metal-Organic Frameworks (MOFs), MOFs with modified ligands, zeolites and cristobalites, substituting SiO4 tetrahedra for supertetrahedra. The process is simple, using a program written in FORTRAN, we have filled the pores of these materials with metal and we have removed the original structure. We have performed 100 nanosecond molecular dynamics at different temperatures to verify that the ordered

nanoporous metals are stable. For these simulations, we have used some force fields from the literature in addition to those developed by us in the previous chapters.

The predictive power of this study is useful from an experimental point of view, since it relates the limiting diameter of the pores as a function of the stability of the new materials. The diffusion of relevant molecules in various fields such as water and xylene is studied as an application of these materials.

Chapter 5. We continue with the creation of new materials presenting one composed of cubic silicon carbide nanoparticles in an amorphous silicon matrix, as an alternative to metallic alloys, due to the high resistance of this type of ceramics to temperature changes. To do this, we have studied simple structures of cubic, hexagonal and amorphous silicon carbide with a series of potentials to determine which of them best models the structural properties compared to existing experiments. Once this was done, we studied two composite materials, (1) flat interfaces of cubic silicon carbide versus amorphous silicon and (2) nanoparticles arranged within matrices of amorphous silicon. We have studied both types with different sizes to observe their behavior based on their densities.

This study was complemented on the microscopic and macroscopic scale. On the first one, the mechanical properties of these materials were studied by performing microstructural lattice simulations. On the second one, to complete the upscaling approach, we have created ceramic tubes for receivers of thermo-solar power plants, seeing their temperature distribution based on their thickness.

Chapter 6. We discuss the conclusions of the study carried out and focus on the directions this work could take in the future.

Resumen

Esta tesis estudia la viabilidad de varios materiales como piezas clave en la construcción de centrales termosolares así como para el almacenamiento de energía solar. Como estos materiales están expuestos a ciclos de presión y temperatura extremos, es importante estudiar el comportamiento de los mismos en dichas condiciones. Para ello, hemos utilizado diferentes técnicas con cálculos clásicos y cuánticos a nivel molecular. Dichos cálculos son fundamentales para comprender el comportamiento estructural de los materiales así como para diseñar y predecir el comportamiento de nuevos materiales.

El propósito de la tesis está dividido en dos partes claramente relacionadas entre sí: (1) desarrollar nuevos métodos para ajustar campos de fuerza de materiales relevantes en el plano energético, partiendo de la densidad electrónica computada con DFT y evitar la dependencia numérica de los parámetros de los potenciales, y (2) diseñar nuevos materiales nanoestructurados que puedan mejorar la eficiencia energética superando las adversidades climatológicas de las centrales termosolares, usando en los casos posibles, los modelos de campos de fuerza mejorados con nuestra nueva metodología.

La tesis está dividida en seis capítulos cubriendo los siguientes temas:

Capítulo 1. En este capítulo comenzamos con un resumen de la tesis y seguimos presentando todos y cada uno de los métodos y materiales utilizados. También presentamos la base teórica detrás de este estudio, metodología específica y detallada así como especificaciones de *hardware* y *software* utilizado para todos los análisis.

Capítulo 2. Desarrollamos un método nuevo para ajustar los parámetros de un potencial interatómico para aleaciones de níquel-cromo, mejorando la predicción de las propiedades estructurales de dichos materiales. Para ello, hemos diseñado un algoritmo que lleva a cabo una serie de iteraciones, en las que se ajustan los parámetros de un potencial ya existente, para optimizarlos en función de una serie de observables experimentales.

Como aplicación, estudiamos diferentes propiedades estructurales de aleaciones con diferentes concentraciones de níquel-cromo, así como nanopartículas de diferentes tamaños utilizando el potencial desarrollado. Incluimos al final un ejemplo de la posible coalescencia de parejas de nanopartículas de dicho material.

Capítulo 3. Mejoramos el método de ajuste desarrollado en el capítulo 2 y con ello la predicción de las propiedades de las aleaciones metálicas. Dicha mejora reside en el estudio cuántico de la densidad electrónica de estos materiales, a partir de la cuál, ajustamos los parámetros de los potenciales clásicos correspondientes a dicha densidad. El uso de observables *ab-initio* supone un avance cualitativo, ya que la obtención de los campos de fuerza no está sujeto al valor de los observables experimentales. Además, ampliamos la composición de las aleaciones metálicas estudiadas añadiendo hierro y molibdeno al modelo, con la intención de acercarnos lo máximo posible a la composición del INCONEL 625.

Capítulo 4. Este capítulo es el primero de los dos centrados en la búsqueda de nuevos materiales energéticos. Hemos propuesto, desde un punto de vista teórico, un nuevo metal microporoso y ordenado usando como modelo Enrejados Metalorgánicos (MOFs de sus siglas en inglés), MOFs con ligandos modificados, zeolitas y cristobalitas sustituyendo los tetrahedros de SiO_4 por supertetrahedros. El proceso es simple, utilizando un programa escrito en FORTRAN, hemos llenado de metal los poros de dichos materiales

y hemos eliminado la estructura original. Hemos realizado dinámicas moleculares de 100 nanosegundos a difernentes temperaturas para comprobar que los metales microporosos ordenados son estables. Para dichas simulaciones, hemos utilizado algunos campos de fuerza de la literatura además de los desarrollados por nosotros en los capítulos anteriores. El poder predictivo de este estudio, es útil desde el punto de vista experimental, ya que relaciona el diámetro limitante de los poros en función de la estabilidad del material. La difusión de moléculas relevantes en diversos campos como el agua y el xileno es estudiada como aplicación de dichos materiales.

Capítulo 5. Continuamos con la creación de nuevos materiales presentando uno compuesto de nanopartículas de carburo de silicio cúbico en una matriz de silicio amorfo, como alternativa a las aleaciones metálicas. Para ello, hemos estudiado estructuras simples de carburo de silicio cúbico, hexagonal y silicio amorfo con una serie de potenciales para determinar cuál de ellos modela mejor las propiedades estructurales en comparación con los experimentos existentes. Una vez hecho esto, estudiamos dos materiales compuestos, (1) interfaces planas de carburo de silicio cúbico frente a silicio amorfo y (2) nanopartículas ordenadas en el seno de matrices de silicio amorfo. Ambos tipos han sido estudiados con diferentes tamaños para observar su comportamiento en función de sus densidades.

Dicho estudio ha sido complementado en la escala microscópica y macroscópica. En la escala microscópica se han estudiado las propiedades mecánicas de dichos materiales realizando simulaciones de red microestructural. En la macroscópica, como aplicación, hemos escalado hasta la creación de tubos cerámicos para recibidores de centrales termo-solares, viendo la distribución de temperaturas de los mismos en función de sus grosores.

Capítulo 6. Discutimos las conclusiones del estudio llevado a cabo y ponemos el foco en las direcciones que este trabajo podría tomar en el futuro.

1. Introduction

1.1. Materials

1.1.1. Nickel-based alloys

An alloy is a combination of metals or a combination of metals with non-metallic elements in which the properties of metals, such as electrical conductivity and ductility, are not lost. The applications of metal alloys are countless. Modifying the properties of a metal by adding other metallic and non-metallic elements has been done for centuries, such as mixing iron with silicon and carbon to obtain steel, or mixing gold and silver to obtain white gold. The alloys can be formed by a solid solution of metallic elements, where each grain has the same composition, or by a mixture of different metal phases. Thanks to the science of materials, the improvement of the properties of metal alloys has been considerable. In the last century, metal alloys have been used in buildings, cars, surgery tools, electronics, in the aerospace industry and in almost any industry[1–5].

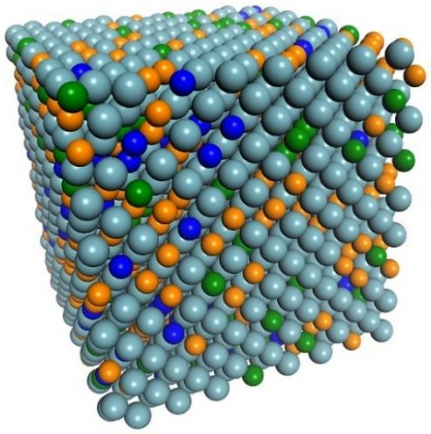

Figure 1. 1. Perspective representation of a Ni-based alloy with Cr, Mo and Fe in solid solution.

Its use is due, on the one hand, to lowering the cost of materials without losing the initial metallic properties, or on the other hand, in order to improve its properties that pure metals lack.

In the field of renewable energies, alloys are used for their structural properties and for their high resistance to thermal cycles. In this sense, we have focused on nickel based alloys. In chapter 2 and chapter 3 we have developed two ways of fitting potentials that describe their behavior. In Chapter 4, as an application of what was obtained in Chapter 2 and 3, the behavior of the new ordered nanoporous metals that we have designed. The main objective in chapters 2 and 3 has been to get as close as possible to modeling the behavior of the Inconel 625. In chapter 2, we have worked with the two main metals of the alloy, Nickel and Chrome, while in the next chapter we have added the following two in percentage, iron and molybdenum. The name of this Nickel-based alloy is commercial, as are other alloys such as Hastelloy and Haynes that are also known by their trade name.

Nickel based alloys present high corrosion and thermal shock resistance properties in severe conditions[6]. They are mainly used for Oil & Gas, Chemical and Power industries[7], in the most aggressive parts in flue gas desulfurization units, jet engines and gas turbine blades. In addition, nickel alloys have a low-expansion.

Alloys can be designed to have a very low thermal expansion or display uniform and predictable expansion over

certain temperature ranges, which makes them perfect candidates for solar thermal receivers. New greener, environmentally suitable and cheaper methods to synthesize nickel nanoparticles are being investigated[8]. Due to its properties, the main applications of nickel nanoparticles are as anode of solid oxide fuel cells, automotive catalytic converters, coatings, plastics, nanowires, nanofibers and textiles, magnetic fluid, catalyst propellant and sintering additive[9]. In most such applications, sintering is a desirable effect[10–12]. Due to the importance of having a deep understanding of the dynamics of nanoparticles, in Chapter 2 we have proven that it occurred between two nanoparticles.

1.1.2. Ordered Nanoporous metals

In chapters 4 and 5 we focus on the search for new materials with energy applications. We have already talked about the benefits of metallic materials due to their high resistance to corrosion and thermal cycles. On the other hand, the different types of nanoporous materials that have been designed in recent years[13–16], offer a wide range of applications depending on the material and the size of its pores[17–19]. The large amount of internal surface in such small volumes makes them of great interest in catalysis and molecular separation. The research in natural an designed zeolites and metal-organic frameworks (MOFs) has increased substantially in the last decade because the design of new materials of these characteristics is an upward value in the industry. MOFs are a class of cristalline materials. They are combinations of metallic centers connected by organics linkers. These assemblies generate an organized three dimensional network of channels and cages.

The first existing porous metals came from dealloying[20,21]. The pores created with this technique were of various sizes and messy, since they depend on how the different elements are located. Even so, its versatility for having the properties of metals and porous materials is huge[22,23]. The main application of these metallic foams is that of electrode in NiMH and NiCd batteries. In addition, gold metallic foams have important applications due to their high resistance to radiation with a low weight[24].

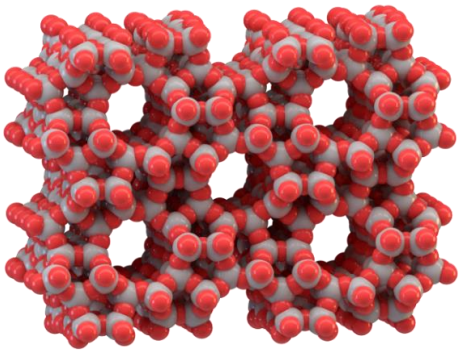

Figure 1.2. Orthogonal CPK representation of a zeolite catalyst.

In the chapter 4 of this thesis, we propose a new class of nanoporous metal which we have called Ordered Nanoporous Metals (ONMs). The way in which ordered pores of microscopic size have been achieved is using MOFs, zeolites and cristobalites as template, we have filled them with metal and then we have removed

Figure 1.3. Real photography of a foamed aluminum block.

the original template, leaving a metal structure with pores of controlled and ordered sizes. We have done this filling and emptying with a computer program written in Fortran. In some cases, to get micropores, we have substituted the tetrahedra of SiO4 with supertetrahedrons. We have verified with two different potentials and with simulations of up to 100 nanoseconds that several of these structures are stable at temperatures of up to 1200 K.

In the literature, we can find that this is possible and has recently been carried out[25]. That is why the invention of these materials represents a breakthrough in the field of porous materials. On the one hand, we have the properties of metallic materials, and on the other, we can design these materials with custom pore sizes for different applications, as is done with MOFs and zeolites. As we have studied, stability depends to some extent on the Pore Limiting Diameter (PLD), so a material of any desired pore size cannot be designed. However, there is a wide range of possibilities yet to be explored.

1.1.3. Silicon carbide structures

Silicon carbide (SiC) is a semiconductor material, which contains silicon and carbon in equal amounts. SiC is used in space stations, advanced fighter aircraft, fusion reactors and the petroleum and automotive industries[26–28]. SiC is a fundamental material for semiconductor technologies and for their future innovations because it is a wide band gap 2.4–3.3 eV semiconductor, with high-power and high-frequency electronic device applications in radiation and high-temperature environments[29–31]. SiC systems are currently being tested for its use in solar thermal receivers. For the most demanding applications, materials must be resistant to thermal shock, impervious, even at high differential pressures (20 bar inside the tubes), commercially available, and it must have proper mechanical properties as high fatigue resistance[32]. Materials presenting high tensile strength σ but small Poisson's ratio ν, modulus of elasticity E and coefficient of thermal expansion α will have high thermal shock resistance as we can see if we look to the expression:

$$R_T = K\,\sigma\,(1-\nu)\,E^{-1}\,\alpha^{-1} \qquad (1.1)$$

Silicon carbide is a unique material, with more than 250 polymorphs of silicon carbide being identified. The polymorphs of SiC include a large family of similar crystalline structures called polytypes. They are variations of the same chemical compound that are identical in two dimensions and differ in the third one. Thus, they can be viewed as layers stacked in a certain sequence. The stacking sequence of those configurations defines the crystal structure, where the unit cell is the shortest periodically repeated sequence of the stacking sequence. For the applications discussed above, β-SiC is of considerable interest in addition to the 6H form of α-SiC.

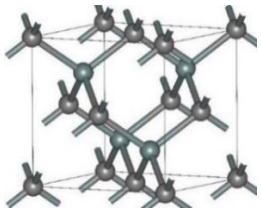

(β) 3C-SiC

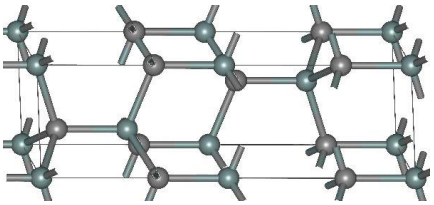

4H-SiC

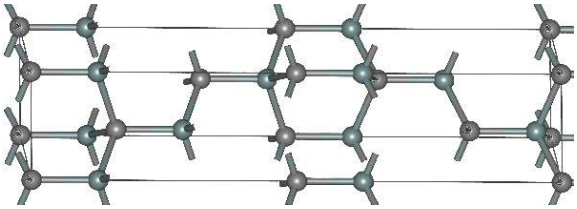

(α) 6H-SiC

Figure 1.4. Orthographic ball and stick representation of the three main SiC structures, 3C-SiC, 4H-SiC and 6H-SiC.

Si-SiC structures as Silit SK, are amorphous silicon infiltrated silicon carbide (Si-SiC) materials, constituted by quite large grains inside a matrix. It is clear that grains are silicon carbide while matrix is amorphous silicon (a-Si). The experiments show that Silit SK is constituted mostly by a mixture of amorphous silicon and alpha (hexagonal phase) and beta (cubic phase) SiC. Silit SK is a well sintered ceramic with lack of pores. According to that, we will study 3C-SiC, 6H-SiC, a-Si and we will focus on the interaction between 3C-SiC and a-Si in two specific cases: a plane interface between them, and well-ordered 3C-SiC NP inside an a-Si matrix.

The amount of existing interatomic potentials that permit us to study the structural and thermal properties of SiC is very large[33–37]. The different nature of these force fields makes them appropriate to study certain characteristics but not all of them. Even when we talk about thermo-structural properties, some force fields just fit correctly for a short range of temperatures. We analyzed the behavior of the simpler structures through different thermo-structural properties like heat capacity, thermal expansion, their melting point and strain-stress curves at different temperatures. We have used five different force fields, two of them follow the 2nd Nearest Neighbors - Modified Embedded Atom Method (2NN-MEAM) and three of them are Tersoff type potentials. We will choose the most accurate potential, according to the experimental data, to study the mixed structures.

In this thesis we propose a new type of material based on SiC. Said material is formed by cubic SiC nanoparticles within an amorphous silicon matrix in which we combine the properties of both materials. These materials could have different densities if we modify the size of the nanoparticles, which would give us a wide range of properties, ranging from the properties of cubic SiC to the properties of amorphous Si.

1.2. Methodology

This section describes the techniques employed in the thesis. The most important factor in simulation is the way in which the energy of the system is calculated. Calculations can be based on the use of interatomic potentials (IP) to model the interaction between the atoms of the system. Another option is to obtain the electronic structure of the system by solving Schrödinger's equation, with any of the plethora of approximations available. The method most commonly used approximation to solve Schrödinger's equation is Density Functional Theory (DFT).

Once we have decided how to calculate the energy of the system, we can then perform several types of simulations, such as Energy Minimisations and Molecular Dynamics simulations (MD). Molecular Dynamics simulations were used to calculate temperature-dependent properties of the different structures studied, as well as dynamical properties. Energy minimizations were employed to determine the most stable structures of the systems, as well as to fit the parameters of the force fields, and thus obtain a better description of the properties.

1.2.1. Statistical Mechanics and Molecular Mechanics Simulations

The work carried out in this thesis is based on the framework of statistical mechanics. This allows to work with systems with a large number of atoms. Statistical mechanics provides methods with which to connect the behavior of a large set of particles with properties that can be observed at the macroscopic scale, such as the temperature or volume of the system.

Molecular simulations are fundamental when reproducing the behavior of systems from an atomic point of

view. It is important to obtain a realistic model that correctly describes the interactions existing in the systems. In our case, we are interested in reproducing observables that can be measured experimentally. We model various systems to design new materials with interesting characteristics from the point of view of the renewable energy industry.

We call simulations to all those processes that use interatomic potentials (classical simulations) or electronic structure methods (quantum simulations) for the calculation of physical properties of materials. In classical simulation, interatomic potentials are used to compute the interaction energy between each of the atoms that compose the system, while in quantum simulation, Schrödinger's equation is solved numerically, with different levels of approximation, to obtain the energy of the system. It is fair to say that, although in theory quantum simulation describes more accurately what happes in reality, classical simulation is very useful in large and long-term systems due to the low computational cost, and in some cases it even provides better description of the systems that quantum calculations.

To include the influence of time in the simulations, we use the Principle of Least Action, which gives rise to Hamilton's equations of motion:

$$\dot{q}_i = \frac{\partial H}{\partial p_i}, \qquad \dot{p}_i = -\frac{\partial H}{\partial q_i} \tag{1.2}$$

for all $i = 1, \dots, N$, where q_i are generalised coordinates, p_i are their corresponding momenta, N the number of particles of the system and H is the Hamiltonian, defined as:

$$H = K + U \tag{1.3}$$

where K is the kinetic energy and U is the potential energy. The total potential energy can be described as an expansion in bonded and non-bonded interactions:

$$U(\vec{r}, \vec{\theta}, \vec{\phi}) = \sum U_{nb}(r) + \sum U_r(\vec{r}^N) + \sum U_\theta(\theta) + \sum U_\phi(\phi) \tag{1.4}$$

Where the terms are non-bonded, bonds, bends and dihedral potential energies, respectively.

To obtain the coordinates and the momenta of a set of atoms, the equations (1.1) are integrated, thus obtaining the evolution of a dynamic system.

A statistical ensemble is the set of all possible replicates that represent the different microstates of a system. An statistical ensemble contains several conservation laws and physical constrains that must be satisfied in the macrostate, as for example the energy conservation:

$$\delta(H(x) - E) \tag{1.4}$$

Macroscopic constraints lead to several ensembles, with particular statistical characteristics. Some thermodynamic ensembles that we use are:

- **Microcanonical ensemble or NVE ensemble**: it describes an isolated and equilibrated system with a fixed number of particles N, volume V and Energy E.
- **Canonical ensemble or NVT ensemble**: it describes a closed (in order to be in statistical equilibrium) system with a fixed number of particles N, volume V and temperature T.
- **Macrocanonical or Grand Canonical ensemble or μVT ensemble**: it describes an open system with a fixed volume V and in equilibrium with a reservoir of particles (fixed chemical potential μ and temperature T).
- **Isothermal-isobaric ensemple or NPT ensemble**: it describes a system with a variable volume V. It allows fluctuations in the pressure P in a closed system (fixed number of particles N and temperature T).

The density of a statistical ensemble is always, as we have seen, an integral of motion. This can be expressed with Liouville's equation:

$$\frac{d\rho}{dt} \equiv \frac{\partial \rho}{\partial t} + \{\rho, H\} = 0 \qquad (1.5)$$

By solving stationary solutions of equation (1.5), we obtain the stationary probability density $\rho(x_t)$.

Table 1.1 compiles the expressions that provide the probability densities in all the ensembles.

Table 1.1: Partition and probability density functions of selected ensembles.

Ensemble	**Partition function Z and probability density $\rho(x, V)$ where $x \equiv \{\vec{q}^N\}$ and $s \equiv \{\vec{q}^N, \vec{p}^N\}$**
Micro canonical	$\Omega(N,V,E) = \frac{1}{h^{3N}N!}\int ds\, \delta(E - H(s))$ $\rho(s,V) \propto \delta(E - H(s))$
Canonical	$Z = Q(N,V,T) = \frac{V^N}{\Lambda^{3N}N!}\int dx e^{-\beta U(x)}$ $\rho(x,V) \propto e\text{^} - \beta U(\S)$
Gran canonical	$Z = \Xi(\mu,V,T) = \sum_{N=0}^{\infty} \frac{V^N e^{\beta\mu N}}{\Lambda^{3N}N!}\int dx\, e^{-\beta U(x)}$ $\rho(x,V) \propto \frac{V^N e^{\beta\mu N}}{\Lambda^{3N}N!} e^{\beta U(x)}$
Isothermal-isobaric	$Z = \Delta(N,P,T) = \frac{\beta P}{\Lambda^{3N}N!}\int dV\, V^{N+1} e^{-\beta PV}\left(\int dx\, e^{-\beta U(x)}\right)$ $\rho(x,V) \propto V^{N+1} e^{-\beta PV} e^{-\beta U(x)}$

Once we know this, the number of microstates that are compatible with a macrostate is given by:

$$\Omega = \int dx_0\, \rho(x_0) = \int dx_t\, \rho(x_t) \qquad (1.6)$$

that is the Partition Function, and the expected value of a generic observable A is defined as:

$$\langle A \rangle = \frac{1}{\Omega}\int dx\, A(x)\rho(x) \qquad (1.7)$$

Both the Partition Function and the observable are time independent.

1.2.2. Interatomic Potential Techniques

Systems are composed of formally charged ions that interact with all the others by means of many kinds of forces when we employ IP methods. These forces depend only upon the atomic positions, so they do not depend upon the atomic velocities or accelerations (as, for instance, magnetic forces would do), and of course, there is no explicit description of the electronic structure of the system. For these reasons, the forces can be fully derived from a potential energy function, which has two main contribution, namely the long-range interactions (*i.e.* the electrostatic interaction between the charges of all the ions) and a short-range potential:

$$V_{Total}(\vec{r}_1,\ldots,\vec{r}_N) = \sum\left(\frac{1}{4\pi\varepsilon_o}\frac{q_i q_j}{r_{ij}}\right) + V_{Short-range}(\vec{r}_1,\ldots,\vec{r}_N) \qquad (1.8)$$

where q_i and q_j are the charges of the interacting ions i and j, r_{ij} the distance between them and $\vec{r}_1,\ldots,\vec{r}_N$ are the positions of the N atoms.

The electrostatic term is not the only one between ions. There are many other interactions in the crystal, referred to collectively as short-range interactions. The short-range energy is usually expressed as:

$$V_{Short-range}(\vec{r}_1,\ldots,\vec{r}_N) = \sum_{ij} V_{ij}(r_{ij}) + \sum_{ijk} V_{ijk}(r_{ijk}) + \sum_{ijkl} V_{ijkl}(r_{ijkl}) + \ldots \qquad (1.9)$$

where V_{ij} refers to all two-body interactions, V_{ijk} to three-body interactions, V_{ijkl} to four-body interactions, and so on.

The most important contribution to the short-range interactions comes from the two-body interactions. There are many different potentials to model these two-body interactions. The best known of all is the Lennard-Jones potential:

$$V_{ij}(r_{ij}) = \frac{A}{r^n_{ij}} - \frac{B}{r^m_{ij}} \qquad (1.10)$$

where A and B are fitted parameters and n and m are integer numbers.

The first term models the repulsive interactions due to the Pauli forces, and the second one the attractive interactions due to the Van der Walls dispersion forces. At short distances the repulsive forces become much higher than the attractive ones. It implies that n must be greater than m. The most frequently used values for n and m are 12 and 6 respectively. The r^{-6} dependence of the attractive forces has a physical background; it can be obtained from theoretical studies of the dispersion energy.

There is an energy minimum distance, r_m, dependant of the fitted parameters A and B. In the proximity of the minimum an exponential function could describe better the repulsive part of the potential. The Buckingham potential uses the r^{-6} term to model the dispersion forces, but the repulsive forces are modelled with an exponential function:

$$V_{ij}(r_{ij}) = A\exp\left(\frac{-r_{ij}}{\rho}\right) - \frac{C}{r^6_{ij}} \qquad (1.11)$$

where A,ρ and C are fitted parameters

Buckingham potentials generally perform better for ionic systems than Lennard-Jones potentials. In part, it could be due to the fact that it has three fitted parameters, one more than Lennard-Jones.

There are other terms, also important in the contribution to short-range energy, such as three-body and four-body energy. However, as they are not used in this thesis, we will not expand more information about them.

On the other hand, in terms of metal-metal interaction and between metalloids such as silicon, different potentials are used in the literature. In this thesis, we used potentials of type Embedded Atom Method (EAM), to be more precise, they have been Modified EAM (MEAM). In this type of interatomic potential, two-body energy is added with a many-body energy that represents the electronic density of the systems. In the MEAM used here, 2nd Nearest Neighbor MEAM versions (2NN-MEAM) have been used that include interactions to the second nearest neighbors, increasing the computational cost but significantly improving the models.

EAM type potentials have the following form:

$$E_{Total} = \frac{1}{2}\sum_{i,j}\phi_{ij}(r_{ij}) + \sum_{i,j}F_i(\rho_i) \qquad (1.12)$$

$$\rho_i = \sum_{j\neq i}\Psi_{ij}(r_{ij}) \qquad (1.13)$$

Where energy is described by a summation of two-body terms plus a summation of many-body terms. The first part depends directly on the distance between atoms while the second part depends on the electronic density of the system, modeled by a function.

1.2.3. Density Functional Theory

In this thesis, we used Density Functional Theory to obtain the energy, as well as the electronic density of the systems. This energy provides useful observables when fitting the force fields. In the case of metals, the models describe by means of equations the body-body interactions as well as the behavior of their electronic band.

The basis of the electronic structure techniques is Schrödinger's equation: $\widehat{H}|\Psi\rangle = \epsilon|\Psi\rangle$. It has all the information needed for a complete quantum description of a time-independent physical system. The Hartree-Fock method[38–42] gives an

approximate solution, but does not account for electronic correlation. Other posterior techniques include correlation effects but these methods are very time consuming and are only applicable to relatively small systems.

Hohenberg and Kohn[43] derived a method for solving Schrödinger's equation, proving that the external potential $V(r)$ and the total number of electrons N are uniquely determined by the electronic density $\rho(r)$ of the ground state of the system. All properties of a physical system can be calculated if $\rho(r)$ is known. One of the most important results of their work was that there is a universal functional that allows calculation of the energy of a quantum mechanical system from this electronic density. For a given potential $V(r)$ the energy of the fundamental state is written as:

$$E[\rho(\vec{r}] = \int V(\vec{r})\rho(\vec{r})dr + F[\rho(\vec{r})] \qquad (1.14)$$

where $E[\rho(\vec{r})]$ is a functional of $\rho(\vec{r})$. $F[\rho(\vec{r})]$ refers to the sum of the kinetic, Coulombic electron-electron and exchange-correlation energies. Hohenberg and Kohn[43] also extended the Variational Principle to this function: the energy $E[\rho(\vec{r})]$ calculated with a given electronic density $\rho(\vec{r})$ is higher than the energy of the real system E_0. So, $E[\rho(\vec{r})]$ equals E_0 only when $\rho(\vec{r})$ is the exact electronic density of the system. The quality of the several functionals proposed in the last years has increased widely.

1.2.4. Energy minimisations

When we talk about minimizing the energy of a system, we refer to finding the most probable configuration, in terms of energy, in which our system is located. Since there is no velocity taken into account for the atoms, the simulations for this type of calculations are effectively carried out at 0 K. The potential energy of the systems depends on N variables, and the following condition must be fulfilled in the minimum energy configuration:

$$\frac{\partial U(\vec{r}^N)}{\partial r_i} = 0 \qquad \forall i = 1, \dots, 3N \qquad (1.15)$$

where $U(\vec{r}^N)$ is the total potential energy of the system and N is the number of atoms.

Transition states and local minima also satisy Equation 1.6, therefore it is necessary to calculate the second derivative to distinguish between a minimum and a transition state.

The Conjugate Gradient method requires the energy and first derivative evaluations, and is the most efficient method at intermediate distances from the minimum. This method follos conjugate search directions instead of always following the force. In the LAMMPS code it is implemented the Polak and Ribiére[44] version of the algorithm:

$$\vec{x}_{n+1} = \vec{x}_n - k_n\vec{h}_n \text{ with } \vec{h}_n = \vec{\nabla}f(\vec{x}_n) + \gamma_n\vec{h}_{n-1} \qquad (1.16)$$

where

$$\gamma_n = \frac{\vec{\nabla}f(\vec{x}_n)\left(\vec{\nabla}f(\vec{x}_n) - \vec{\nabla}f(\vec{x}_{n-1})\right)^T}{\left|\left|\vec{\nabla}f(\vec{x}_{n-1})\right|\right|} \qquad (1.17)$$

The norm of the gradient is checked to ascertain whether to switch from one method to another. When the system is very close to the energy minimum, this method converges slowly. When this happens, we switch to the Newton-Raphson method[45] which makes use of the second derivatives of the energy, in order to reach rapidly the energy minimum. Newton-Raphson method approximates de objective function by a quadratic surface at each step and moves to the minimum of that surface:

$$f(\vec{x} + \Delta\vec{x}) \cong f(\vec{x}) + \vec{\nabla}f(\vec{x})^T \cdot \Delta\vec{x} + \frac{1}{2}\Delta\vec{x}^T \cdot H \cdot \Delta\vec{x}$$

$$\vec{\nabla}f(\vec{x} + \Delta\vec{x}) \cong \vec{\nabla}f(\vec{x}) + H \cdot \Delta\vec{x}$$

$$\Delta\vec{x} = -H^{-1} \cdot \vec{\nabla}f(\vec{x})$$

where $H = \frac{\partial^2 U}{\partial_{x_i}\partial_{x_j}}$ is the Hessian. This method has a computationally elevated cost. On the other hand, Rational Function Optimization introduces a step size dependent

denominator[46] which prevents the algorithm from taking large steps:

$$f(\vec{x}+\Delta\vec{x}) \cong f(\vec{x}) + \frac{\vec{\nabla}f(\vec{x})^T\cdot\Delta\vec{x}+\frac{1}{2}\Delta\vec{x}^T\cdot H\cdot\Delta\vec{x}}{1+\Delta\vec{x}^T\cdot S\cdot\Delta\vec{x}} \quad (1.18)$$

Both Newton-Raphson and Rational Function Optimization methods were used to ensure convergence to true energy. However, the second method, behaves better than the first one in the vicinity of inflextion points. The two methods are included in the GULP code[47].

1.2.5. Molecular Dynamics

In Molecular Dynamics simulations, particles move around in the system, following trajectories determined by Newton's laws. The equations derived from Newton's equations describe the motion of the atoms as a function of time:

$$m_i \frac{d^2\vec{r}_i}{dt^2} = -\vec{\nabla}_i V_{Total}(\vec{r}_1,\ldots,\vec{r}_N) \qquad \text{i=1,....,N} \quad (1.19)$$

where m_i is the mass of the i atom, r_i its position vector, N the number of atoms and $V_{Total}(\vec{r}_1,\ldots,\vec{r}_N)$ is the total potential energy of the system, as defined in Equation 1.9

These equations cannot be solved analytically, and a large number of algoritms exist for solving them numerically. In an iterative scheme, the forces they exert on one another are calculated from their positions. Based on the forces, the velocities are updated and these velocities, kept fixed for one time-step, τ, yield the new positions one time-step away. The velocity-Verlet algorithm is the most used method for integrating the equations of motion[48]. This algorithm is implemented in most simulations codes according to the following equations:

$$\vec{r}_i(t+\tau) = \vec{r}_i(t) + \vec{v}_i(t)\tau + \frac{\vec{f}_i(t)}{2m}\tau^2 + O(\tau^3) \quad (1.20)$$

$$\vec{v}_i(t+\tau) = \vec{v_i}(t) + \frac{\vec{f_i}(t)+\vec{f_i}(t+\tau)}{2m}\tau + O(\tau^3) \quad (1.21)$$

where $\vec{r_i}(t)$, $\vec{v_i}(t)$ and $\vec{f_i}(t)$ are the position, velocity and force vector at time *t*, respectively. τ is the time-step and *m* the mass of the atom i. Note that this algorithm is time-reversible. An unphysical drift in the energy appears after long integration time or as a results of the use of large time-steps, τ. To test this energy drift for a given time-step after λ integration steps, we can check the integration validity by requiring the drift is lower than a typical energetic value δ:

$$\sum_{i=1}^{\lambda}\left|1-\frac{E(i\tau)}{E(0)}\right| < \delta\lambda \quad (1.22)$$

There are several ensembles in which we can run calculations, depending on the conserved quantities: NVE, NVT, NPT, etc. In this thesis, we use the NVT and NPT ensembles. The numerical integration was performed using the Nose-Hoover equations of motion, which are designed to generate positions and velocities sampled from NVT and NPT ensembles. After equilibration, one measures the average values of properties from the trajectories of the particles. The ergodic hypothesys states that ensemble averages can be obtained from time averages. This indicates that one can follow the time evolution of the systems instead of sampling the phase space by generating microstates with a given probability. According to this, the time average value of a property can be obtained by the following expression

$$\langle A\rangle_t = \lim_{t\to\infty}\frac{1}{t}\int dt\, A(x,t) \quad (1.23)$$

where $x \equiv \{\vec{r}^N\}$. If equation (1.4) is equal to

$$\langle A\rangle = \frac{1}{\Omega}\int dx\, A(x)\rho(x). \quad (1.24)$$

the system is ergodic.

1.3. Computed Properties

1.3.1. Radial Distribution Function

The Radial Distribution Function (RDF) is a relevant structural property of the system. Given a reference particle, RDF can be defined as the normalized probability to find particles at a certain distance between r and r+dr.

The RDF of two particles A and B is defined as:

$$g_{AB}(r) = \frac{1}{<\rho_b>}\frac{1}{N_A}\sum_{i=1}^{N_A}\sum_{j=1}^{N_B}\frac{\delta(r_{ij}-r)}{4\pi r^2} \quad (1.25)$$

Where $< \rho_b >$ is the average density of the B-type particles and N_i is the number of i-tipe particles.

1.3.2. Diffusion Coefficient

Diffusion coefficient or self-diffusion coefficient is a dynamical property that accounts for the net movement of atoms or molecules from a reference state. The mean squared displacement (MSD) is based on the trajectories of the particles along the simulation time and can be used to compute the diffusion coefficient. Three dynamical regimes can be observed when plotting MSD *versus* time. At very short simulation times, the system is in the ballistic regime where the MSD is proportional to t^2. After this, the regime is controlled by the collisions between particles until they finally reach the diffusive regime, in which the MSD scales linearly with time. The self-diffusion coefficient in a 3-dimensional system can be extracted from the slope of the MSD in the diffusive regime by using the Einstein equation:

$$D_s = \lim_{t\to\infty}\frac{<\sum_i^n||r(t)-r(0)||^2>}{6t} \quad (1.26)$$

1.3.3. Elastic Constants

When we speak of elastic constants, we refer to each of the physically measurable parameters that characterize the elastic behavior of a solid. These parameters describe the relationship existing between the stresses and strains undergone by a material.

For linear elastic anisotropic bodies, the relationship between stress and strains can be expressed by a stiffness tensor given by:

$$s_{ij} = C_{ijkl}\cdot e_{kl} \quad (1.27)$$

where $\boldsymbol{s_{ij}}$ is the stress tensor, $\boldsymbol{e_{kl}}$ is the strain tensor, and $\boldsymbol{C_{ijkl}}$ is the fourth-rank constitutive tensor. In three dimensions, this tensor has 81 elements. Using Voigt notation, the tensor can be written as a $\boldsymbol{6\times 6}$ matrix and $\boldsymbol{C_{ij}}$ is now the derivative of $\boldsymbol{s_i}$ with respect to $\boldsymbol{e_j}$.

At any temperature, the calculation of these derivatives, is made by deforming the domain in one of the three directions. Once the elastic constants are determined, we compare our results with experimental results.

The isotropic bulk module *K* is the relationship between hydrostatic pressure and volumetric deformation, and is given by the following expression:

$$K = -V\frac{dP}{dV} = \frac{C_{11}+2C_{12}}{3} \quad (1.28)$$

Where P is the pressure and V the initial volume.

Young's modulus is a parameter that characterizes the behavior of an elastic material, depending on the direction in which a force is applied. For a linear and isotropic elastic material, Young's modulus has the same value for a tension as for a compression, being a constant independent of the stress provided that it does not exceed a maximum value called the elastic limit, and is always greater than zero. We can determine Young´s modulus $\boldsymbol{E}$ as follows:

$$E = \frac{\sigma}{\varepsilon} = \frac{F/S}{\Delta L/L} = \frac{(C_{11}+2C_{12})(C_{11}-C_{12})}{(C_{11}+C_{12})} \quad (1.29)$$

Where σ is the stress on the cross-sectional area of the element, $\boldsymbol{\varepsilon}$ is the strain understood as the ratio of the change in length with respect to the initial length.

Shear modulus $\boldsymbol{G}$, is defined as the ratio of shear stress to the shear strain:

$$G = \frac{F/A}{\Delta x/l} = \frac{C_{11}-C_{12}+3C_{44}}{5} \quad (1.30)$$

Where F is the force which acts, A is the area on which the force acts, Δx is the transverse displacement and l is the initial length.

Poisson's ratio $\boldsymbol{\nu}$ is a measure of the Poisson effect, the phenomenon in which a material tends to expand in directions perpendicular to the direction of compression:

$$v = \frac{C_{12}}{2(C_{12}+ C_{44})} \quad (1.31)$$

Anisotropy is the property of a material which allows it to change or assume different properties in different directions as opposed to isotropy. Anisotropy ratio A can be measured as follows:

$$A = \frac{2C_{44}+C_{12}}{C_{11}} - 1 \quad (1.32)$$

The elastic anisotropy factor is zero for an isotropic material. Any value smaller or larger than zero indicates a certain level of anisotropy, and thus measures the degree of elastic anisotropy of the crystal.

1.3.4. Coefficient of Thermal Expansion

Thermal expansion is the phenomenon where an object or body expands in reaction to being heated. Thermal expansion is most obvious in gasses and liquids but can still have a substantial effect on solids. When a body is heated, it is accepting and storing energy in its atoms in the form of kinetic energy. This expose to an increased temperature causes an atom's natural vibrations to grow stronger and more pronounced. This increase in vibration pushes against the inter-molecular forces, allowing the atoms or molecules to become farther apart and the body to grow larger.

$$\alpha = \frac{1}{L_0} \cdot \frac{\partial L}{\partial T} = \frac{1}{V_0} \cdot \frac{\partial V}{\partial T} \quad (1.33)$$

The Coefficient of Thermal Expansion α can be calculated in a specific direction or taking into account the whole volume.

1.3.5. Specific Heat Capacity

In thermodynamics, the specific heat capacity c_p of a substance is the heat capacity of a sample of the substance divided by the mass of the sample. It can be calculated as follows:

$$c_p = \frac{1}{M} \cdot \left(\frac{\partial Q}{\partial T}\right)_p \quad (1.34)$$

The specific heat often varies with temperature, and is different for each state of matter.

2. Thermostructural Behaviour of Ni-Cr Materials: Modelling Bulk and Nanoparticle Systems

The thermostructural properties of Ni-Cr materials, as bulk and nanoparticle (NP) systems, have been predicted with a newly developed interatomic potential, for Ni/Cr ratios from 100/0 to 60/40. The potential, which has been fitted using experimental data and further validated using Density Functional Theory (DFT), describes correctly the variation with temperature of the lattice parameters and the coefficient of thermal expansion, from 100 K to 1000 K. Using this potential, we have performed Molecular Dynamics (MD) simulations on bulk Ni-Cr alloys of various compositions, for which no experimental data are available. Similarly, NPs with diameters of 3, 5, 7, 10 nm were studied. We found a very rapid convergence of NP properties with the size of the systems, showing already the 5 nm NPs a thermostructural behaviour similar to that the bulk. MD simulations of two 5 nm NPs show very little sintering and thermally-induced damage, for temperatures between 300 K and 1000 K, suggesting that materials formed by agglomeration of Ni-Cr NPs meet the thermostructural stability requirements for catalysis applications.

2.1. Introduction

Metal alloys have historically been used in structural applications, due to their exceptional mechanical properties. The use of metals and metal alloys has been greatly extended during the last decades, in fields such as catalysis, medicine, engineering, electronics, etc[5]. This is possible thanks to the development of materials science, which has increased the range of properties of metallic systems. In many cases, there is an enhancement in specific properties upon alloying due to synergistic effects, and the rich diversity of compositions, structures, and properties of metal alloys and nanoalloys has led to widespread applications[1,49].

Nickel-Chromium alloys are extensively used, mainly due to their excellent resistance to high temperature oxidation and corrosion[50]. There are six main nickel-based alloy groups, where chromium is the second main component in most of them. The role of chromium in corrosion-resistant nickel alloys is to enhance the formation of passive oxide films that impede the corrosion process[6]. This capability of nickel-chromium alloys is also largely exploited in energy related applications, where safety requirements demand high resistant for high temperature and/or pressure, as for example in nuclear power systems. In this sense, austenitic nickel-chromium-based alloys are also

becoming widely extended within the aerospace industry (e.g. moving parts as rotors and blades, rocket nozzles and spacecraft shielding); chemical engineering (e.g. reactor shells, boilers or catalysts); or renewable energy (e.g. solar receivers, photovoltaic substrates) to cite a few. In fact, the development of this type of superalloys has become the core business in some metallurgical companies. As a matter of fact, these superalloys are often referred to by their commercial names (e.g. Inconel®, Hastelloy®, Haynes®, or Chronin®).

Ni and Ni-Cr nanoparticles can be used for various applications, mainly in catalysis. For instance Ni nanoparticles catalyse the reactions to produce syngas by oxy-steam reforming of methane[51], to produce hydrogen from bioethanol[52], or to perform thermal decomposition of ammonia[53]. Ni nanoparticles can also be used in sensing applications[54,55], and even in printed electronics[12]. There are still many hurdles for achieving more successful applications of Ni and Ni-Cr nanoparticles, such as the sintering of the nanoparticles, which decreases the surface to volume ratio of the system and modifies its morphology[11,56,57]. For some applications, sintering can be a desirable effect, such as in the mentioned field of printed electronics[58]. It is then clear that a deep understanding of the dynamics of Ni and Ni-Cr nanoparticles is desirable.

But despite the relevance of Ni and Ni-Cr alloys, there are not available interatomic potentials appropriate for accurate modelling the thermo-structural properties of these materials at temperatures above room temperature. In this work we develop interatomic potentials with which to obtain an atomistic view of the behaviour of Ni and Ni-Cr bulk and nanoparticles. We have parametrized the potentials to obtain the best fit of a set of experimental observables, and we have subsequently carefully validated their performance. Using this potential, we are able to predict some properties of bulk Ni-Cr, for which there are no experimental data available. Finally, we used the potential to model Ni-Cr nanoparticles, of various sizes and Ni/Cr ratios, for a range of temperatures at which Ni-Cr alloys are commonly employed, namely between 300 K and 1000 K. MD simulations have become an invaluable source of information of the structural behaviour and deformation mechanisms of nanocrystalline metals[59]. The newly developed potential can be used in simulations of large systems, in order to get a better understanding of these materials, for instance by modelling whole nanoparticles, nanorods and nanotubes, among other nanostructures, as well as thing films and grain boundary characterization or interface behaviour in polycrystals. Furthermore, this new potential can be the starting point for developing interatomic potentials with which to model inconels and other Ni-based alloys, by fitting the parameters for other metals, such as Fe, Co, or Mn.

2.2. Simulation details

Embedded Atom Methods (EAM) provide a well-balanced description of metallic systems, due to their many-body nature capable of dealing reasonably well with metallic bonds[60,61]. The energy of the system is described by:

$$E_{Total} = \frac{1}{2}\sum_{i,j}\phi_{ij}(r_{ij}) + \sum_{i,j}F_i(\rho_i) \qquad (2.1)$$

$$\rho_i = \sum_{j\neq i}\Psi_{ij}(r_{ij}) \qquad (2.2)$$

where $\phi_{ij}(r_{ij})$ are two-body terms and $F_i(\rho_i)$ are many-body terms that depend on the electron density of the metallic system. This electron density is calculated as the sum of the contribution of atoms within a given cutoff, which in many cases only consider first neighbours. There are several choices for selecting the functional dependence for the EAM implementation. Here we use that of Johnson[62], since in our preliminary calculation of the Coefficient of Thermal

Expansion (CTE) of Ni with several published interatomic potential was the one with better performance. Details in this regard are presented below in the Results section.

In the Johnson-type EAM potentials the terms are described as follows:

$$\phi_{ij}(r_{ij}) = Ae^{r_{ij}/d} - \frac{C}{r^6} \quad (2.3)$$

$$F_i(\rho_i) = -\sum_{i,j} E_c \left[1 - ln\left(\rho_i/\rho_{0_i}\right)^{\alpha_J/\beta}\right](\rho_i/\rho_{0_i})^{\alpha_J/\beta} + F_1(\rho_i/\rho_{0_i})^{\gamma/\beta} \quad (2.4)$$

$$\rho_i = \sum_{i,j} A_d e^{B_d(r_{ij}-r_0)} \quad (2.5)$$

where E_c is the cohesive energy, $\alpha_J = 3(\Omega B/E_c)$, (with Ω as the volume per atom, and B as the bulk modulus) and r_0 is the first nearest neighbour distance, $a/\sqrt{2}$ for an fcc metal where a is the lattice parameter. The rest of them are fitted parameters. Note that it consists of two parameters in the two-body term (ϕ), six in the functional form (F), and the last three in the electron density function (ρ). So, within this approach eleven parameters are therefore needed to model an elemental metal solid, three of which can be calculated directly from observables, namely E_c, α_j, and r_0.

For Ni, the cell parameter calculated with the original Johnson potential does not compare well with experiments (Table 2.1), and therefore this requires further improvements for a better description of the Ni alloys, mainly if predictive calculations are intended to be used to improve our understanding of structural and dynamical properties. For the parameterization there are six experimental observables, and therefore it is not possible to do the fitting in a straight way. Another important point preventing the fitting of the potentials in one step is that there are several parameters that are largely correlated and therefore least square minimization with respect to observables is likely to fail if the starting parameters are not close to the optimal ones. In order to overcome these limitations, we developed an iterative procedure that relies on the optimization of a likelihood fitness function defined by us, as will be shown below.

It is known that Cr does not adopt an fcc structure, but a bcc one, and thus there are not experimental observables to be used for fitting fcc Cr. Then, we turned to the calculation of ab-initio observables that we can obtain through electronic structure calculations. However, ab-initio calculation of the elastic constants of Cr in fcc structure fails to provide reliable data, as the energy well of the relaxed fcc structure is so small that any tiny structural deviation pushes the system out from the energy well, resulting in negative elastic constants. We then used the extrapolated experimental data to pure Cr in fcc structure reported elsewhere[63]. Ni-Cr alloys exhibit fcc structures, as they are dominated by the larger content of Ni over Cr. For the parameterization of the interatomic potentials for the alloys only two parameters are needed to be fitted in the Johnson EAM scheme, those of the Buckingham term considering C equal to zero. The available experimental data were used for their determination.

To study the structural behaviour at finite temperatures MD simulations have been carried out using the LAMMPS code[64]. The time step is 1 fs, while the values of the thermostat and barostat parameters are 0.1 and 2.0 ps respectively. Simulations were performed for bulk (in the NPT ensemble) and nanoparticles (in the NVT ensemble) systems, for pure Ni and Ni-Cr alloys. The Cr contents studied were 10, 20, 30, and 40 %. The bulk systems were made of 15x15x15 unit cells, with 13500 atoms, whereas the nanoparticles radii were 3 nm, 5 nm, 7 nm, and 10 nm, with 1289, 5979, 16415, and 47741 atoms, respectively.

As a validation of the parameterized potentials we computed via ab-initio methods the cell variations with applied external hydrostatic pressure (from -20 to

100 GPa) and also the cohesive energy corresponding to each structure. For this purpose we used the VASP code[65]. We have employed the PBE exchange-correlation functional because it has been demonstrated that it is the functional that models transition metals more accurately[66]. The Brillouin zone has been sampled using a 14x14x14 Monkhorst-Pack K-point mesh for the calculations of the systems with only one unit cell. This is the grid that shows the best compromise between accuracy and computational cost. The mesh employed in systems with 2x2x2 unit cells was a 2x2x2 K-point mesh. The cut-off energy was 500 eV. It is important to note that magnetism has been taken into account for both pure metals differently, treating Ni as ferromagnetic and Cr as antiferromagnetic.

It is useful to mention that we tried to fit the potential parameters to ab-initio surface energy curves, but it resulted unsuccessful, even if only small deviations were scanned around the energy minimum. This is a limitation of the classical potential energy functional that is unable to capture with the necessary details the complex energetic behaviour of the metals, mainly Ni, under deformation. Nevertheless, as it will be shown below, the fit of the observables provides a set of potentials parameters that reproduce well the targeted values.

2.3. Results and discussion

2.3.1. Development of the interatomic potentials to model bulk Ni-Cr alloys.

The key point of our procedure for fitting the Ni potentials is based on the use of the code Gulp[67,68] for fitting a reduced number of parameters in wisely designed cycles, until all parameters are modified and then repeated until convergence. This code has implemented the procedures to perform potential fittings, using least squares algorithms. It is important to notice that the complex nature of the metallic bonds hinders the development of classical potentials that perform well at reproducing at the same time structural observables, CTEs, and elastic constants. In this regard, we assigned weights to each calculated observable as compared with experiments in order to construct the fitness function in a way that allows measuring the progress of the overall quality of the fitting process. The procedure we followed to carry out the fitting of the potential parameters is shown in Scheme 2.1a. The procedure is outlined below:

1. A flag indicates if the fitness is being improved or not. Flag is set off at the beginning.
2. The first step is to check the fitness in the system with the starting parameters.
3. In each cycle, a number of optimization steps are conducted, where in each case only three parameters are optimized by a least squares optimization. Three parameters are taken, one from each term conforming the potentials (eq. 2.3 to 2.5), and the number of sets chosen is enough to make sure that all possible combinations of three parameters are considered.
4. If the new fitness is better than the best one obtained before, the new parameters will substitute the best ones; and if not, they are kept unchanged. If the potential is improved in one of the steps of a cycle, flag will be set on.
5. If the cycle has not ended, it will go back to the three parameters fit with a new three parameter combination.
6. If the cycle has ended, it will come back to start a new cycle just if the flag is on; if the flag is off, it means that in the last cycle the potential has not improved, so the algorithm will end.

We have made the fitness calculation according to a threshold tolerance (TT) and a weight for each observable as we show in

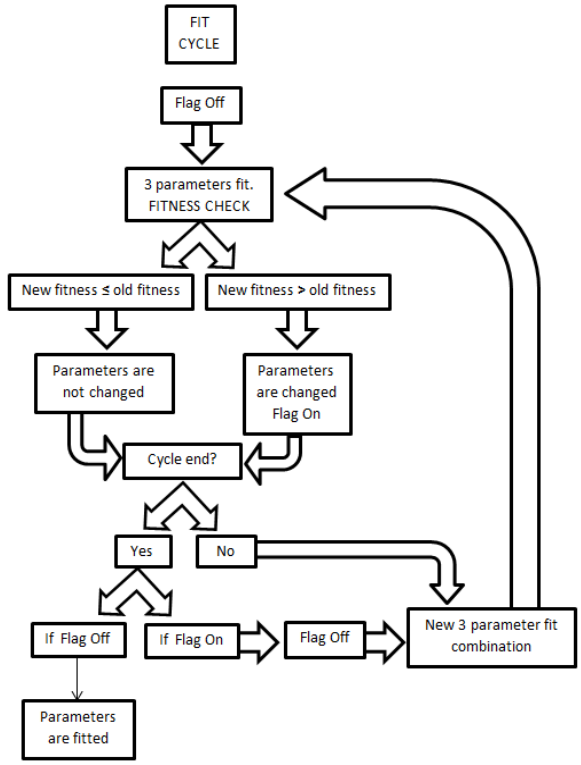

FITNESS CHECK

TT (E_c)=12	weight (E_c)=1
TT (a)=8	weight (a)=1
TT (B)=12	weight (B)=0.75
TT (C_{11})=32	weight (C_{11})=0.5
TT (C_{12})=32	weight (C_{12})=0.5
TT (C_{44})=32	weight (C_{44})=0.5

$$relative.value_i = \frac{|fit.value_i - experimental.value_i|}{experimental.value_i} \cdot 100 \cdot \frac{1}{TT_i}$$

$$partial.fitness_i = f(relative.value_i)$$

$$fitness = \sum_{i=1}^{6} weight_i \cdot partial.fitness_i$$

Scheme 2.1. (Top) Algorithm developed to carry out the fitting of the potential parameters. (Bottom) Algorithm developed to carry out to calculate the fitness function.

Scheme 2.1b. They indicate us the error range that we are able to accept and the importance of each one in the final sum of fitness respectively. The relative value calculated for each observable depends on the comparison between the experimental value and the fitted one.

Once the potentials parameters for Ni have been optimized, we find a much better agreement between calculated and experimental static properties than that obtained with the original Johnson potentials, and a level of agreement similar to that of other published potentials (see Table 2.1). We then studied the dynamic properties of the system. In Figure 2.1 the cell parameters of Ni as a function of the temperature are plotted. The newly developed interatomic potential is able to predict the variation with temperature of the cell parameters within an error of the order of 0.01 Å, while the errors obtained with the potentials developed by Bonny et al. increase as temperature increases, reaching 0.04 Å at 800 K. We have not included in Figure 2.1 the behaviour of the cell parameters as calculated with the MEAM interatomic potential, because this set of potentials, although providing excellent static properties, results in large structural instability of the simulation cell in NPT MD simulation, *i.e.* thermal motion causes the structure to deform, losing the cubic symmetry and giving rise to unphysical structures.

Table 2.1. Experimental[69] and simulated[62,63,70,71] static observables (cohesive energy, lattice parameter, elastic constants, and bulk modulus) and CTEs of bulk fcc Ni.

fcc Ni	*Exp.*[69]	*Johnson*[62]	*Bonny*[63]	*Sutton Chen*[70]	*MEAM*[71]	*This work*
$E_c\left(\frac{eV}{atom}\right)$	-4.45	-4.75	-4.45	-4.43	-4.45	-4.45
a (Å)	3.519	3.433	3.519	3.521	3.521	3.519
$B\ (GPa)$	179	167	179	195	181	179
$C_{11}\ (GPa)$	247	230	247	231	247	235
$C_{12}\ (GPa)$	147	134	147	177	148	151
$C_{44}\ (GPa)$	125	157	125	80	125	131
$\alpha_{300K}\ (10^{-6}K^{-1})$	15.4	16.3	3.4	21.3	5.3	16.1

The new potential also provides an improved description of the variation with temperature of the CTEs, which vary from 15.3x10^{-6} K^{-1} to 18.8x10^{-6} K^{-1} in the temperature interval from 100 K to 1000 K, while the experimental CTEs change from 14.1x10^{-6} K^{-1} to 17.6x10^{-6} K^{-1}. This is in contrast to the previous well accepted potential for Ni-Cr systems[63], which predicts CTEs that are too low in the range of temperatures studied, and that rises too quickly as temperature increases.

Since Ni is the most abundant metal in most Ni-Cr alloys of industrial relevance, the improvements that the new interatomic potentials yield at modelling bulk Ni will be of help when modelling structural and mechanical properties of Ni-Cr alloys. In Table 2.2 we show the static observables for bulk Cr. It must be noted that bulk Cr is not stable with an fcc structure, so there are no direct experimental data available of fcc Cr. Nevertheless, Smith and Was[72] extrapolated the data for pure fcc Cr, using

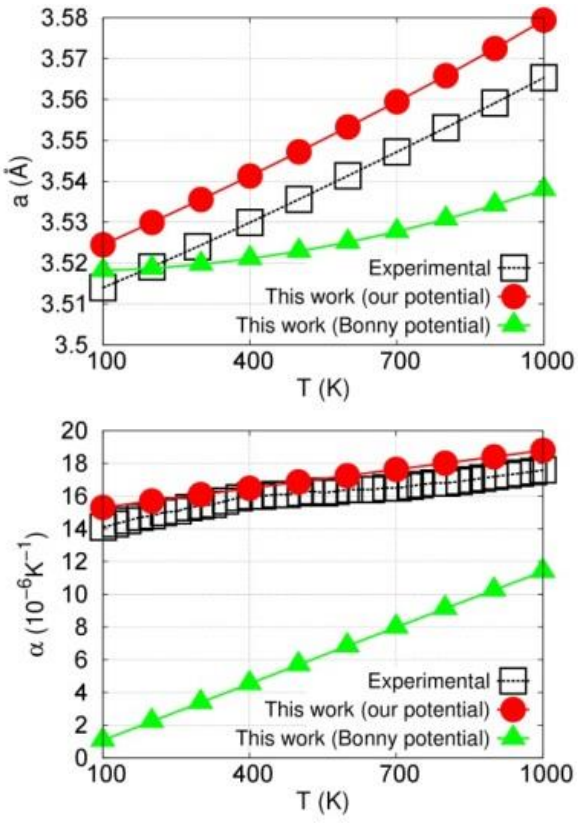

Figure 2.1. Experimental and calculated lattice parameters and CTE for fcc Ni, as a function of temperature.

Table 2.2. Extrapolated experimental[72] and simulated static observables (cohesive energy, lattice parameter, elastic constants, and bulk modulus) of bulk fcc Cr.

Cr fcc	*Exp.*[72]	*Bonny*[63]	*This work*
$E_c\left(\frac{eV}{atom}\right)$	-3.69	-3.69	-3.72
a (Å)	3.619	3.619	3.619
$B\ (GPa)$	202	202	202
$C_{11}\ (GPa)$	249	249	257
$C_{12}\ (GPa)$	178	178	174
$C_{44}\ (GPa)$	143	143	139

Table 2.3. Experimental[73–75] and simulated static observables (lattice parameter, elastic constants, and bulk modulus) of fcc Ni-Cr with a Ni/Cr ratio of 80/20.

fcc Ni-Cr	*Exp.* [73–75]	*This work Bonny Potentials*[63]	*This work Our Potentials*
a (Å)	3.555	3.554	3.552
$B\ (GPa)$	185	154	196
$C_{11}\ (GPa)$	247	197	251
$C_{12}\ (GPa)$	154	132	168
$C_{44}\ (GPa)$	128	107	132

Table 2.4. Johnson-type EAM fitted parameters for fcc Ni, Cr, and Ni-Cr alloys.

Buckingham			
Parameter	*Ni-Ni*	*Ni-Cr*	*Cr-Cr*
A	6393.86	6675.50	5804.36
ρ	0.27829	0.27759	0.27800
Johnson EAM functional			
Parameter	*Ni*	*Cr*	
E_c	4.45000	3.69000	
F_1	4.49058	4.93708	
ρ_0	4.83626	4.08507	
α_J	5.09453	6.03694	
β	6.45654	6.32622	
γ	8.85297	8.89153	
EAM density			
Parameter	*Ni*	*Cr*	
A	0.42133	0.61852	
B	2.67635	2.13582	
r_0	2.48900	2.13582	

values from various Ni-Cr alloys, of increasing percentage of Cr. These are the data presented in Table 2.2. It is observed that the agreement between the data obtained with the new potentials and the extrapolated experimental values is very good.

Once the potentials for modelling fcc Ni and Cr separately were available, we proceeded to fit the potential to model Ni-Cr alloys with a Ni/Cr ratio of 75/25. The results obtained for the calculated static properties of a Ni-Cr alloy with a Ni/Cr ratio of 80/20 are shown in Table 2.3, where we observe that the new Ni-Cr potentials reproduce well the experimental observables. Note that the quality of the fit with respect to the static observables for pure Cr is comparable to that of previous interatomic potentials[63], while the results for Ni-Cr are largely improved with our potential.

The fitted potentials parameters obtained in this work are reported in Table 2.4. Their use also provides better results than previous potentials when modelling the thermal behaviour of Ni-Cr solids, as can be seen in Figure 2.2. In particular, the curve of the variation of the cell parameter with temperature is close to the experimental results (the difference is of the order of 0.01 Å) and changes in a similar manner; while the curve obtained with previous potentials diverges from the experimental values as temperature increases. The behaviour of the CTE is similar to that observed for Ni; the new potential predicts values that are closer to experiment and vary with temperature in a similar fashion.

As a further rigorous structural test for the fitted interatomic potentials, we have made a comparison of the lattice parameters and the cohesive energies as a function of pressure, calculated with the potentials and with DFT calculations, for the three model systems (*i.e.* Ni, Cr, and Ni-Cr). Figure 2.3 shows that a successful reproduction of the DFT data is achieved with the new potentials. Note that the

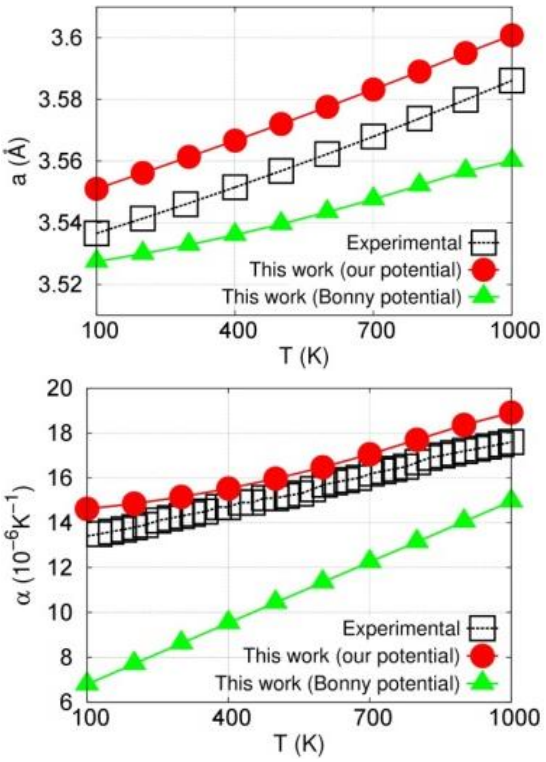

Figure 2.2. Experimental[76] and calculated lattice parameters (top) and CTEs (bottom) as a function of temperature for fcc Ni-Cr alloy with a Ni-Cr ratio of 80/20.

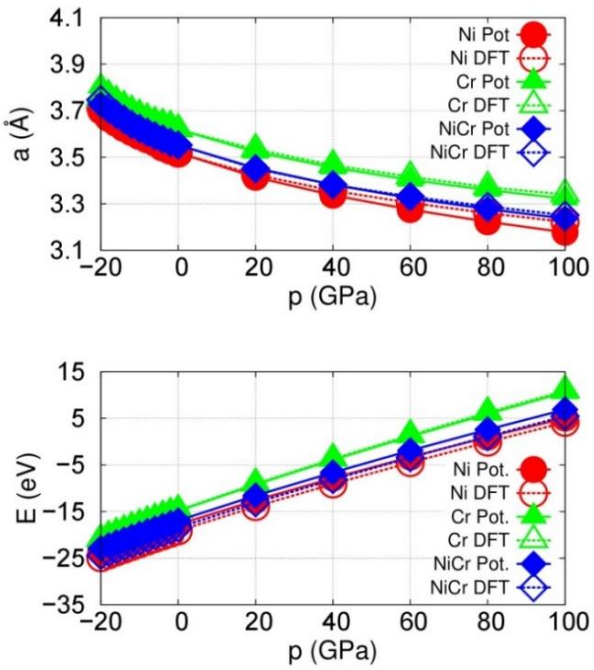

Figure 2.3. Dependence of the lattice parameters (top) and the cohesive energies (bottom) with the applied external pressure, calculated with the new potentials and with DFT calculations, for fcc Ni, Cr, and Ni-Cr 80/20.

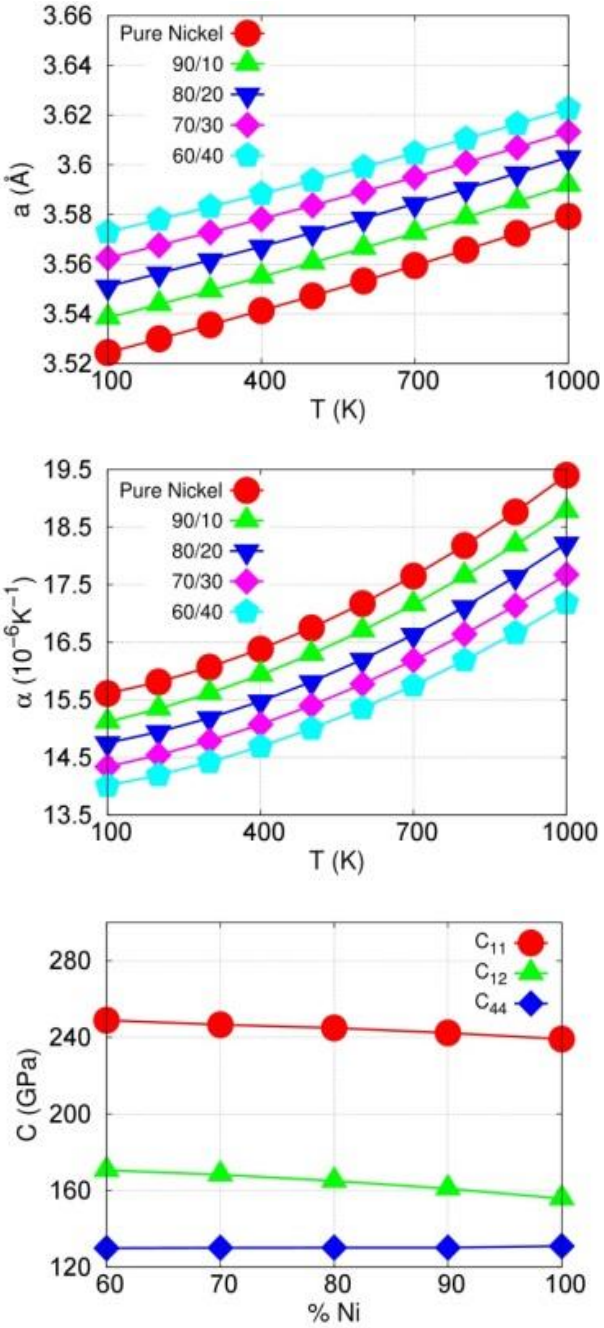

Figure 2.4. Calculated lattice parameters (top) and CTEs (middle), as a function of temperature, as well as the three elastic constants (bottom), for Ni-Cr alloys of various compositions.

displacement of the enthalpy minimum as a consequence of the applied pressure is dictated by the curvature of the surface energy, thus by doing so we are proving that this curvature is reproduced by the new potentials. This is valid even for distances well beyond that of the surface energy minimum, *i.e.* apart from the harmonic region that is used for the calculation of the elastic constants. The agreement of the computed cohesive energies using the potentials with respect to those calculated by DFT is also remarkable.

Indeed, the fact that the structural behaviour is well described by the new potentials at interatomic distances belonging to the region of the anharmonic curvature of the surface energy is a solid base for validating the predictive character of our fitted potentials towards their use at higher temperatures and pressures.

2.3.2. Thermo-structural characterization of bulk Ni-Cr solids

With the interatomic potential developed for Ni-Cr alloys we can predict the properties of Ni-Cr for which there are no experimental data. For example, Figure 2.4 shows the variation with temperature of the lattice parameters and CTEs, as well as

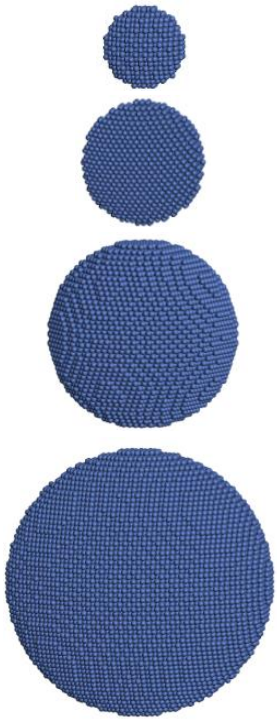

Figure 2.5. Ni nanoparticles with diameters of 3 nm, 5 nm, 7 nm, and 10 nm, from left to right. Ni-Cr nanoparticles of various Ni-Cr ratios have the same atomic positions, but have the corresponding percentage of Ni atoms exchanged with Cr atoms.

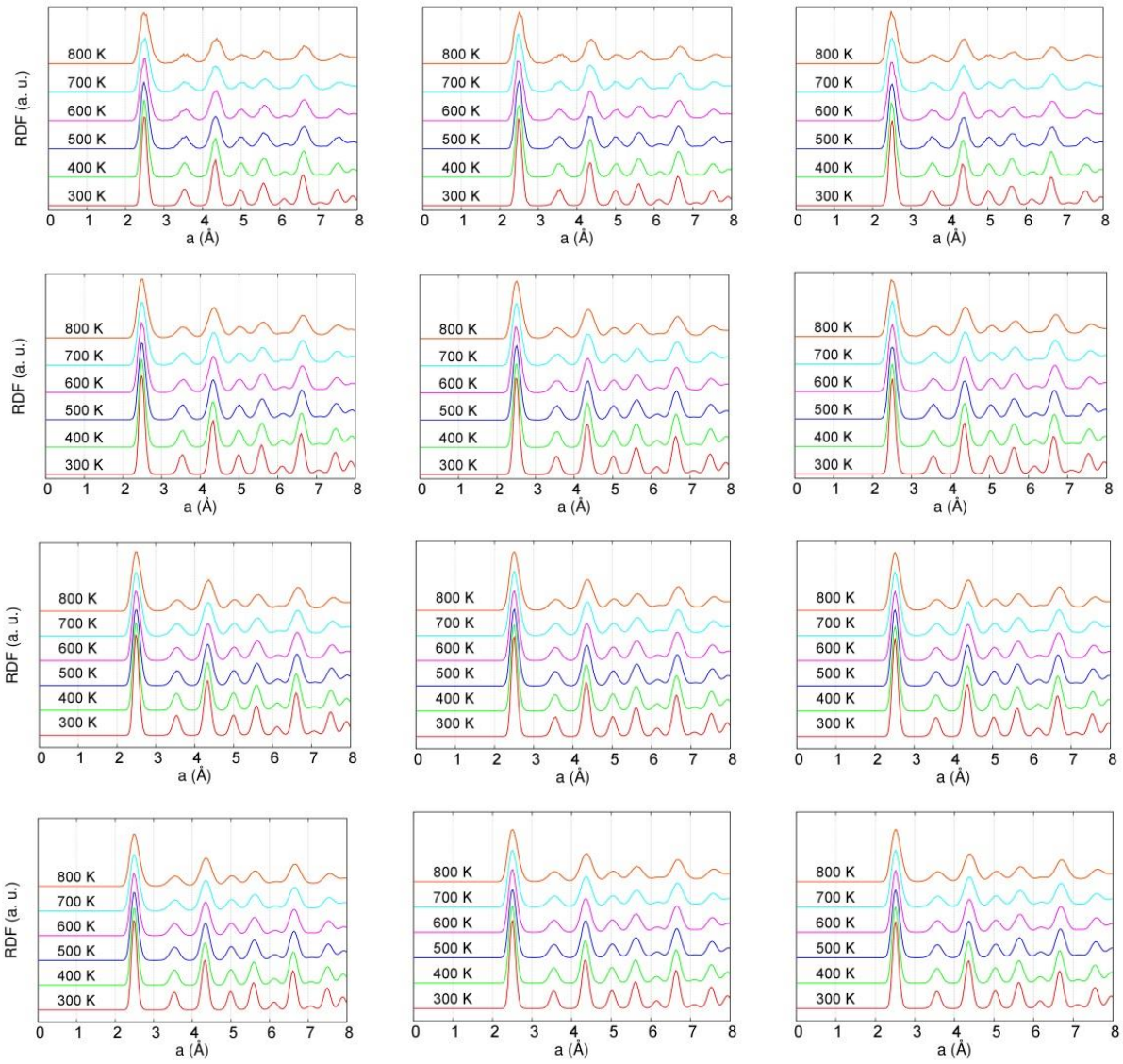

Figure 2.6. Ni-Ni RDFs of Ni-Cr nanoparticles of sizes (from top to bottom) 3 nm, 5 nm, 7 nm, and 10 nm. Left, middle, and right panels correspond to Ni-Cr ratios of 100/0, 90/10, and 80/20, respectively.

the three elastic constants, for Ni-Cr alloys with Ni-Cr ratios of 100/0, 90/10, 80/20, 70/30, and 60/40.

An interesting result is that the inclusion of Cr can decrease down to 10 % the CTEs, which would be a point to take into accountwhen structural materials are designed for their use at high temperatures. It is also observed that the increase of the amount of Cr lowers the CTEs, which is in concordance with the smaller slope, in absolute values, of the cell parameter vs. pressure curves (Figure 2.3). The lattice parameters, as expected from the molar volume of each metal, increase as the amount of Cr increases. We found that by controlling the alloy composition the cell parameter can be tuned within an interval of 0.05 Å. It is also observed that the estimated C11 and C12 elastic constants decrease with the content of Ni, mainly C12, whereas C44 remains almost unaffected by the binary mixture composition.

2.3.3. Thermo-structural characterization of Ni-Cr nanoparticles.

Once we have tested the capability of the new interatomic potentials to model accurately bulk Ni-Cr, we use them to predict the thermo-structural properties of Ni-Cr nanoparticles of different sizes. We have studied 4 nanoparticles, whose diameters are 3 nm, 5 nm, 7 nm, and 10 nm (see Figure 2.5).

Their structures were generated by cutting spherical pieces of fcc Ni bulk crystal. It must be noted that these sizes are large enough so that most of the atoms are in the bulk, which means that the potential developed can be used without corrections.

We have carried out MD simulations at temperatures between 300 K and 800 K, in order to study the influence of temperature on the structure of the nanoparticles. For each nanoparticle, we performed an initial energy minimization, after which we equilibrated the system during 30 ps at 800 K. Subsequently we carried out a production run, at that temperature, of 50 ps. The final structure was employed as a starting point of a new MD simulation, at 700 K, for which another equilibration run of 30 ps was performed, followed by a production run of 50 ps. This procedure continued until a final temperature of 300 K. The final structure at 300 K, for all nanoparticles, was crystalline, with very little disorder. This fact is reflected by the peaks of the Ni-Ni Radial Distribution Functions (RDFs) of the nanoparticles, which are shown in Figure 2.6, for all nanoparticle sizes, temperatures, and Ni-Cr ratios.

Our simulations show therefore that the crystalline structure of the nanoparticles is very resilient to changes in temperature, since even in this fast quenching of the systems highly ordered crystalline structures are readily attained. We mentioned previously the fact that all nanoparticles can be regarded as bulk-like nanoparticles, at least at room temperature, due to their large sizes. In order to check whether this is the case, we have studied the surface layer of the Ni nanoparticles, comparing the RDF of a 1nm thick outer shell with the RDF of the nanoparticle core (the rest of the nanoparticle), as well as with the RDF of the fcc Ni bulk structure, at 300 K. Since performing a MD simulation of the outer

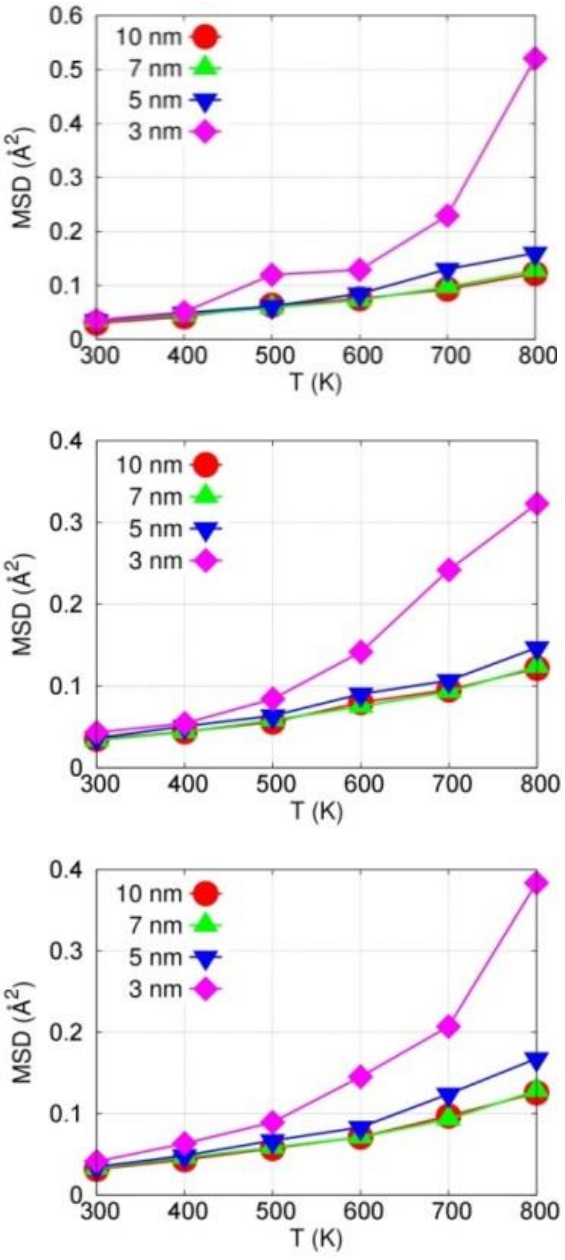

Figure 2.7. MSDs of the atoms of each nanoparticle, as a function of temperature, for Ni-Cr nanoparticles with Ni-Cr ratios, from top to bottom, of 100/0, 90/10, and 80/20.

layer of the nanoparticle, without the core, would lead to unrealistic results, we have calculated the RDF of just the last structure of the simulations. The results show that all nanoparticles, even the smallest one show similar RDFs, which in turn are very similar to that of the bulk. Our simulations suggest that there are no large rearrangements of the surface layer of the nanoparticles.

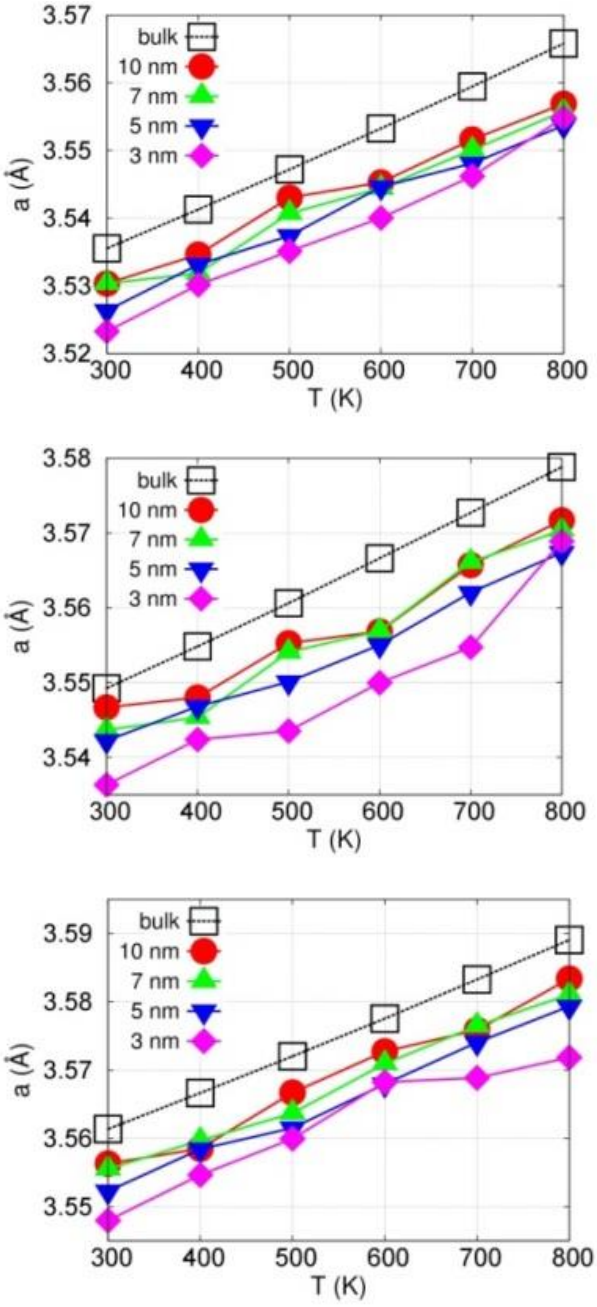

Figure 2.8. Variation with temperature of the cell size, for Ni-Cr nanoparticles with Ni-Cr ratios, from top to bottom, of 100/0, 90/10, and 80/20. The values obtained for the bulk are also shown, for comparison.

Another interesting result from our simulations is that even at 800 K the nanoparticles get disordered, but still keep a high level of crystallinity. There is a big difference in this respect between the smaller nanoparticle (3 nm) and the rest. One way to analyse this different behaviour is calculating the Mean Squared Displacement (MSD) of the atoms of the nanoparticles. Figure 2.7 shows the MSDs of all nanoparticles, as a function of temperature.

We observe that the 3 nm nanoparticles show the largest displacements of the atoms, and that there is very little difference between the rest of the nanoparticles, *i.e.* when the size reaches 5 nm the nanoparticles start having a bulk-like behaviour and an increase in size does not change drastically the dynamics of the atoms.

In order to study how the properties of the nanoparticles converge towards those of the bulk, we analysed the size of the unit cell. In order to calculate the size of the cells of the nanoparticles we made use of the RDFs. In the fcc structure the second peak of the RDF corresponds to the size of the unit cell, so we obtained the Gaussian that best fitted the second peak and calculated the unit cell size as the distance at which the Gaussian is centred. Using this method we were able to predict the variation of cell size for the nanoparticles, as a function of temperature (see Figure 2.8). We see that the cell sizes of the nanoparticles are slightly smaller than those of the bulk structure, for all temperatures, and that the variation with temperature has similar slope in all cases. The noise of the data could be due to the uncertainty in definition of a unique cell size for non-periodic structures such as the nanoparticles, as well as to the disorder associated with the presence of the surfaces.

As a final measure of the convergence of the properties of the nanoparticles we analysedpotential energy

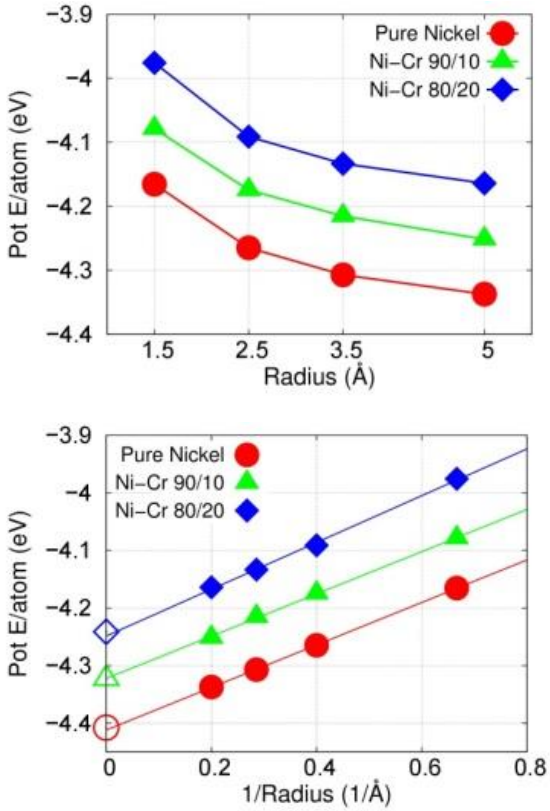

Figure 2.9. Left, potential energy per atom of the nanoparticles at 300 K, as a function of size. Right, potential energy per atom of the nanoparticles at 300 K, as a function of the inverse of the size. The energies per atom of the bulk structures are also shown on the right panel, over the y axis (open symbols)

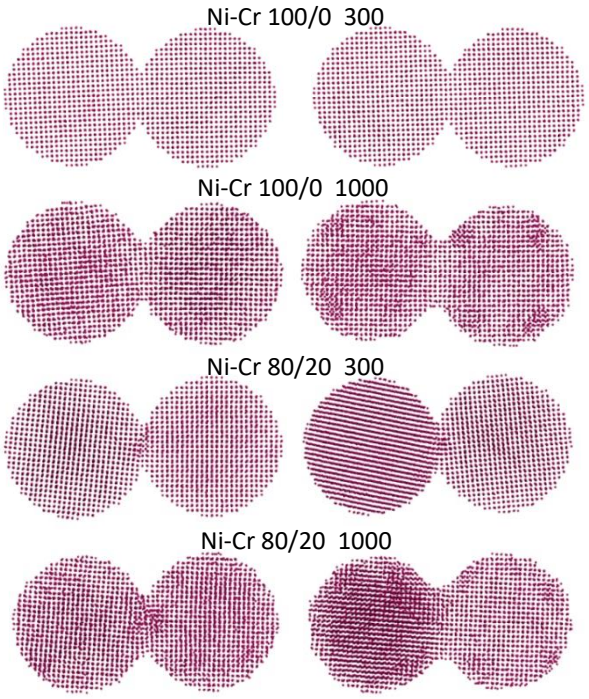

Figure 2.10. Snapshots of the simulations of the sintering process between two 5 nm nanoparticles structures, taken at 10 ps (left) and 500 ps (right). The Ni/Cr ratios and temperatures of the simulations are, from top to bottom 100/0 300 K, 100/0 1000 K, 80/20 300 K, and 80/20 1000 K.

as a function of size. The potential energy per atom of the nanoparticles at 300 K, as a function of size, is shown in Figure 2.9, left. We observe the expected decrease of energy as the size increases, for all Ni-Cr compositions. On the right we plot the same energies, but as a function of the inverse of the size. With this type of plot we see that, for each composition, all the energies are placed in a line, and that the line reaches the y axis at a value which is very close to that calculated for the bulk structure with the corresponding composition.

For example, the line extrapolated for the pure nickel nanoparticles reaches the y axis when the energy is -4.40 eV/atom, exactly the same value obtained for the pure nickel bulk structure. We must note that the experimental cohesive energy of fcc Ni is -4.45 eV/atom, which differs from this value due to the increase of potential energy of the system associated with the thermal motion at 300 K.

As mentioned above, changes in state of aggregation of the nanoparticles can induce changes in the properties of the materials[77]. We have employed the new Ni-Cr potential to model the sintering of nanoparticles. Since we have not observed so far large differences between the behaviour of the nanoparticles of different sizes, we did not study the sintering of nanoparticles of all sizes. We decided instead to study the sintering of two 5 nm nanoparticles, with Ni-Cr ratios of 100/0 and 80/20, at two different temperatures (300 K and 1000 K). To do that, we placed initially the two nanoparticles in contact, at a distance of 2.49 Å, which is the distance between first neighbours in the bulk structure of fcc Ni. The systems were

energy minimized, after which an equilibration of 30 ps was carried out, followed by a production run of 500 ps. Figure 2.10 shows snapshots at the beginning of the simulations (at 10 ps) and at the end (at 500 ps).

We observe that for both types of nanoparticles (pure nickel and Ni-Cr alloy with Ni-Cr ratio of 80/20) there is no loss of crystallinity at 300 K, and the contact zones do not suffer significant changes. The main change is observed for the Ni-Cr 80/20 nanoparticles, which undergo a slight rotation in order to release some stress (see Figure 2.10c). The simulations at 1000 K show that, as expected, there is more disorder in the structures associated to the higher level of thermal motion. This thermal motion is not enough to induce the fusion of the two nanoparticles and form a single larger nanoparticle. The contact zone is larger than in the simulations at 300 K, but it is still possible to regard the systems as formed by two nanoparticles in contact, so that the surface/volume ratio is similar to that a 300 K. Therefore, our simulations suggest that Ni-Cr nanoparticles also show the thermal stability that is characteristic of bulk Ni-Cr materials.

2.4. Conclusions

We have fitted a new set of interatomic potential parameters that model the thermo-structural properties, including the mechanical properties, of Ni-Cr alloys. To do that, we have developed a fitting algorithm that uses a set of experimental observables. The fitted potential models correctly described the dependence with temperature of the lattice parameters and the coefficients of thermal expansion, for fcc Ni and Ni-Cr solids. The new potential has also been used to predict the properties of Ni-Cr materials of various compositions. Finally, we have used the new potential to study the behaviour of nanoparticles of various sizes (3 nm, 5 nm, 7 nm, and 10 nm), finding that the lattice parameter increases as the size increases. The smallest nanoparticles (3 nm) behave differently from the others, *i.e.* when the size reaches 5 nm the nanoparticles show significant bulk-like features, although 3 nm nanoparticles are large enough to have a bulk-like core structure and show small surface distortions. Finally, the MD simulations of the sintering process show that when two 5 nm nanoparticles are in contact, they keep their structures as two separated nanoparticles, with a contact region in the middle, suggesting that materials made of nanoparticles of Ni-Cr alloys as small as 5 nm are quite resilient to thermally-induced damage and therefore capable of being used in applications such as catalysis, where high temperatures and aggressive environments are common.

3. Fitting electron density as a physically sound basis for the development of interatomic potentials of complex alloys

The development of new interatomic potentials to model metallic systems is a difficult task, due in part to the dependence between the parameters that describe the electron density and the short-range interactions. The problem of finding adequate parameters becomes very complicated, and the iterative methods commonly employed to do that can get stuck in local minima and provide unphysical parameters. To solve this problem, we have developed a methodology for obtaining the electron density parameters independently of the short-range interactions, so that physically sound parameters can be obtained to describe the electron density, after which the short-range parameters can be fitted, thus reducing the complexity of the process and yielding better interatomic potentials. With the new method we can develop self-consistent, accurate force fields, using solely calculations, with no need to fit to experimental data. Density Functional Theory calculations are used to compute the observables with which to fit the potential. We applied the method to a Ni-based Inconel 625 superalloy (IN625), modelled here as Ni, Cr, Mo and Fe solid solution alloys. The capability of the force fields developed using this new method is validated, by comparing the structural and thermo-elastic properties predicted with the force field, with the corresponding experimental data, both for single crystals and polycrystalline alloys.

3.1. Introduction

Computer modeling has become an organic part of materials research, saving time through in silico design or providing deep understanding on materials behavior[78,79]. First principles-based atomistic simulations allow us to model a wide range of properties[80–84], being Density Functional Theory (DFT) the usual method of choice, since it provides accurate results at an affordable computer cost[85,86]. Despite the increase in computing power and efficiency of scientific software[87]. DFT calculations are limited to systems comprised of a few thousand atoms. Atomistic simulations of larger systems, or similar systems simulated using large scale Molecular Dynamics (MD) simulations, require the use of classical mechanics-based calculations, which rely on the use of accurate interatomic potentials (IP)[78,87,88].

Besides the traditional fields in which alloys have played a relevant role, such as structural materials in building and transportation, there is an increase in use of superalloys (in particular Ni-based alloys) in various fields, such as gas turbines[89], solar thermal power plants[90], steam

turbines[91] heat exchangers for nuclear reactor systems[92], catalysis[93,94], batteries[95], fuel cells[96,97] and medicine[98,99]. These applications fuel the need to improve the quality of interatomic potentials for alloys, and the methods with which they are parameterised. Many-body potentials are known to be the best option for modelling metallic systems, with the handicap of having a large number of parameters. DFT calculations are now commonly used to provide the observable data that can be used to carry out the fitting of the parameters[87,100–103]. There are even computer codes designed to perform this task automatically[67,104–108]. They use a set of experimental and/or calculated data as a benchmark, *i.e.*, these values are compared with the values predicted by the IPs, and the IP parameters are changed iteratively until a minimum is obtained. These methods are very dependent on the initial values used for the parameter optimisation, so that convergence is very slow, or gives rise to unphysical values, if the initial parameters are not close enough to the "correct" ones. For example, even for a simple system, which does not require many-body potentials, the ab initio-derived parameters for CO2 in silica zeolites[109] need to be modified for being used in aluminosilicate zeolites[110].

In the case of metals, and more acute in multi-element alloys, the situation is particularly difficult, due to the sloppy behaviour of the interatomic potentials and their related soft modes in parameter space, which can cause the minimization algorithms to fail to converge[107]. These materials are usually modelled using many-body potentials, such as Embedded Atoms Method (EAM) potentials, in which the energy is calculated using the following equations:

$$E_{Total} = \frac{1}{2}\Sigma_{i,j}\Phi_{ij} + \Sigma_{i,j}F_i(\rho_i) \quad (3.1)$$

$$\rho_i = \Sigma_{i\neq j}\psi_{ij}(r_{ij}) \quad (3.2)$$

where:

$$\Phi_{ij}(r_{ij}) = Ae^{r_{ij}/d} - \frac{C}{r^6} \quad (3.3)$$

$$F_i(\rho_i) = -\Sigma_{i,j}E_c[1 - \ln(\rho_i/\rho_{0_i})^{\alpha_J/\beta}](\rho_i/\rho_{0_i})^{\alpha_J/\beta} + F_1(\rho_i/\rho_{0_i})^{\gamma/\beta} \quad (3.4)$$

$$\rho_i = \Sigma_{i,j}A_d e^{B_d(r_{ij}-r_0)} \quad (3.5)$$

When doing numerical experiments to explore the effects of the parameters on the total energy of the system we found that there is a direct numerical dependence between the repulsive factor of the Buckingham-type short-range term (eq. 3.3) and the exponential factor of the electron density term (eq. 3.5). As a consequence of the strong correlation between these two values, there must be a correct balance between these two factors, in order to obtain a sensible value of the total energy. If we change one factor without changing the other, we can introduce spurious changes in the total energy of the system, thus changing all the properties that depend on the total energy. Here, we develop a methodology to solve this problem and to remove the sloppy behavior of the parameterization. A method has been devised to obtain a self-consistent set of values of the electron density terms, which describe adequately the physics of the system. This leads to an enormous reduction of the complexity of the problem, since we can perform the optimization of the other parameters independently.

We applied this method to one of most complex systems (in terms of the nature of the interactions involved) that are described using IPs, namely multi-element alloys. The interest in Ni-based superalloys has a renewed rise, owing to their performance in novel advanced applications, as mentioned above, along with their good performance as resistant structural materials in advanced engineering applications, in particular at high temperature and corrosive conditions[111–113], where they are even capable of maintaining acceptable thermo-mechanical properties at thermal creep conditions. These materials retain the face-

centered cubic (FCC) crystal packing of its main constituent, Ni solid metal, which is present at concentrations of ca. 60 % wt[114]. Interestingly, the remaining 40% is composed by elements such as Cr, Fe, Mo, and W, which do not crystallize in FCC structures in monometallic phases[114]. We have applied the new method for developing force field parameters to model the Ni-Cr-Fe-Mo superalloys, in particular Inconel 625 superalloy (IN625).

The chapter is organised as follows. The next section is devoted to present the methodology and computational details, first by presenting the methodology used for the parameterisation, followed for that used for the validation. The results start with the fit of the electron density and the parameterisation of the potential. The modelled structural and thermo-elastic properties are shown in the last part of the chapter85 as validation of the developed potential.

3.2. Simulation details

3.2.1. Development of interaction potentials for Ni, Cr, Mo and Fe alloy from DFT calculations

In a previous work, we developed an EAM-potential parameterization method that allowed us to obtain an accurate description of the structural and elastic behavior of Ni-Cr alloys and to predict the behavior of nanoparticles[115]. This method is based on an iterative procedure, which allows the optimization of a reduced number of parameters in each cycle, until all parameters are fitted, and successive iterations do not improve further the quality of the fit. We used this method as the strategy to conduct the parameterization of Ni-Cr-Fe-Mo superalloys EAMs. However, the method failed for multi-element alloys, due to the difficulties appearing to separate the large interdependence of the parameters for such number of components in the alloy. To circumvent this limitation, here we devise a method that allows the parameterization of multi-element EAM potentials at a reasonable cost. The main novelty of our development is the fitting of the electron-density parameters of the EAM potential (eq. 3.4) to reproduce the DFT-computed electron density in the solid state. We noted that early developments of EAM potentials used the electron density of the free atoms[61,116]. However, the electron density changes notoriously upon the formation of the solids, so the electron properties of free atoms are not the best to fit parameters to model solids.

First, we relaxed the structures by energy minimization, and then we computed the electron density of the solids. The calculations were performed with the VASP code[65,117], using the PBE exchange-correlation functional[118]. The Brillouin zone has been sampled using a 14x14x14 Monkhorst-Pack K-point mesh. The cut-off energy was 500 eV. We performed spin-polarized calculations to take into account the magnetism of the system. The cubic symmetry of the elemental solids in a FCC structure was employed, the electron density was studied along high symmetry lines pointing to neighboring atoms.

Efforts to fit the rest of the parameters of the interatomic potential to energy surface curves[68], employing wisely-constructed deformed unit cells, were not successful. Instead, we employed ab initio-derived elastic and energetic observables, which together with their respective structures were used in the automatic fitting procedure, conducted with the aid of the Gulp code[67,68]. The cohesive energy, Ec in (Eq. 3.4), and the nearest neighbor distance, r_0 in (Eq. 3.5), for the FCC pure metals, were directly determined from the data obtained for the DFT energy-minimized structures. Cr, Fe and Mo crystallize in a body-centered cubic (BCC) crystal packing, *i.e.* the FCC structure typical of the Ni-based alloys is not the most stable structure. Nevertheless, standard cell

Table 3.1. Atomic composition of IN625 superalloy: experimental (first row, from ref. [119]) and interatomic potentials simulated (second row) systems.

Atomic Composition	Ni	Cr	Mo	Fe	Cb+Ta	C	Mn	Si	P	S	Al	Ti	Co
Experimental[119]	>58	20-23	8-10	<5	3.15-4.15	0.1	0.5	0.5	0.015	0.015	0.4	0.4	1
Simulated	66	21	9	4	–	–	–	–	–	–	–	–	–

deformations used to compute elastic constants of cubic solids[120] allowed the calculation of the bulk modulus and the C11, C12, and C44 elastic constants of Fe in the FCC structure. However, in the case of Mo, any small anisotropic deformation around the equilibrium structure conduced to structural instabilities, until a BCC packing is achieved, thus preventing the calculation of the elastic constants in the FCC structure. Fortunately, the FCC Mo structure remains stable upon applied pressure over a considerable range of hydrostatic pressures, allowing the computation of lattice energy values for a set of stable structures at their corresponding enthalpy equilibrium. All possible combinations of binary alloys must be taken into account for fitting the two-body parameters accordingly.

3.2.2. Validation of the interatomic potential

Once the whole set of interatomic potentials was derived, we validated the goodness of the potential via two types of calculations: Lattice Dynamics and Molecular Dynamics simulations at an atomistic level and calculations at a continuum level. The latter was performed by two approaches, namely an analytical and a Fast-Fourier Transform numerical homogenization model. To model the structural features at low temperatures, where the zero-point energy has a dominant effect on the lattice parameters, we used lattice dynamics (LD)[121], as implemented in Gulp. For this purpose, after minimizing the cell parameters at 0 K, various sets of structures were created by inducing isotropic cell variations around the minimum, and the phonon spectra were computed for each of those structures.

Then, for each temperature and structure, the free energy was calculated, and the minimum in the free energy vs lattice plot provides the most likely value of the lattice parameters. In each case, three independent simulations were performed with the selected composition and random atom distributions. The resulting average values were used to calculate the average cell parameters for each temperature. At higher temperatures, where the asymmetry of the bonds energy profile is relevant, MD

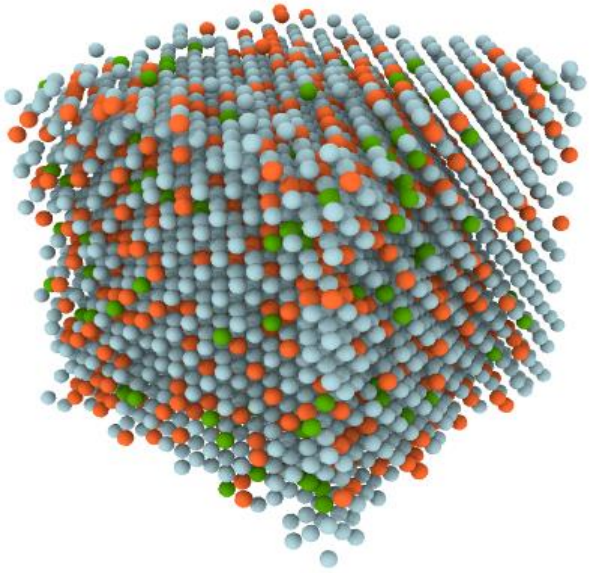

Figure 3.1. Representation of a Ni-based alloy with Cr, Mo and Fe in solid solution.

simulations in the NPT ensemble were conducted using the LAMMPS program[64]. Considering the large cost of the LD calculations[122,123], 8x8x8 computational cells (ca. 28.9 Å cell axis), consisting of 2048 atoms, were used, while 35x35x35 cells (ca. 126 Å cell axis), containing 171500 atoms, were used for the MD simulations. A time step of 1 fs was used, with equilibration and production runs of 30 and 1000 ps, respectively. The temperature variation was 1 K/ps and the relaxation time for the thermostat and barostat were 0.1 and 2 ps, respectively. The simulation cells employed for both LD and MD were created with compositions similar to those experimentally measured for IN625 (Table 3.1). The atoms were initially randomly distributed over the sites of the unperturbed FCC lattice and allowed to move freely during the simulation. A depiction of a selected alloy is shown in Figure 3.1.

Due to the lack of experimental information about the evolution of single crystal elastic constants with temperature, we provide a rigorous validation of the behavior of the new interatomic potentials by comparing with experimental results for polycrystals. For this, we upscale the single crystal results, following an analytical and a numerical method. The single crystal-like elastic constants were determined by MD simulations in the NVT ensemble, at the cell volumes determined above, using a strain tensile test approach[124,125]. The methodology is based on the atomistic simulation of two uniaxial strain tests in different orientations of the crystal. The deformation was applied along the x-axis, constraining the strains along the y- and z-axis. The crystal orientation with respect to the Cartesian coordinates is shown in Figure 3.2. For each temperature, an initial compressive strain of $\epsilon_{xx}^{0} = -0.5\%$ was applied on the boundary of the cell. The strain was then increased by $\Delta_{xx} = 0.1\%$ to reach a final strain of 0.5%.

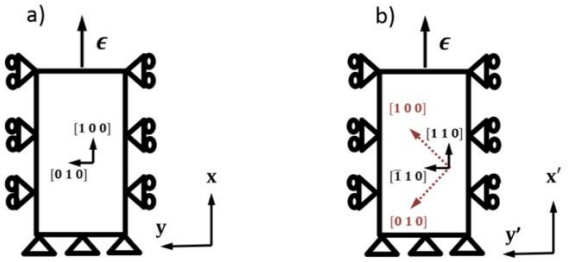

Figure 3.2. Schematic view of the uniaxial strain simulations. a) Configuration of the simulation in which the materials axes [100] and [010] are coincident with x and y, respectively. b) Configuration of the simulation in which the material axes [100] and [$\bar{1}10$] are coincident with x and y. This configuration is rotated 45º with the previous one. Z-axis is parallel to the crystal axis [0 0 1] in both configurations.

The use of the uniaxial strain along the x-direction (ϵ_{xx}) allowed the determination of the (C_{11} and C_{12}) elastic constants of the crystal according to:

$$C_{11} = \frac{\sigma_{xx}}{\epsilon_{xx}} \quad (3.6)$$

$$C_{12} = \frac{\sigma_{yy}+\sigma_{zz}}{2\epsilon_{xx}} \quad (3.7)$$

where σ_{xx}, σ_{yy}, and σ_{zz} are the normal stresses in the x-, y-, and z-direction, respectively (Figure 3.2a). In the second configuration, the crystal was rotated by 45º around the z-axis for the uniaxial strain test, resulting in x|| [110], y|| [$\bar{1}$10], and z|| [001] (Figure 3.2b). The cell was then deformed along the x-axis and the elastic constant C_{44} was obtained:

$$C_{44} = \frac{\sigma_{xx}}{\epsilon_{xx}} - \left(\frac{C_{11}+C_{12}}{2}\right) \quad (3.8)$$

If the material has no texture (*i.e.*, the ODF is random), the polycrystal will be isotropic and analytical expressions for two independent elastic constants (*i.e.*, either the bulk and shear moduli, *B* and *G*) are given by different mean field methods using standard formulae[126–128]. Further details are supplied in the supplementary information. For a numerical approach of the elastic behaviour of the polycrystal, a home-made computational homogenization FFT code, developed in IMDEA-Materials,

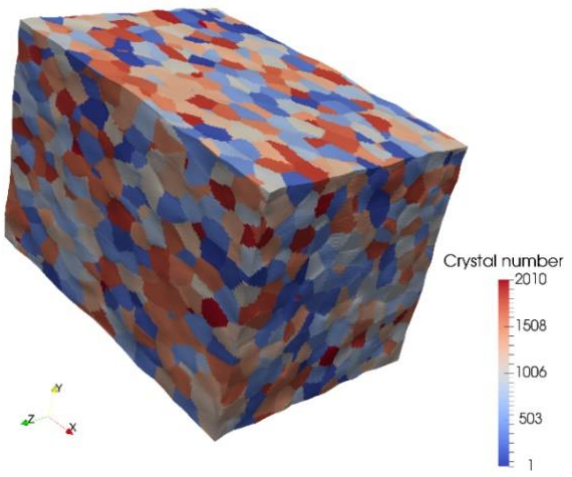

Figure 3.3. Representative volume element of a ca. 2000-grain polycrystal used for the numerical simulation of the elastic properties of an IN625 Inconel polycrystal by means of the FFT homogenisation method.

was used, called FFTMAD. For these simulations, the accelerated scheme[129] was selected for its very good performance using this phase contrast. The Representative Volume Elements (RVEs) were generated using Dream 3D[130], following a typical log-normal distribution of grains. Around 2000 grains discretized in a cubic box of 128 × 128 × 128 voxels were used, as shown schematically in Figure 3.3. The numbers of grains provide an accurate description of the random texture.

The resulting number of voxels per grain (approximately 1000) is enough to provide a good representation of the fields within the superalloy grains[131]. The simulations were carried out imposing a uniaxial strain and the values of the elastic modulus and Poisson's ratio were obtained from the average stress results. For each temperature, ten different RVEs with the same grain distribution were simulated.

3.3. Results and discussion

Exploiting the cubic symmetry of the elemental solids in FCC structure, the electron density was studied along high symmetry lines related to neighboring atoms. We fitted numerically the EAM electron density parameters to match the electron density surface computed at the DFT level. In Figure 3.4 we observe that the electron density calculated with the classical function reproduces well the DFT-obtained electron density.

The values of the cohesive energy, elastic constants, and bulk modulus of Fe obtained with the new IP are in good agreement with the values calculated using DFT. The largest deviation is only 5%, in the case of the C12 constant (see Table 3.2), which is relevant if we keep in mind that Fe does not crystallize in FCC packing.

As we mentioned in the previous section, in the case of Mo-FCC, any small anisotropy (*i.e.*, shear, deformation of the unit cell), results in elastic instabilities. However, the solids show stability towards isotropic compression and expansion, as shown in Table 3.3. The agreement between the DFT and the interatomic potential results for the five pressures studied is very good.

The interaction between two different types of atoms is described by a Buckingham potential (Eq. 3.3). This equation, as we showed before, has two parameters to fit, for which three DFT-derived observables were computed for the parameterization. Again, the fitting procedure is able to provide values in good agreement between the DFT and the interatomic potential results for the different alloys, since lattice parameters and bulk moduli are within 0.6% and the differences in cohesive energies are below 10% (see Table 3.4).

We note that the starting point for the different fits is very important in order to obtain an acceptable agreement between DFT and classic calculations for the five new binary alloys (Ni-Fe, Ni-Mo, Cr-Fe, Cr-Mo, and Fe-Mo). Our method is in this point relevant, as the potentials derived for the monometallic metals are essential to fit the parameters for the alloys. The quality of the computed values of the binary alloys, gives

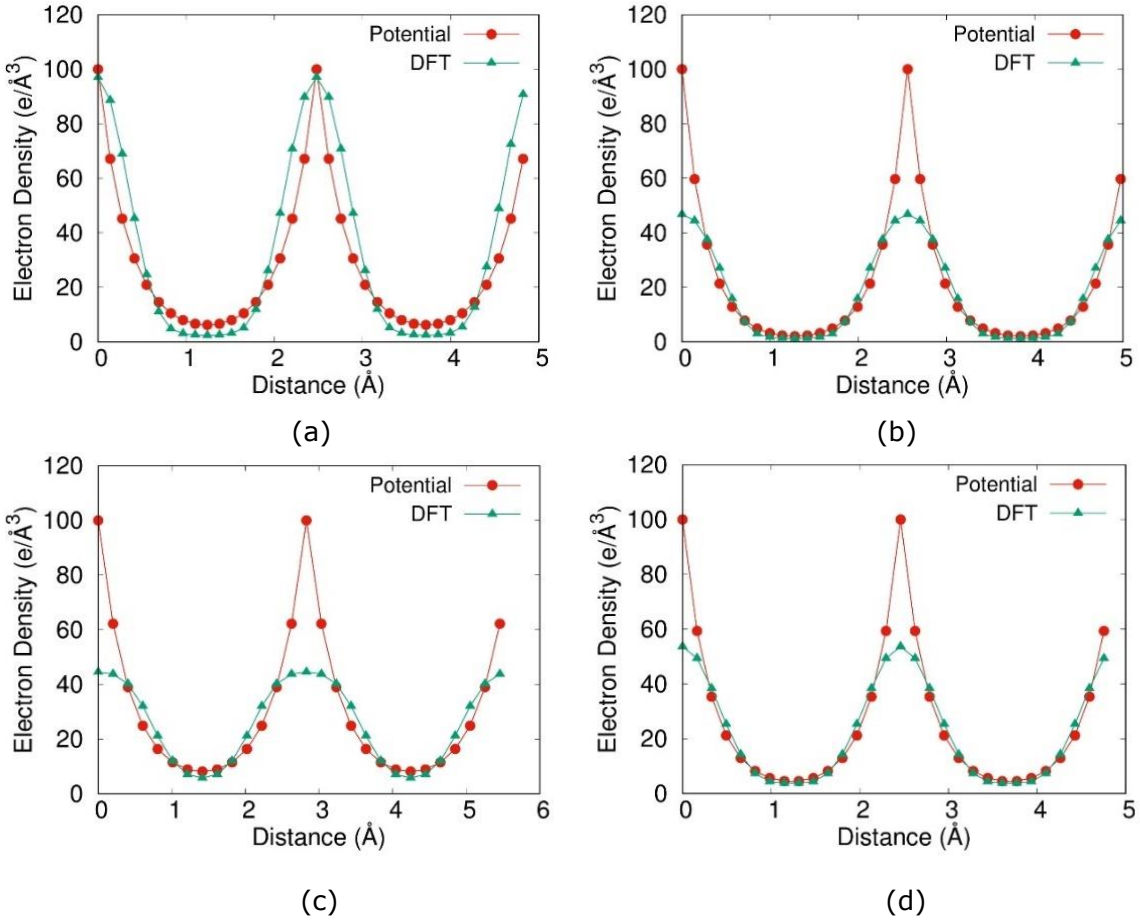

Figure 3.4. Electron density along the diagonal of a unit cell face, computed with DFT (green triangles) and by numerical fitting (red circles) for the elemental metal solids in FCC structure: a) Ni, b) Cr, c) Mo, and d) Fe.

us confidence on the quality of the *ab initio*-derived interatomic potentials. Details of the potential are shown in Table 3.5. The file with all potentials parameters, in the format needed to be used in LAMMPS is supplied as a supplementary information.

As the first validation of the potentials, we computed the thermal expansion of the material, at both low (*i.e.*, below 300 K) and high (*i.e.,* above 300 K) temperatures. The simulated behavior, along with experimental data are displayed in Figure 3.5. It can be observed that the LD simulations are able to capture the rapidly changing behavior of the thermal expansion at low temperature, but it departs from the experimental trend at about 300 K. It is clear that the thermal expansion values computed by MD for temperatures below 300 K are in disagreement with experiments, due to neglecting the zero-point contributions. Our results stress the need of using LD for such purpose in the low temperature regime. The high temperature branch is well described by MD simulations. The slopes of the experimental curves above 800 K increase slightly, in contrast with the simulated curve, probably due to the well-known clustering of minor components that occurs as Inconel 625 ages[142–144].

Our simulations cannot account for this effect, as such clustering appears at time scales that are orders of magnitude higher than those affordable by MD simulations. Note that the cell parameters are within 1% of the experimental values in the entire temperature range (Figure 3.6) and therefore the overestimation of the cell parameters obtained with the simulations

Table 3.2. Comparison of the interaction potential *vs* DFT simulations for Fe: lattice energy, lattice parameter, bulk modulus, and elastic constants.

Fe (FCC)		
Property	DFT	Pot
a (Å)	3.479	3.480
B (GPa)	181	181
E_c (eV)	5.09	5.05
C11 (GPa)	304	294
C12 (GPa)	119	125
C44 (GPa)	181	189

Table 3.3. Lattice energy, lattice parameter, and bulk modulus for elemental Mo solid as a function of the pressure, obtained with DFT and with the developed interatomic potential.

Mo (FCC)					
Pressure (kbar)	a (Å)		B (GPa)		E_c (eV)
	DFT	IP	DFT	IP	DFT
-60	4.041	4.043	218	218	6.49
-40	4.028	4.029	227	227	6.29
-20	4.016	4.016	235	235	6.08
0	4.002	4.003	244	244	5.88
20	3.973	3.970	268	268	5.29

can be considered negligible.

Figure 3.7 represents the distribution of the microscopic fields in the RVE obtained using the FFT algorithm for an applied macroscopic uniaxial strain tensor $\varepsilon_{xx} = E$ and the rest of the values are equal to 0. In particular, Figure 3.7a corresponds to the value of the strain component ε_{xx}, parallel to the applied macroscopic strain, and Figure 3.7b represents the same for the stress tensor component, σ_{xx}. The variations observed in the values of both fields are due to the anisotropic (orthotropic) elastic behavior of the crystals that, for the different crystal orientations, results in a different stiffness.

The maximum differences are found near the grain boundaries due to the elastic incompatibility of the deformation of adjacent grains. This may lead to high local stress concentrations, which induce the initiation of cracks in the material, even when low average stresses are observed macroscopically. This model of the system would be valid only for low and medium temperatures. At high temperatures, in contrast, the grain boundaries behavior plays an important role in cracking so, in order to study the degradation of the material at high temperatures, we would need to model the grain boundaries explicitly within a finite element method framework, which is out of the scope of this study.

Table 3.4. Comparison between the interaction potential *vs* DFT simulation results, for five binary alloys: lattice energy, lattice parameter, bulk modulus, and elastic constants.

Metals (FCC)						
Binary alloy	a (Å)		B (GPa)		Ec (eV)	
	DFT	IP	DFT	IP	DFT	IP
Ni-Mo	3.644	3.655	219	219	-20.31	-21.30
Ni-Fe	3.544	3.523	198	198	-19.95	-17.90
Cr-Mo	3.728	3.745	240	240	-16.79	-18.52
Cr-Fe	3.568	3.572	258	258	-16.51	-17.79
Mo-Fe	3.876	3.880	252	252	-22.92	-23.21

Table 3.5. Parameters of repulsive Buckingham, Johnson functional and electron-density terms of the EAM interatomic potentials developed in this study for Ni-Cr-Mo-Fe superalloys.

Buckingham						
Parameter	Ni-Ni		Cr-Cr	Mo-Mo		Fe-Fe
A_B	6393.9		5804.4	4768.8		4330863.7
ρ	0.27829		0.27800	0.28949		0.14497
Parameter	Ni-Cr	Ni-Mo	Ni-Fe	Cr-Mo	Cr-Fe	Mo-Fe
$\boldsymbol{A_B}$	6675.5	8760853.1	133726.8	12917834	68016.6	3675619.2
$\boldsymbol{\rho}$	0.27759	0.14029	0.22852	0.14512	0.22877	0.16506
Johnson EAM functional						
Parameter	Ni		Cr	Mo		Fe
E_c	4.45000		3.69000	5.09042		5.09042
F_1	4.49058		4.93708	3.09627		10.95780
ρ_0	4.83626		4.08507	1.24594		2.66268
α_J	5.09453		6.03694	6.03694		6.03694
β	6.45654		6.32622	10.1932		33.73605
γ	8.85297		8.89153	4.48959		52.01543
EAM density						
Parameter	Ni		Cr	Mo		Fe
A	0.42133		0.61852	0.06989		0.06290
B	2.67635		2.13582	3.17639		3.71782
r_0	2.48900		2.13582	2.82761		2.41072

The elastic constant at the different temperature values computed by the two homogenisation approaches for polycrystal and by MD for an infinite single crystal are shown in Figure 3.8. It is noticeable that the analytical and the numerical homogenisation methods provide curves very close to each other, while the MD results only differ 2.5% from those of the polycrystal homogenization. The experimental data, taken from references [134–136], are also displayed. The agreement is good, with differences of no more than 10 %, which are common in both computed and experimental elastic constants. Note that properties computed at

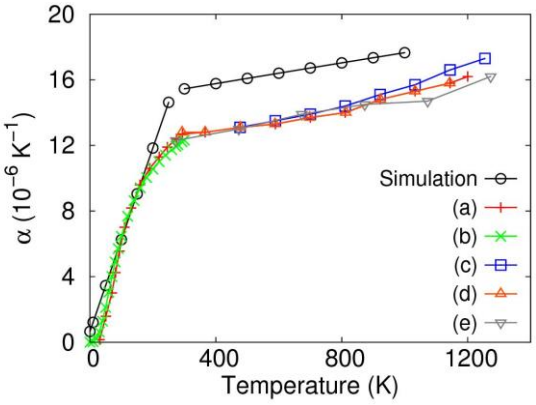

Figure 3.5. Values of the thermal expansion coefficient of IN625, as a function of temperature, calculated with LD at low (below 300 K) and MD (above 300 K), along with experimental results (a) Ref [132], (b) Ref [133], (c) Ref [134], (d) Ref [135], (e) Ref [136].

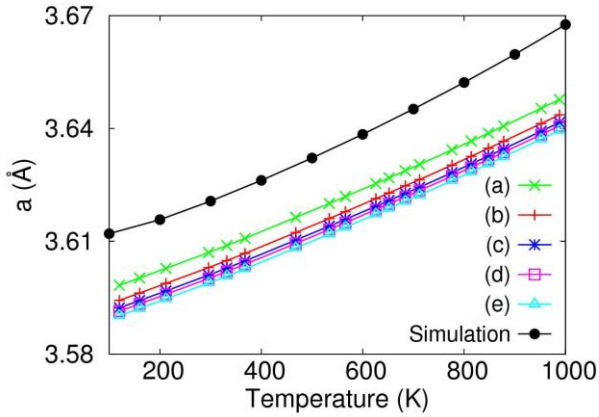

Figure 3.6. Simulated and experimental cell parameters of IN625 (Ni-Cr-Mo-Fe). (a) Ref [137], (b) Ref [138], (c) Ref [139], (d) Ref [140], (e) Ref [141].

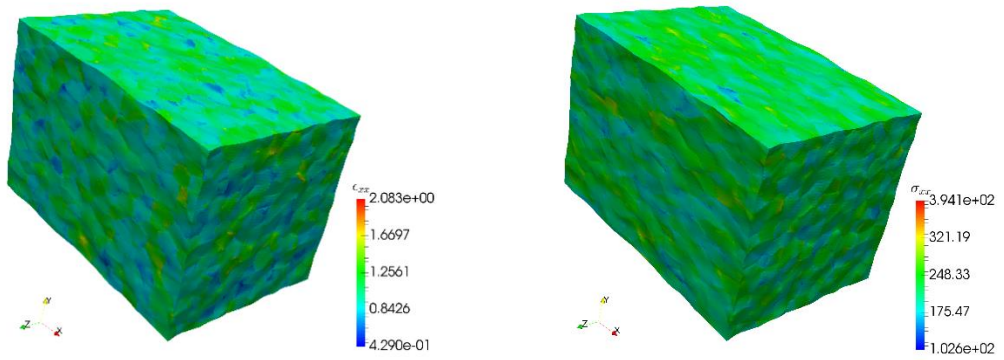

Figure 3.7. Numerical simulation of an Inconel IN625 polycrystal by means of the FFT method. (left) ε_{xx} field distribution, and (right) σ_{xx} field distribution (label in MPa).

finite temperatures were not used during the parameterisation of the potentials.

As mentioned above, one of the consequences of long exposure of Ni-based superalloys to high temperatures is the appearance of aging-related phenomena. In particular, the formation of small clusters of chromium, molybdenum, and iron. The most stable phase for these three metals is BCC. For this reason, it is also important to model with reasonable accuracy their main structural properties. Thus, taking advantage of our ab initio derivation of the interatomic potentials, we used them for the computation of the lattice parameters, as well as the bulk moduli of these three metals in their corresponding BCC phases.

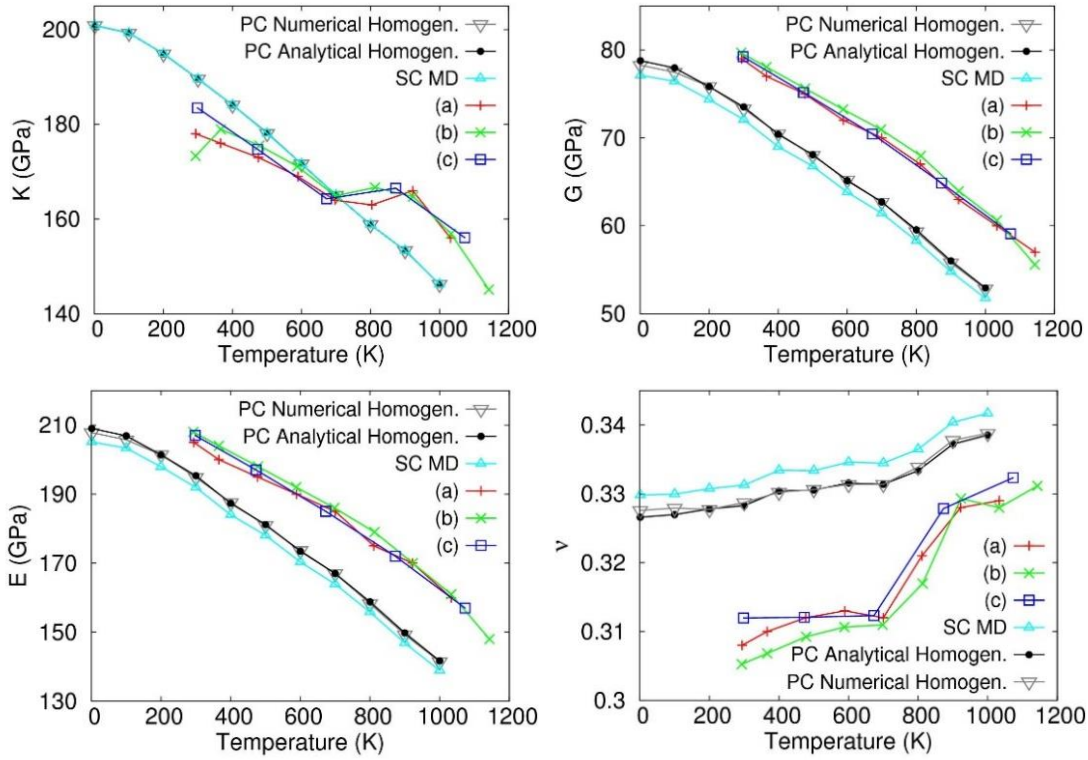

Figure 3.8. Simulated elastic properties of IN625: polycrystal (PC) numerical homogenization, PC analytical (mean-field) homogenization, and single crystal (SC) molecular dynamics (MD); along with experimental results: (a) Ref [134], (b) Ref [135], and (c) Ref [136].

Table 3.6. Simulated and experimental cell parameters and bulk modulus of chromium, molybdenum, and iron in their BCC phase.

Property	Cr – BCC		Mo – BCC		Fe – BCC	
	Exp. [145]	Pot.	Exp. [146]	Pot	Exp. [147]	Pot
a (Å)	2.88	2.88	3.15	3.18	2.86	2.82
Bulk (GPa)	191	198	230	240	169	162

As can be seen in Table 3.6, differences below 1.5% in lattice parameter and below 5% in bulk moduli were found between the experimental and simulated values, despite the fact that the potentials were designed for the FCC phase (Tables 3.2 to 3.4). This opens a possibility for the use of multiscale tools, such as kinetic Monte Carlo, for the study of aging in Ni-based superalloys.

3.4. Conclusions

We have introduced a novel approach for carrying out the parameterisation of EAM potentials, based on the direct fit of their electron density parameters, to reproduce the DFT-computed electron density. This provides a route to develop self-consistent, *ab initio*-derived interatomic potentials for multi-element alloys, as numerical interdependence between the parameters is removed from the fitting procedure. The electron density parameters can then be used to fit the rest of the parameters, which are then easier to obtain, since they can be fitted without changing iteratively the electron density parameters. We have applied this approach to obtain the parameters to model Ni-based superalloy Inconel IN625. The parameters were validated by comparing with the experimental data of thermal expansion and thermoelastic behaviour in a wide range of temperatures. The thermal expansions simulated at low and high temperatures, by lattice dynamics and molecular dynamics, respectively, reproduce accurately the experimental behaviour. The elastic properties computed by the used analytical and numerical homogenisation approaches were also found in good agreement to the experimental data. The interatomic potentials presented in this work are expected to be useful for modelling aging at the atomic level, which is a relevant but still a poorly explored area.

4. Stability of ordered nanoporous metals

The recently discoverd familiy of ordered nanoporous metals is studied here at theoretical level, to determine the factors that affect the stability of these solids. A computational atomistic design approach is used for the construction of a set of new kind of hypothetical solids, some of which are good candidates to be synthesised. Molecular dynamics simulations are conducted on the in-silico constructed solids, for five different metals and variety of structures with varying por sizes. The much cheaper nickel materials appear as potential candidates for applications. The predicted solids show capacity for molecular diffusion, which is relevant for applications in catalysis, separation, nanofiltration, batteries and fuel cells.

4.1. Introduction

Nanoporous materials, like zeolites, MOFs and COFs, featured by large surface to volume ratios, play major roles in current chemical technologies owing to their catalytic, ion-exchange, adsorption and separation properties[148,149]. Recent work has introduced a new kind of nanoporous solids, Ordered Nanoporous Metals (ONMs), with the special feature of being composed only by metal atoms[25]. These authors use MOFs as hard templates for casting nanoporous metals, incorporating K_2PtCl_4 in three MOFs and subsequently carrying out metal reduction and etching with hydrofluoric acid, which is an approach conceptually similar to that used in the preparation of zeolite-replicated carbon (ZRC) materials[150]. The resulting new metal nanostructures exhibit excellent catalytic activities in methanol electrooxidation reactions. A more recent work reports that mesoporous trimetallic PtPdAu alloy exhibits enhanced electrocatalytic activity in methanol oxidation[151].

ONMs could have high relevance in advanced electrodes in batteries and fuel cells, as well as high performance molecular separation membranes. In contrast to traditional porous metals, in which usually there are no connected voids throughout the material, the ordered nature of the porosity in ONMs guarantees overall mass transport in the whole volume, which is of particular relevance in technological applications. The ordered templating hosts not only translate their ordered negative replica topology to the nanocasted ONMs, but also the pore regularity. This is an important property for shape-regulated applications, like adsorption, separation and catalysis.

The clear impact of nanoporous solids in diverse areas strongly encourages theoretical predictions on the structure and stability these new family of materials, ONMs. In their pioneering work, Maboudian *et al*[25]. simulated the structure of three ONMs assuming a continuous occupation of the MOF channels by the metal. Their predicted diffraction patterns were in good

agreement with the experimental ones. This approach relayed on filling the voids with a continuous metal body, however it cannot be applied to its related analogue, zeolite-replicated carbon materials, as the directional C–C bonds impose severe structural constraints. Seven years after the discovery of the ZRCs, Rousel *et al*[152]. used Monte Carlo simulations to absorb carbon atoms that fill the pores and generate ZRCs frameworks[152,153]. They showed the utility of the approach used for building ZRCs models, although the density of the solids was higher than that of the experiments. Two years later, in 2009, Nishihara *et al*. showed that a Lego-like construction of atomistic models using hexagons, pentagons and/or heptagons assembled to graphene sheets can be used as a geometric simulation approach to the structure of ZRCs[154]. Further developments in both approaches have appeared in recent years[155,156]. We note that the widely-used codes that employ the traditional Monte Carlo method (based on sampling of possible displacements and atom insertion/deletion) are expected to show poor performance in designing ONMs, in terms of quality/computational-time ratio. While those codes are a useful to create ZRCs, our preliminary simulations on OMNs showed that the number of atoms (in the order of tens of thousands *vs* only hundreds or few thousands in ZRCs) exceeds the practical limits for efficient Monte Carlo simulations of full loading of porous materials.

Here we conduct a modelling study to explore at atomic level the key-aspects of ONMs, including the relation between the porosity of the porous template solids and the stability of the resulting ONMs, as well as the influence of the nature of the metal. Besides MOFs, we use large pore supertetrahedral solids[157] as hard-templating solids. We also introduce a simple computational approach to carry out the *in-silico* design of stable ONMs. The exploration of the stability of the *in-silico* built ONMs has been conducted by performing large-scale molecular dynamics simulations. Since diffusion is a relevant property needed for adsorption and separation applications, as well as for a more efficient performance in catalytic and electrochemical areas, we compute the diffusion coefficients of water, methanol and ethanol, as well as benzene and the three xylene isomers, ortho, para and meta. The choice of these molecules lies in their relevance to the green sustainable production of fuels and chemical feedstocks (for the first three molecules), and in petro-chemistry (for the xylene isomers).

4.2. Computational details

Our atomistic in-silico design of the ONMs combines a geometric approach to build the initial structures, with structural relaxation. The nature of the bonds in metals, that is not restrictive in directionality, allows the use of a geometrical approach for generating the starting atomistic models. Our procedure proceeds through the following steps: (1) we take a simulation cell of the hard-templating solid and remove all the atoms, thus creating an empty simulation cell; (2) this cell is then completely filled with the metal atoms in the bulk, crystalline phase; (3) the atoms of the original templating structure are inserted again, (4) all the overlapping metal atoms (i.e., all metal atoms at a distance less than the sum of van der Waals radii from any framework atom) are removed; (5) we identify those metal atoms with no connection to other metal atoms, and remove them, leaving the ONMs with the correct connectivity for all metal atoms, and (6) structural relaxation to evaluate the stability. The structural relaxation could modify the initial bulk-like atom connectivity, which was created in the initial geometrical constriction. This is in line with the High Resolution Transmission Electron Microscopy (HRTEM) results on the ONMs samples, obtained by Maboudian *et*

al., which show bulk-like atomic sections[25]. One secondary, but relevant, consequence of the connectivity of the metal atoms is that electronic conductivity is expected to maintain high values, although it might decrease with respect to that of bulk metals, retaining the metallic conductivity as occurs in metal nanowire networks[158], and also in ZRCs[159].

The initial construction of the solids resulted in periodic units containing several thousands of atoms, which precludes the use of Density Functional Theory (DFT) calculations. Therefore, the structural and dynamical properties of the solids were studied by molecular dynamics (MD) simulations with the LAMMPS code[160], using Embedded Atom Method (EAM) interatomic potentials. Since a range of atomic environments are expected to appear in the structures, we have chosen EAMs rather than Modified Embedded Atom Methods (MEAM), which considers angular dependence and therefore might introduce spurious bias. To ensure the accuracy of the calculations, we selected first-principles derived interatomic potentials by Sheng[2]. In addition, for the Ni materials we also included our recently first principles-derived potentials[115], and a second potential was also used for Pt[62]. We use various interatomic potentials to study the same material, with the aim of testing whether the stability of the structures depends significantly on the choice of the interatomic potentials. These potentials have proved to be useful to model different nanosystems[115,161–163]. Details of these potentials are displayed in the supplementary information[115,161–163].

A preliminary set of calculations indicated that some ONMs collapsed after 500 ps of MD simulations, which suggested that long MD runs are required to ensure the assessment of stability of these materials. Since this is a key point in the design of a new class of materials, we conducted 100 ns long MD simulations. In a realistic and challenging test, the simulations have been carried out in the isothermal-isobaric (NPT) ensemble, in order to test the stability with respect to structural collapse. The potential energy and cell parameters were used as fine numerical indicators to assess the stability of the materials. As a result of significant diffusion of the surface metal atoms, non-porous structures are formed after the total collapse of the ONMs at certain temperatures, which is easily observed. However, the two indicators mentioned allow the identification of local collapse before total collapse occurs. The Nosé-Hoover thermostat and barostat were used, with time constants of 0.1 and 2.0 ps, respectively. A time step of 1 fs was employed for the calculations, and 500.0 ps were used for the equilibration. Since atomic rearrangements are expected to occur, due to the structural evolution after the initial *in silico* construction, we tried to avoid large atomic single step motions, to ensure smooth stress relaxation without artificial collapse. For this reason, the time step was chosen to be 1 fs, shorter than the time step that could be used in simulating the bulk metal.

Since one of the primary goals in using metal nanostructured solids is to exploit their potential thermo-structural stability for applications at temperatures well above room temperature, some thermal properties were studied, such as the specific heat at constant pressure (C_p) and the thermal expansion for the temperature range where each ONM is stable. The thermal expansion was studied by means of a series of MD simulations at increasing temperatures, where the temperature was varied slowly enough to permit the system to reach the equilibrium at every temperature. We increased the temperature at a rate of 0.1 K ps^{-1}. The thermal expansion coefficient, α, and the specific heat, C_P, were calculated with the standard procedures, which use the calculated variation of the lattice parameter or the total energy with respect to temperature.

Here, we do not focus on the molecular diffusion in these materials, we just want to know whether they permit diffusion through their pores. The diffusion coefficients of the molecules investigated in the generated ONMs structures were calculated by fitting the Mean Squared-Displacement in the long production time section of the MD simulations at 300 K, and at molecular loadings half of their maximum adsorption capacity, for each molecule. The maximum adsorption capacity for each molecule was estimated from the bulk density of the adsorbate and the void volume fraction inside the metal pore. The MD simulations were carried out in the NPT ensemble, considering long enough simulation times (ranging from 10 to 20 ns), to ensure that the mean square displacement exceeds the lattice parameter of the cell. Water molecules were treated using the TIP3P force field[164]. Methanol, ethanol and the three xylene isomers were modelled following DREIDING force field[165]. The intermolecular interactions between the metal and molecules were simulated with the well-tested force fields by Jalkanen *et al*.[166], and Tarmyshov *et al.*[167], for silver and platinum ONMs, respectively.

The porosity and textural properties s were computed with RASPA code[168], for OMNs, and with Poreblazer[169], for MOFs and ST solids. Besides surface area and pore volume, for all solids, the pore size distribution was used to determine the largest pore aperture in OMNs, while the large cavity diameter (LCD) and pore limiting diameters (PLD) were also determined for MOFs and ST solids.

4.3. Results and discussion

A schematic view of the construction of the ONMs designed in this study is illustrated in Figure 4.1. In order to show the relation between the ONM and the original sacrificial hard template framework

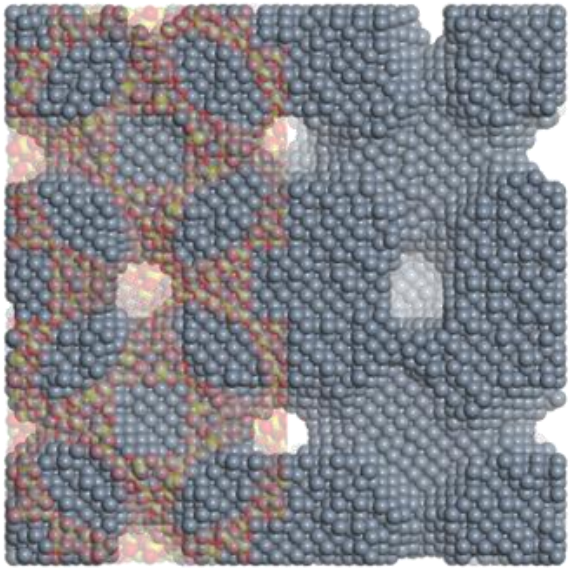

Figure 4.1. Shaded view of a hard template MOF, NDC-MIL-101 (top) and a supertetrahedral solid with SOD zeolite topology (bottom), which are filled with metal atoms to form the ONM (left half of each). ONM obtained once the original sacrificial hard template framework is removed.

in the left side we include a shaded view of the parent solid, NDC-MIL-101 MOF (a) and the supertetrahedral solid with SOD zeolite topology (b), while the designed negative replica ONMs are shown on the right.

In the atomistic design of these materials, we would need to consider the non-directional nature of the chemical bond in metals, as opposed to zeolites and MOFs, where directional bonds stabilize low-symmetry local atomic environments. The lack of such bonds in metals might induce atomic surface diffusion, with a relatively low activation energy. Consequently, the large internal surface of a metallic nanoporous solid would be at risk of structural damage, resulting from the migration of labile atoms, mainly those acting as connectors, and therefore leading to framework collapse. For this reason, we propose to consider nanoporous solids with pore walls built by several atomic layers, to form solids with the pores in the microporous range (from 0.2 to 2 nm). Materials with such features would exhibit

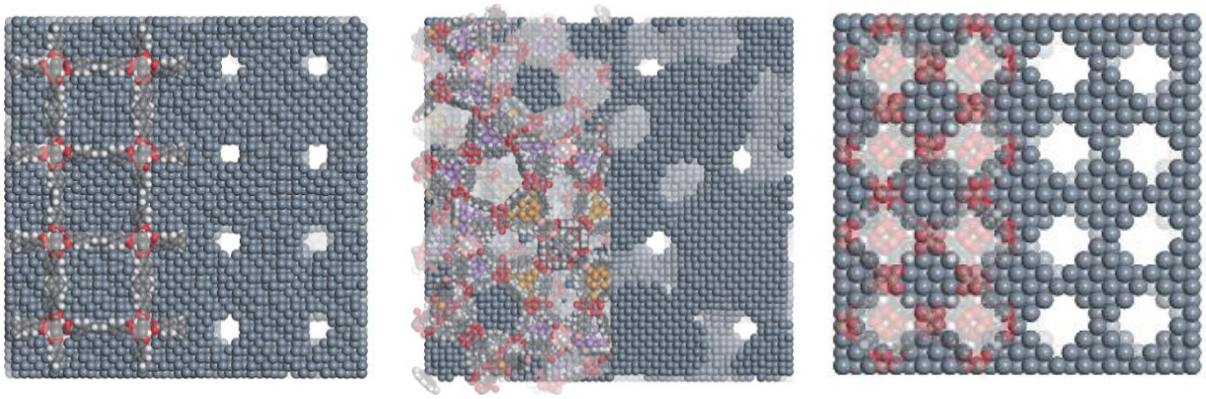

Figure 4.2. Three of the MOFs structures used as templates, namely IRMOF-16, NDC-MIL-101, and HKUST-1, from left to right. The left side of each panel shows the template and the ONM grown within their pores, and the right side shows the ONM once the templating framework is removed.

not only strong interaction with guest molecules or ions, but also high densities of sites with direct contact between diffusing species and the solid. In this context, MIL-100[170], NDC-MIL-101[171], HKUST[172], MOF-5[173], IRMOF-16[16], PCN6P[174], and MOF-500[175] were selected for the study, considering the three-dimensional connectivity of their pores. We note that three-dimensional pore connectivity is necessary to ensure a three-dimensional solid as its negative replica. Since MIL-101 is a highly robust material, the isoreticular, pore expanded solid that is built with the naphthalenedicarboxylate ligand was also considered, although this structure, with larger pores, will give rise to a lower porosity of the templated ONM. However, we do not know in advance which porosity will be needed for ONMs to be stable, so we used isoreticular solids as a way to gain an insight into the relation between the porosity and the robustness of the ONM, to do which, we also employed isoreticular supertetrahedral (ST) solids. In ST materials, each single tetrahedral (T, *e.g.* T = Si, Ge) node of a topological template structure, like a zeolite, for example, is replaced by an entire larger tetrahedral node[157]. If the entering tetrahedral node is a TX_4 tetrahedron (*e.g.* X = O, S, Se), in replacement of a tetrahedral atom, a second level supertetrahedral solid (ST2) is formed. Subsequent replacements lead to higher level supertetrahedral, *e.g.* ST3, ST4 and ST5. We built GeS_2 supertetrahedral solids *in-silico*, using the Tobunporous code[176,177], which automatically based on any desired topology used as topological structural template and rescaling appropriately the cell parameters. An example of a supertetrahedral solid built in this way is shown in Figure 4.1, while in Figure 4.2 we show three of the solids built by templating with MOFs.

Maboudian *et al.* used Pt and Pd for the preparation of their pioneering ONMs. Here, in addition to these metals, we use two other noble metals (Au, Ag) and Ni. The inclusion of Ni in the study responds to economic factors, and is supported by the catalytic properties and thermostructural stability of Ni nanostructures[9]. Changing the nature of the particular interatomic interactions might result in different stabilities, which is clearly relevant to the design strategies in materials discovery

Once all the targeted ONMs solids were designed *in silico*, the structures were subjected to an analysis of their structural features and their stability. We focused on the influence that the level of porosity has on their thermo-structural stability. The as-generated structures were firstly subjected to a lattice energy minimization to relax the solids, which removed the large, initial

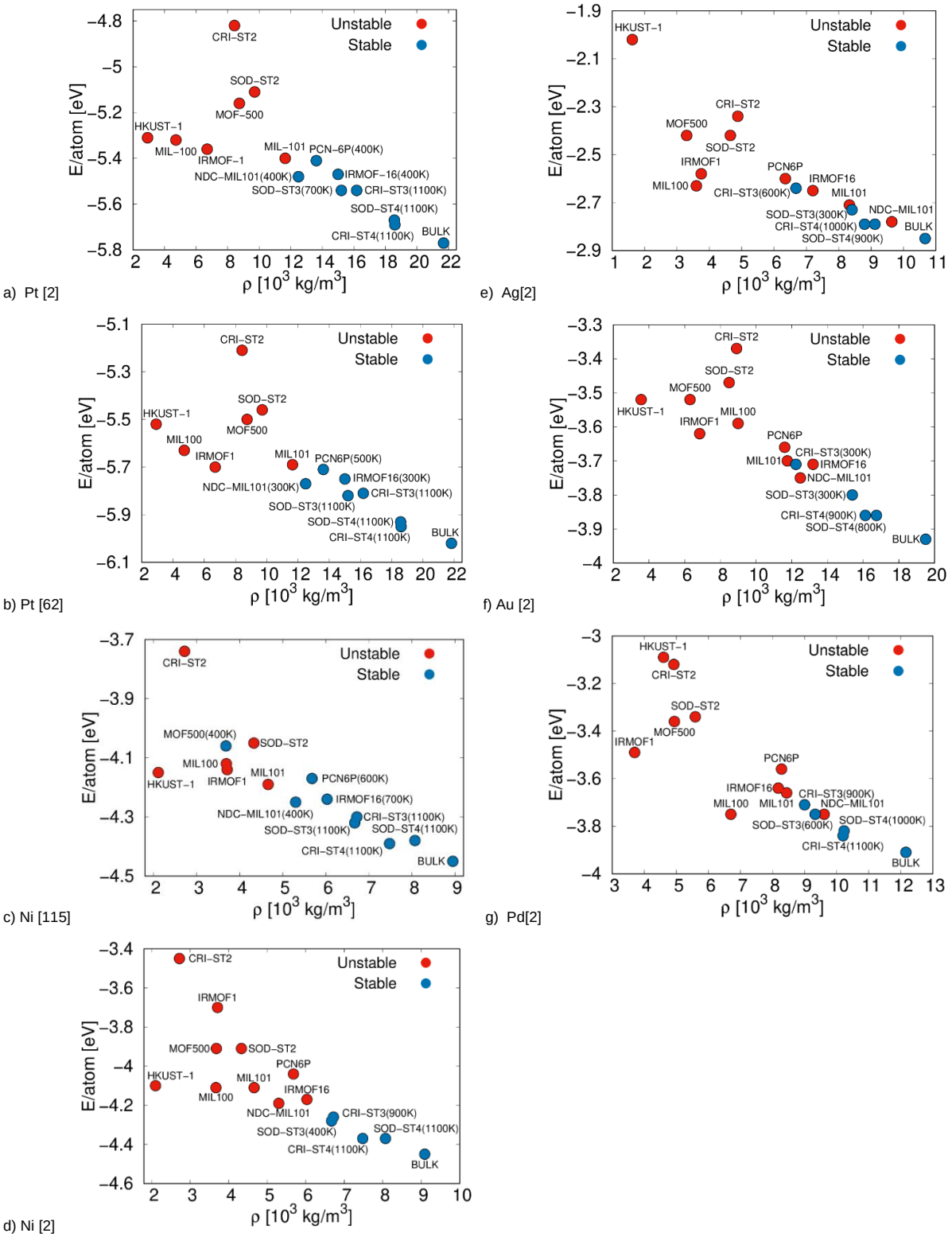

Figure 4.3. Energy per atom vs. density, for all structures studied. In parenthesis, next to the atomic symbol, we show the reference of the interatomic potentials used in each case. Stable structures, in blue, are accompanied by the highest temperature at which they are stable. Structures in red are not stable.

forces, originating at the low coordinated atoms. Then, long MD simulations (100 ns) were performed to assess the stability of the structures. In order to gain a better insight into the behaviour of the materials, the MD simulations were carried out in the NPT ensemble. We also noted that the artificial constraint imposed in canonical MD simulations, associated with the use of fixed cell parameters, precludes the use of such simulations, since unstable structures erroneously appear as stable.

The MD analysis of the framework stabilities (see Figure 4.3) shows that some of the structures collapse at the beginning of the MD simulations, but there are other very stable structures, for which the ONMs can withstand very high temperatures, even above 1000 K, while still keeping their crystallinity. The stable structures are those built from both supertetrahedral solids, with sodalite (SOD-ST3, SOD-ST4) and cristobalite topologies (CRI-ST3, CRI-ST4), and from a number of MOFs structures (NDC-MIL-101, PCN-6P, MOF-500 and IRMOF-16). Figure 4.3 plots the energy per atom *versus* the density of the metal structures obtained, since an important factor that influences the possibility of synthesising a particular structure is the relative energy with respect to the most stable structure of the material (in our case the bulk metal). This scheme has been useful for instance to predict the structural stability of very complex polyoxometalate-based MOFs, which have been successfully synthesised[178]. In figure 4.3, those structures that are stable after 100 ns of NPT MD simulations are coloured in blue, and in red the unstable structures. For each stable structure, the temperature at which structural collapse occurs is also shown in the figure, in parenthesis. The structures remain porous after the long MD simulations, as revealed by their pore size and surface area, ranging from 4.8 to 10.9 Å and 340 to 1500 m^2/cm^3, respectively (see further details in the Supplementary Information).

It is clear that Ni and Pt are the best candidates for preparing robust ONMs with various topologies. Au and Ag ONMs show low stability, only ST3 and ST4 ONMs of these metals are stable at temperatures above room. The low stability of Au- and Ag-based ONMs can be ascribed to the facility with which metal surface displacement can take place. From a macroscopic viewpoint, this is can be linked to lateral deformations of the bulk solids, with atomic layers displacing one on top the other. To analyse this hypothesis, exploiting the symmetry of the parent solids, we calculate the C_{44} elastic constants, which characterize shear deformations[179], and it was found that the highest values are those for Ni structures, followed by Pt and Pd. On the other hand, Au and Ag have the smaller values for these elastic constants. For example, in the case of the structure SOD ST3, C_{44} is 60 GPa for the Ni structure. For Pd and Pt, C_{44} is *circa* 40 GPa, and 20 GPa for Au and Ag. For the sake of comparison, the experimental values of C_{44} for the bulk Ni, Pd, Pt, Au and Ag metals are 132, 71, 77, 45 and 51 GPa[180–184], respectively, so the new materials could withstand significant shear deformations, about half of the bulk metals. Comparing our predictions for the five metals and looking at the experimental results of Maboudian *et al.*[25], who were able to prepare Pd, Pt and Rh ONMs, we can speculate that Ni-ONMs are strong candidates for experimental synthesis, as we have found more stability in Ni ONMs than in Pd ones.

Figure 4.3 also permits us to perform an analysis of the influence of the potential on the thermo-structural stability of ONMs. We observe that, when two potentials are employed to model the same material (as is the cases of Pt and Ni), they both give rise to a very similar qualitative picture. This observation provides support for the validity of the conceptual design of these new materials, since it gives additional confidence as to the stability of the predicted materials. In these materials,

although the same ONMs are stable for the two potentials used, we observe some quantitative differences, which show that the development of interatomic potentials to model complex nanostructured metals is a challenging task. The main discrepancy lies in the stability of Ni ONMs, since the Ni SOD-ST3 structure collapses at 1100 K for one interatomic potential[115] and at 400 K for the other[2] and the MOFs-derived ONMs are not stable with the interatomic potential developed by Sheng *et al.* One route for developing better potentials would involve using a range of low-symmetry configurations for the parameterization based on first-principles calculations. It would also be necessary to test different many-body potentials like MEAM or bond-order potentials[60,185]. However, we consider that the qualitative conclusions retrieved from our studies are robust, considering the independence on the parameterization of the two potentials used.

Further interesting information arising from Figure 4.3 is the observation of a limiting density (for instance a density of circa 12000 kg/m^3 in the case of Pt), below which the ONMs are unstable. To put this into perspective, we can compare with the density of zeolites. Stable ONMs densities are ca. 50 % of their dense counter parts, i.e. bulk metals, while the densities of silica zeolites are in the relative range 46-66 % with respect to quartz, the corresponding dense material. Hence, the main conclusion we draw from this figure is that the present computational study strongly suggests that these materials are thermally stable and strongly encourages the feasibility of their synthesis, since the difference in energy between the most stable, bulk structures and the porous structures is of the same order of magnitude as that observed in zeolites[176]. Zeolites are less stable than their dense counterpart, quartz, but they are, nevertheless, very stable materials. We can use the results of our computational study to guide the search for new stable materials, as based on our simulations for

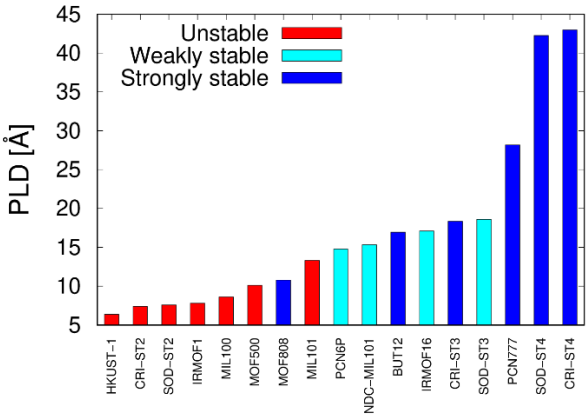

Figure 4.4. Pore limiting diameters (PLDs) of Pt-based ONMs, with the 14 different topologies investigated

the various metals, the templating materials CRI-ST4 and SOD-ST4 using Ni, Pd or Pt would give rise to ONMs that would have very similar stabilities to those of the bulk metals, so they might be the first option when trying to synthesise this new family of porous materials. Moreover, it would be possible to introduce a controlled percentage of other metals in order to increase the hardness of the materials, using the well-known method of solid-solution hardening. The introduction of other metal species could also help to tune the catalytic properties of the materials.

To see whether it could be possible to predict the stability of OMNs from structural descriptors of a given MOF or ST solid, we analyse the porosity and textural properties of the 14 solids used here as templates. We have focused on Pt-ONMs, considering their successful experimental synthesis and the theoretical results that identify this element as one with which to create stable hypothetical ONMs. We found that the pore limiting diameters (PLDs) of the predicted stable ONMs (Figure 4.4) are in the range [14.76 Å, 42.96 Å], while in the unstable ONMs they are within [6.37 Å, 13.31 Å].

The PLDs of the three experimental structures templated with MOFs (synthesised by Maboudian *et al.*[25]) are

10.80 Å (from MOF-808), 16.94 Å (from BUT-12) and 28.17 Å (from PCN-777). The two latter lie in the interval we predicted for the stable ONMs, while the PLD of MOF-808 is smaller than that of the unstable MIL-101. To rationalize this apparent controversy we must note that MIL-101 has two types of pores. The PLD is given by hexagonal windows delimiting the entrance to the larger pores, while the 10 Å diameter pentagonal windows delimit the smaller pores. This is a space that can be occupied by metal atoms, but it is likely that it does not yield a robust enough structure, as is in the case of MOF-500, which has a PLD of 10.12 Å. We then speculate that the collapse of the smaller metal units formed at the pentagonal windows of the MIL-101 might trigger the collapse of the whole material. This resembles the collapse of MOFs upon desolvation, triggered by capillary forces[186]. Further studies in this direction will provide a conclusive understanding in this respect. Note that the isoreticular NDC-MIL-101, with 15% larger pore windows, forms a stable ONM. The appearance of a minimum value of PLD of the template porous solids as a requisite for preparing stable ONMs is in line with our view of lateral internal surface atomic diffusion as the key-point controlling the stability of ONMs. In our modelling study, the smaller PLD of a porous host that yielded stable ONMs can be empirically described by the following equation (see Supplementary Information):

$$PLD_c = 2R_{vdw} + 7.50R_{atom} \quad (4.1)$$

where PLD_c is the critical PLD for a valid template, and R_{vdw} and R_{atom} are the van der Waals and atomic radii of the ONM-constituent metal. The large cavity diameter (LCD) of the template host solids does not play a controlling role in the stability of the ONMs, neither the accessible surface area and the accessible helium void fraction. Details of the computed porosity and textural properties are compiled in the Supplementary Information.

Since these materials are likely to be used in applications at which there are significant changes in temperature, we have also studied their thermal behaviour. In Figure 4.5 we show the results obtained from the analysis of the heat capacities, calculated from MD simulations. The computed values for five out of the seven solids fall close to those of the bulk structures. A slight departure is observed for cristobalite ST3 ONM, and large differences appeared for NDC-MIL-101 and sodalite ST4 ONMs. We did not find any direct connection between the structure of these solids and the computed heat capacity behaviour with temperature. The thermal expansion (also shown in Figure 4.5) also appears to be uncorrelated. However, there is a wide span of calculated values, with one solid unexpectedly showing nearly zero

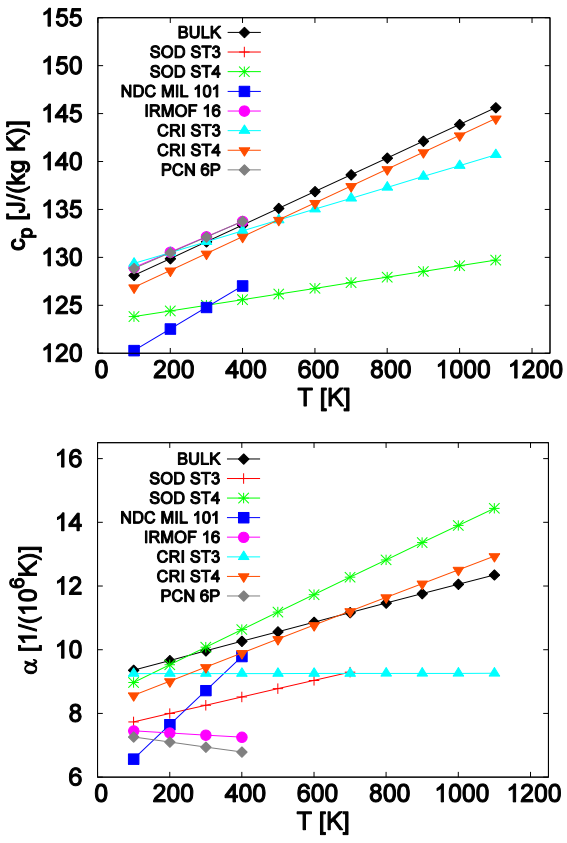

Figure 4.5. Specific heat (left) and thermal expansion coefficient (right), and for the ONMs generated with platinum and modelled with the interatomic potential developed by Sheng et *al*[2]. The final temperatures for each structure are those at which each material collapses.

thermal expansion (cristobalite ST3 ONM) and two with negative thermal expansion (IRMOF-16 and PCN6P ONMs). To our knowledge, zero and negative thermal expansivity have not been predicted before for nanoporous solids built by one elemental metal. The open framework nature of these solids could be the reason behind this uncommon behaviour, which frequently occurs in traditional microporous solids, such as zeolites[187,188] and MOFs[177,189,190], and also non-porous framework materials like ZrW_2O_8 and quartz[191]. This interesting finding might open a new area of research in the field of thermal materials.

Table 4.1. Diffusion coefficients of benzene, orthoxylene, metaxylene, paraxylene, water and methanol, calculated with MD simulations in various Ag- and Pt-based ONMs. We have used the force fields a[166] and b[167] for modelling the interactions between structures and molecules, and the force fields c[165] and d[164] for the molecules themselves.

ONM (ff)	*Molecule (ff)*	*D [10^{-9} m^2/s]*
Ag CRI ST3 (a)	Benzene (c)	1.5
Ag CRI ST3 (a)	Orthoxylene (c)	0.2
Ag CRI ST3 (a)	Metaxylene (c)	0.4
Ag CRI ST3 (a)	Paraxylene (c)	0.3
Pt CRI ST3 (b)	Methanol (c)	1.4
Pt CRI ST3 (b)	Water (d)	1.1
Pt PCN 6P (b)	Methanol (c)	1.4
Pt PCN 6P (b)	Water (d)	1.3
Pt NDC MIL 101 (b)	Methanol (c)	1.4
Pt NDC MIL 101 (b)	Water (d)	1.6

The development of new metallic nanostructured solids, as for instance metal nanoparticles or nanorods supported on different materials[192,193], is still crucial for several applications such as in catalysis.

In order for these materials to be used in separation, molecular-enhanced heat exchange, or catalysis applications, the stable structures should be able to allow the flow of molecules at a rate comparable to other microporous solids. We therefore computed the diffusion coefficients of four relevant molecules (benzene, o-xylene, m-xylene and p-xylene), within the Ag-CRI-ST3 structure, and the diffusion of water and methanol within the structures Pt-CRI-ST3, Pt-PCN-6P and NDC-MIL-101.

From the data shown in Table 4.1, we can conclude that, since diffusion coefficients are of the order of 10^{-9} m^2/s, which is of the same order of magnitude as for diffusion in zeolites[194] and MOFs[195,196], these materials could have the required flow of molecules to allow their use in some relevant industrial applications. For example, if we compare the diffusion coefficients at 300 K of the three isomers in the silver Ag-CRI-ST3 structure, we observe that the three xylene isomers diffuse at different rates, so this structure could be used to separate differentially mixtures of these molecules. The fact that the diffusion coefficients are of the same order of magnitude as those observed in MOFs and zeolites suggests that the relative large dispersion interactions from all atoms of the ONMs is equivalent to the combined electrostatic and relatively weak dispersion interactions in MOFs and zeolites.

4.4. Conclusions

To summarise, in this work we have developed an *in-silico* strategy for the design of ordered nanoporous metals (ONMs). We have shown that besides MOFs, previously used in the pioneering work of this novel family of solids, supertetrahedral

solids can be also used as reverse templates for growing their "negative" replica metal structures. Some of the ordered metal structures thus formed are predicted to withstand temperatures as high as 1000 K, and we rationalize the stability of the ONMs based on the porosity of the parent material and the nature of the shear elasticity of the constituent metal of the metallic nanostructure. It has been found that the PLD of the template host can be used as a descriptor for selecting potential porous materials for the preparation of ONMs. Ni-based ONMs are predicted to be strong candidates for applications, considering their robustness and their competitive price, compared to Pt and Pd, which are over 1000 times more expensive. We also found negative and zero thermal expansion in some of the studied solids, which could trigger experimental research looking for the development of new advanced nanoporous materials. Due to the high surface area of these structures, the most relevant applications are expected to be in the fields of separation and catalysis, particularly in thin membrane technologies where the molecular sieving features can be combined with high thermal and chemical stability, as well as the high electronic conductivity intrinsically associated to metallic materials. As a prerequisite for such applications, we have shown the feasibility of molecular diffusion of molecules representative of those used in renewable and traditional fuels industries. Our approach can lead to the prediction of a library of hypothetical ONMs that can stimulate further synthetic work.

5. Design and thermostructural characterization of new siliconized Silicon Carbide composite materials with applications in solar energy harvesting

In this chapter, we design a new Silicon-based nanomaterial, with good thermostructural properties, which can be used to build tubes for central receivers in solar power plants. The new material is formed by SiC crystalline nanoparticles (with either cubic or hexagonal phases), embedded within an amorphous Si matrix. We have followed an *in silico* approach to characterize the mechanical and thermal behaviour of these materials, , such as the elastic constants, uniaxial stress-strain curves, coefficient of thermal expansion, and specific heat, at different temperatures, combining both atomistic and continuum-based simulations. In the first place, we have studied the performance of different interatomic potentials available in the literature, namely 2NN-MEAM and Tersoff type potentials. We selected the potential that performs better than the rest, and we have employed it to predict the properties of the new composite materials here designed. The results obtained from these atomistic simulations are used to feed finite element simulations that permit the study of the materials at higher scales, both at the microscopic level (which allows accounting for microstructural aspects such as shape and size of the particles) and at the macroscopic level (which allows the study of SiC-based tubes of the central receivers, enhancing the thermal resistance with respect to other materials currently used). From this study we observe that this new type of material presents enhanced thermal resistance features, making it suitable for solar energy harvesting applications at high temperature.

5.1. Introduction

One of the main challenges of solar energy technologies is the reduction of the cost of electricity. This objective can be accomplished in various ways, such as developing high-capacity thermal energy storage systems, improving solar radiation absorption, or increasing cycle efficiency[197–199]. An increase in the operating temperature of solar plants is then demanded and, in some cases, expected to surpass 1000 K. Unfortunately, the increase in temperature also implies a decrease in the performance of materials. For this reason, alternatives to conventional high-temperature superalloys, which on the other hand present long-term ageing effects, must be found[115,200–202]. It is within this context that ceramic materials may become an interesting solution, for two main reasons. On the one hand, from the harvesting point of view, low thermal

expansion and high absorbance[203,204]. On the other hand, from a storage point of view, due to their high conductivity and reasonable heat capacity[205]. And, most important and in both cases, due to their high thermal stability.

In this article, we present a three-scale study of a new type of nanomaterial with possible applications in solar receivers. We have created *in silico* a new type of nanocomposite material, formed by SiC nanoparticles (much smaller than the micrometre size particles usually obtained[206]), in alpha (i.e., hexagonal) and beta (i.e., cubic) phases inserted within an amorphous Si (a-Si) matrix. First, we have performed a comparison of the performance of five of the best force fields available to model a-Si and SiC, in order to choose the one that best describes the thermostructural properties of interest in our study. Once we have selected an appropriate force field, we have carried out Molecular Dynamics (MD) simulations of the systems, to obtain the structural (i.e., stress-strain curves, coefficient of thermal expansion) and thermo-physical properties (i.e., specific heat) at different temperatures. The information obtained from the MD simulations, with atomic detail, is then fed into a lattice model[207], which can provide information about the behaviour of the system at larger length and time scales. The goal is to develop different representative volume elements (RVE), including the previous phases, in order to analyse the effect of the composition, geometry, and temperature on the global properties of the microstructure. Finally, the material information computed at this scale is subsequently input at macroscopic finite element models to design the receivers under different operating conditions.

5.2. Simulation details

In this section we present the computational strategy followed in the design process of the material and the component built with it. In the first place, the atomistic models to characterize the individual phases observed at the atomic scale (i.e., $\sim 10^{-9}$ m) are used. This information is subsequently implemented into the micromechanical model (i.e., $\sim 10^{-3}$ m) which provides the constitutive behaviour of the material used later in the macroscopic simulations (i.e., $\sim 10^{0}$ m).

5.2.1. Atomistic model

The MD simulations have been carried out with the open-source code LAMMPs[160]. The materials are modelled using interatomic potentials developed for reactive covalent systems, which include the possibility of breaking and forming covalent bonds. Chemical bonds vary in strength depending on the local bonding environment, *via* bond-order potentials. We have used five potentials pertaining to two different potential types: Second Nearest Neighbour-Modified Embedded Atom Method (2NN-MEAM), with certain modifications to include in their interactions the nearest second neighbors[34,71], and Tersoff[35,37,208] potentials.

In this work, we will focus on the interaction between 3C-SiC and a-Si, in two different types of composite materials: plane interfaces between them with different densities, and systems of 3C-SiC NPs embedded within an a-Si matrix. These NPs are located following a Body Centred Cubic (BCC) symmetry, that is, one in the corners of the cell and another in the centre of it. As for the flat interface systems, we have built five systems with densities ranging from 2.65 g/ml to 2.97 g/ml, using a fixed 3C-SiC thickness and varying the a-Si thickness. On the other hand, we have built five systems of SiC NPs in an a-Si matrix with densities from 2.30 g/ml to 2.63 g/ml, varying both the size of the NPs and of the cells.

In order to obtain results as accurate as possible, we have checked which force

fields describe better the thermal and structural properties of the single systems. We have studied five different force fields, two of them are of the Embedded Atom Method (EAM). The remaining three are of the Tersoff type. There is a large number of potentials with which it would be possible to study SiC and a-Si systems, but these five potentials are the ones that best describe the characteristics of interest for this study, according to the literature reviewed.

The 2NN-MEAM potential was created by Baskes[209,210] by modifying the MEAM to partially consider second nearest-neighbour atom interactions and to remove some critical shortcomings in the original MEAM. It is thus suitable for modelling metal and alloys, with fcc, bcc, hcp, and diamond cubic structures, as well as covalently bonded materials, such as silicon and carbon. In the MEAM formulation, the total energy of a system of atoms is given by:

$$\boldsymbol{E} = \sum_{\boldsymbol{i}} \left[\boldsymbol{F_i}(\boldsymbol{\rho_i}) + \frac{\boldsymbol{1}}{\boldsymbol{2}} \sum_{\boldsymbol{i \neq j}} \emptyset_{\boldsymbol{ij}} (\boldsymbol{r_{ij}}) \right] \qquad (5.2)$$

where F is the embedding energy, which is a function of the atomic electron density $\boldsymbol{\rho}$, and $\emptyset$ is a pair potential interaction, between atoms $\boldsymbol{i}$ and $\boldsymbol{j}$. The pair interaction is summed over all neighbours within the cut-off distance, 4 Å. The multi-body nature of the MEAM potential is a result of the embedding energy term. Two different sets of 2NN-MEAM potential parameters were used[34,71].

The family of potentials developed by Tersoff[211,212] are based on the concept of bond order, giving to the local environment the key to stablish the strength of the interaction between atoms. In this case, this strength is not constant, expecting to reproduce better dynamic models, where the environment strongly varies. Despite the presence of the two terms in a Tersoff potential (an attractive one and a repulsive one), they are not considered pair potentials, since the coefficient in the attractive part is not constant. We have used three different Tersoff potentials[35,37,208].

The validation of the different force fields is made against a series of experimental data, for various thermal and mechanical properties, such as elastic constants and uniaxial tensile tests of the systems. Elastic constants characterize the stiffness of a material, and its formal definition is provided by the linear relation that holds between the stress and strain tensors in the limit of infinitesimal deformation. In tensor notation, this is expressed as:

$$s_{ij} = C_{ijkl} \cdot e_{kl} \qquad (5.2)$$

where the repeated indices imply summation. $\boldsymbol{s_{ij}}$ is the stress tensor, $\boldsymbol{e_{kl}}$ is the strain tensor, and $\boldsymbol{C_{ijkl}}$ is the fourth-rank constitutive tensor. In three dimensions, this tensor has 81 elements. Using Voigt notation, the tensor can be written as a $\boldsymbol{6 \times 6}$ matrix and $\boldsymbol{C_{ij}}$ is now the derivative of $\boldsymbol{s_i}$ with respect to $\boldsymbol{e_j}$. $\boldsymbol{C_{ij}}$ is symmetric with, at most, 21 distinct elements. However, a material hardly presents no symmetry in space. Thus, in the case of a material with three independent planes of symmetry, also known as orthotropic, there are 9 independent elements. If the material presents symmetry in those planes, i.e., it behaves similarly regardless of the direction considered, the material is known as linear elastic isotropic and is defined by only two elements, the so-called Lamé's parameters.

At zero temperature, it is easy to estimate these derivatives, by deforming the domain (i.e., the MD simulation box) in one of the three directions. Once the elastic constants are determined, we compare our results with experimental results.

The isotropic bulk module $\boldsymbol{B}$ is the relationship between hydrostatic pressure and volumetric deformation, and is given by the following expression:

$$B = \frac{C_{11}+2C_{12}}{3} \qquad (5.3)$$

We can determine Young´s modulus $\boldsymbol{E}$, Shear modulus $\boldsymbol{G}$, Poisson's ratio $\boldsymbol{\nu}$, and the elastic anisotropy factor $\boldsymbol{A}$, from the elastic constants, as follows:

$$E = \frac{(C_{11}+2C_{12})(C_{11}-C_{12})}{(C_{11}+C_{12})} \quad (5.4)$$

$$G = \frac{C_{11}-C_{12}+3C_{44}}{5} \quad (5.5)$$

$$v = \frac{C_{12}}{2(C_{12}+C_{44})} \quad (5.6)$$

$$A = \frac{2C_{44}+C_{12}}{C_{11}} - 1 \quad (5.7)$$

The elastic anisotropy factor is zero for an isotropic material. Any value smaller or larger than zero indicates a certain level of anisotropy, and thus measures the degree of elastic anisotropy of the crystal.

Another mechanical parameter analysed in this work is the coefficient of thermal expansion (CTE), which measures the volumetric expansion of the material with the rise of temperature:

$$\boldsymbol{\alpha = \frac{1}{V} \cdot \frac{\partial V}{\partial T}} \quad (5.8)$$

where $\boldsymbol{V}$ is volume and $\boldsymbol{T}$ is temperature. To calculate this coefficient, we compute the lattice parameter and the temperature of the system from 100 K to 1000 K.

With regard to thermal properties, we study the specific heat, $\boldsymbol{c_p}$, which is the amount of heat needed to raise 1 K its temperature, per kilogram of substance. We calculated it, at constant pressure, for temperatures between 100 K and 1000 K.

5.2.2. Micromechanical model

For the microstructural analysis of the material, namely the assessment of its thermo-mechanical behaviour, the so-called lattice model[207] is used. Lattice models have been successfully used in the last decade for the characterization of the mechanical behaviour of quasi-brittle heterogeneous materials[213–217]. In fact, at the microscale, SiSiC resembles a heterogeneous structure. Thus, the lattice model becomes a suitable tool for its numerical analysis.

a) Mesh Generation. The main aspect of a lattice model is the discretisation of the material structure, which is described by a network of one-dimensional elements representing the mechanical (and thermal, in this study) interaction between material volumes. In order to account for its internal heterogeneity, the material microstructure is mapped onto this network of elements. Thus, depending on the phase it represents, each element is assigned specific local material properties.
Regarding geometrical aspects, regular meshes (e.g. parallel/perpendicular), although simpler, are not usually used, in order to avoid numerical bias difficulties to obtain realistic values of the Poisson's ratio[218]. Instead, the domain is divided into a grid in which nodes are randomly placed. The mesh is then constructed following a Delaunays's triangulation from the nodes, ensuring an irregular arrangement

b) Microstructure Generation. As pointed out above, SiSiC exhibits a heterogeneous material structure at the microscale with the following phases: a-Si matrix, large SiC grains (in alpha and beta phases) and interfacial transition zone (ITZ) between the matrix and the grains. These phases must be accounted for in the microstructure generation.

The microstructure can be generated either by numerical approaches[219,220], using image-based techniques[221], or a combination of both[222]. In any case, the resulting microstructure must be statistically representative of the material at such scale, yielding the so-called representative volume element (RVE). Different experimental works[223–226] set the range within 5 and 50 μm. In this work, we consider an RVE of 15 μm, which is large enough so as to include several SiC particles and we present a novel approach to generate the microstructure numerically.

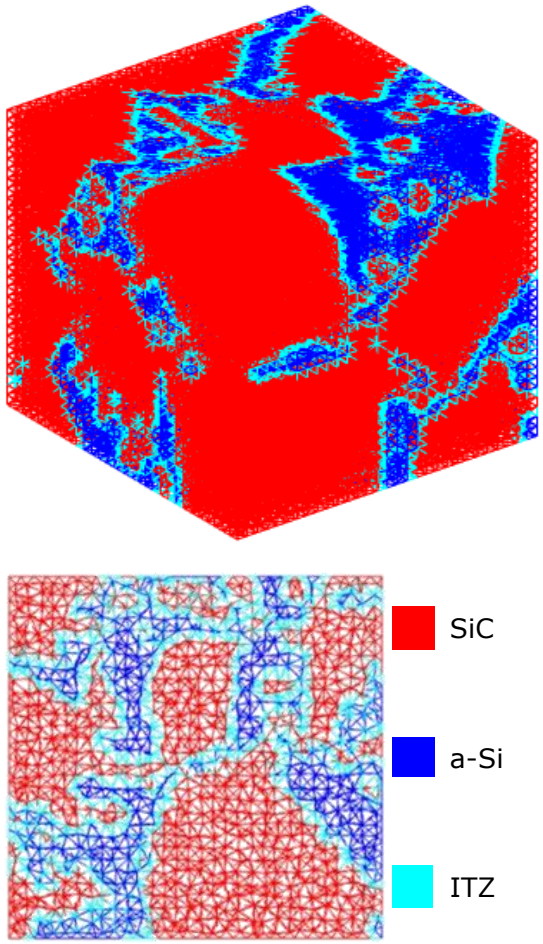

Figure 5.1. Virtual SiSiC microstructure and corresponding lattice microstructure: a) isometric view of the microstructure and b) cross section.

Firstly, the particle distribution inside de RVE is generated following the take-and-place method[227]. Three different sizes of ellipsoidal grains, which will be used as the construction basis for the crystals, are considered. An 80% volume content of grains is assumed, which is in accordance with experimental observations[228]. Then, $\boldsymbol{n}$ random points from the ellipsoidal surface are chosen (in this work, the number of points is set to $\boldsymbol{n = 20}$). These points will later become the vertices of the polyhedra. Finally, these polyhedra are placed within the RVE domain and overlapping is not allowed. Once the particles are generated, these are mapped onto the mesh. Then, if a node of the mesh lies inside a particle, the node is identified as *SiC grain node*. If the node lies outside a particle, the node is identified as *Si-matrix node*. Finally, three possible types of element are defined depending on the node connectivity: *a-Si element* (both nodes are of the type Si-matrix), *SiC element* (both nodes are of the type SiC grain), and *ITZ element* (otherwise). This ITZ element represents the interface transition zone between the matrix and the particles, and its properties are evaluated in this work by means of MD simulations at the very interface between both phases. Figure 5.1a shows a virtual SiSiC microstructure generated using the presented method. Figure 5.1b presents a slice of this microstructure and three independent phases can be clearly identified, namely, SiC, a-Si, and ITZ.

The length of the elements, which is required for the stiffness matrix assembly, is directly obtained from the Delaunay's triangulation. The areas of the lattice elements are chosen so as to meet homogeneous material properties in a preliminary test. Both circular and rectangular cross-sections have been proposed in the literature[213].

c) Micromechanical elastic behaviour. The mechanical properties of the constituents of SiSiC are taken in this work from the MD simulations, and the five different potentials have been considered herein. Regarding the ITZ, it can also be obtained by means of MD simulations, although a simpler assumption can be used to estimate its elastic modulus[220]:

$$\frac{\mathbf{2}}{\boldsymbol{E_{ITZ}}} = \frac{\mathbf{1}}{\boldsymbol{E_{a-Si}}} + \frac{\mathbf{1}}{\boldsymbol{E_{SiC}}} \qquad (5.9)$$

Where $\boldsymbol{E_{ITZ}}$, $\boldsymbol{E_{a-Si}}$, and $\boldsymbol{E_{SiC}}$ are the corresponding elastic moduli for each phase.

In order to evaluate the elastic behaviour of the material at different temperatures, virtual uniaxial tensile tests are performed. Then, the global elastic modulus is obtained measuring the average vertical strain (i.e., the imposed displacement over the height

of the specimen) and the average stress (obtained as the reaction forces over the cross-sectional area).

d) Microscale Properties: evaluation of the Coefficient of Thermal Expansion. The same RVEs generated to evaluate the elastic modulus were used to obtain the global coefficient of thermal expansion of the heterogeneous microstructure. Free expansion tests were modelled as follows: normal displacements on the nodes of one face are constrained and free on the opposite face of the cube, keeping one vertex of the cube clamped to prevent rigid-body motion. An initial internal stress, σ_{th}, was set for each element, which depends on the phase of the element and the temperature increment:

$$\sigma_{th} = \alpha \cdot \Delta T \cdot E$$

where α is the CTE, ΔT the change in temperature and E the elastic modulus of the element. Finally, the CTE in each direction is obtained as the average strain in that direction over the temperature change:

$$CTE = \frac{\Delta L}{L} \cdot \frac{1}{\Delta T} \qquad (5.10)$$

5.2.3. Multiscale strategy

The multiscale strategy followed in this work is based on a parameter-passing scheme[217]. Under this approach, the information is passed from a lower scale of observation into a higher scale in terms of material properties. Thus, two scale transitions are covered in this study

i) Atomistic to microscale: the thermal and mechanical properties obtained by means of MD simulations for each constituent (a-Si, alpha-SiC, beta-SiC, a-Si-SiC interface) are used in lattice model simulations as local properties.

ii) Microscale to macroscale: the thermal and mechanical properties obtained by means of lattice model simulations are wrapped up into constitutive material models used in finite element simulations at the macroscale (e.g., pipes, elbows, joints, etc). For this purpose, numerical homogenization schemes (i.e., volume averaging) is used:

$$\langle C \rangle = \frac{1}{\Omega_{RVE}} \int_{\Omega_{RVE}} C d\Omega \qquad (5.11)$$

where C is the local variable, Ω_{RVE} is the volume of the RVE and $\langle C \rangle$ the averaged, global variable.

The receivers are analysed at the macroscale by means of the finite element method (FEM), using averaged material properties from lower scale simulations, i.e., explicitly from lattice model simulations and, implicitly in these, from MD simulations. These material properties are input at the constitutive material law in the FEM simulations, as discussed in Section 5.3.

5.3. Results and discussion

In order to get a high level of confidence about the predicted properties of the new materials, we first validated the force fields with experimental and *ab initio* data. We compared the behaviour of the five potentials against some mechanical and structural properties, which allows us to choose the force field that better describes the materials and employ it to predict the properties of the new composite materials. This information is then fed into the micromechanical model in order to determine the properties of the material at the macroscopic level, which are later used in the macroscopic simulations of the tubes for its performance assessment.

5.3.1. Validation of force fields for a-Si and SiC

We have selected five different potentials (two MEAM and three Tersoff potentials), with which to compare the experimental data of elastic constants, Young´s modulus, Poisson coefficient, anisotropy factor, and Bulk modulus of the cubic and hexagonal phases of SiC, as well as amorphous Si. The results are shown in Tables 5.1 to 5.4.

In Table 5.4 we report the percentage error of each potential, averaged for the three materials studied. We observe that the potential that predicts values closer to the experimental ones is Tersoff (c), with average percentage errors below 11% for all the calculated properties. Thermal properties are usually more difficult to predict than structural properties. In Table 5.1, 5.2 and 5.3 we show the calculated and experimental values of the coefficients of thermal expansion of the three materials, for the five potentials, as a function of temperature.

Table 5.1. Elastic constants (C_{11}, C_{12} and C_{44}), Young´s modulus (E), Poisson coefficient (v), anisotropy factor (A), and Bulk modulus (B) calculated in this work with different potentials, in comparison with experimental data, for 3C-SiC (cubic, beta phase). (a).

Property	MEAM **a**[71]	MEAM **b**[34]	Tersoff **c**[37]	Tersoff **d**[35]	Tersoff **e**[36]	Exp. Data [229]
C_{11} (GPa)	396	402	383	383	446	**390**
C_{12} (GPa)	147	115	144	144	138	**142**
C_{44} (GPa)	183	187	245	245	206	**256**
K (GPa)	230	211	224	224	241	**225**
G (GPa)	158	165	175	175	181	**183**
$E_{(111)}$ (GPa)	316	351	304	304	381	**314**
v	0.22	0.19	0.19	0.19	0.2	**0.18**
A	0.29	0.22	0.66	0.66	0.23	**0.68**

Table 5.2. Elastic constants (C_{11},C_{12} and C_{44}), Young´s modulus (E), Poisson coefficient (v), anisotropy factor (A), and Bulk modulus (B) calculated with different potentials in comparison with experimental data, for 6H-SiC (hexagonal, alpha phase).

Property	MEAM **a**[71]	MEAM **b**[34]	Tersoff **c**[37]	Tersoff **d**[35]	Tersoff **e**[36]	Exp. Data [230]
C_{11} (GPa)	427	457	485	506	505	**502**
C_{12} (GPa)	166	102	120	131	121	**100**
C_{44} (GPa)	91	167	159	176	176	**167**
K (GPa)	253	220	242	256	249	**234**
G (GPa)	104	172	167	184	187	**183**
$E_{(111)}$ (GPa)	334	420	437	452	458	**469**
v	0.32	0.19	0.22	0.21	0.2	**0.19**
A	-0.19	-0.05	-0.10	-0.05	-0.06	**-0.14**

Table 5.3. Elastic constants (C_{11},C_{12} and C_{44}), Young´s modulus (E), Poisson coefficient (v), anisotropy factor (A), and Bulk modulus (B) calculated with different potentials for amorphous silicon (a-Si). We have also included two sets of experimental values.

Property	MEAM **a**[71]	MEAM **b**[34]	Tersoff **c**[37]	Tersoff **d**[35]	Tersoff **e**[36]	EXP. Data [231,232]
C_{11} (GPa)	193	144	140	147	141	**156, 138**
C_{12} (GPa)	45	56	60	63	63	**58, 42**
C_{44} (GPa)	74	43	41	39	38	**49, 48**
K (GPa)	94	85	87	91	89	**91, 74**
G (GPa)	73	44	40	40	39	**49, 48**
$E_{(111)}$ (GPa)	176	113	104	109	102	**125, 118**
v	0.19	0.28	0.3	0.31	0.31	**0.27, 0.23**
A	0.00	-0.01	0.01	-0.04	-0.01	**0, 0**

The potential that best models the CTE is MEAM (a) for the cubic phase and Tersoff (c) for the hexagonal phase.With the exception made for MEAM (a), the rest of the potentials overestimate the CTE. It should be remarked that the MEAM (a) predicts very accurately the coefficient of thermal expansion of the cubic phase, but gives a very bad description of the hexagonal phase, while Tersoff (c) gives a better description of the materials overall.

Table 5.4. Average percentage error of the properties calculated with different potentials in the three systems studied: 3C-SiC, 6H-SiC and a-Si.

Property	MEAM a[71]	MEAM b[34]	Tersoff c[37]	Tersoff d[35]	Tersoff e[36]
C_{11} (GPa)	13,4	6,6	5,1	2,8	8,2
C_{12} (GPa)	30,6	8,2	8,3	13,7	10,8
C_{44} (GPa)	40,7	13,7	9,0	10,6	16,3
K (GPa)	4,5	6,3	2,8	3,3	5,2
G (GPa)	34,7	9,0	10,8	8,1	8,2
$E_{(111)}$ (GPa)	23,4	10,6	8,9	6,5	14,0
v	40,0	3,3	10,9	10,5	10,6
A	7,2	1,1	-8,5	-20,4	3,0

The disagreement between calculated and experimental data is more prominent in the case of the Specific Heat, cp, as shown in the following figure.

For c_p, all the potentials have a similar behavior, but the experimental cp for the two SiC structures, for temperatures between 100 K and 700 K, are much lower than the values predicted by the potentials. There are no experimental data available for amorphous silicon, but we have also plotted its specific heat, and we observe that the five potentials give a similar description, with MEAM (a) and Tersoff (e) predicting a stabilization at high temperatures, while the rest of the potentials still show increases as temperature increases. As an indirect validation of the potentials, we can mention that the values predicted for the specific heat of amorphous Si are lower than those of SiC, as would be expected due of its density, lower than that of the silicon carbide structures.

In view of this analysis, we reach the conclusion that, overall, the best potential is Tersoff (c). The first relevant property related to the mechanical stability of the materials that we will discuss is the stress-

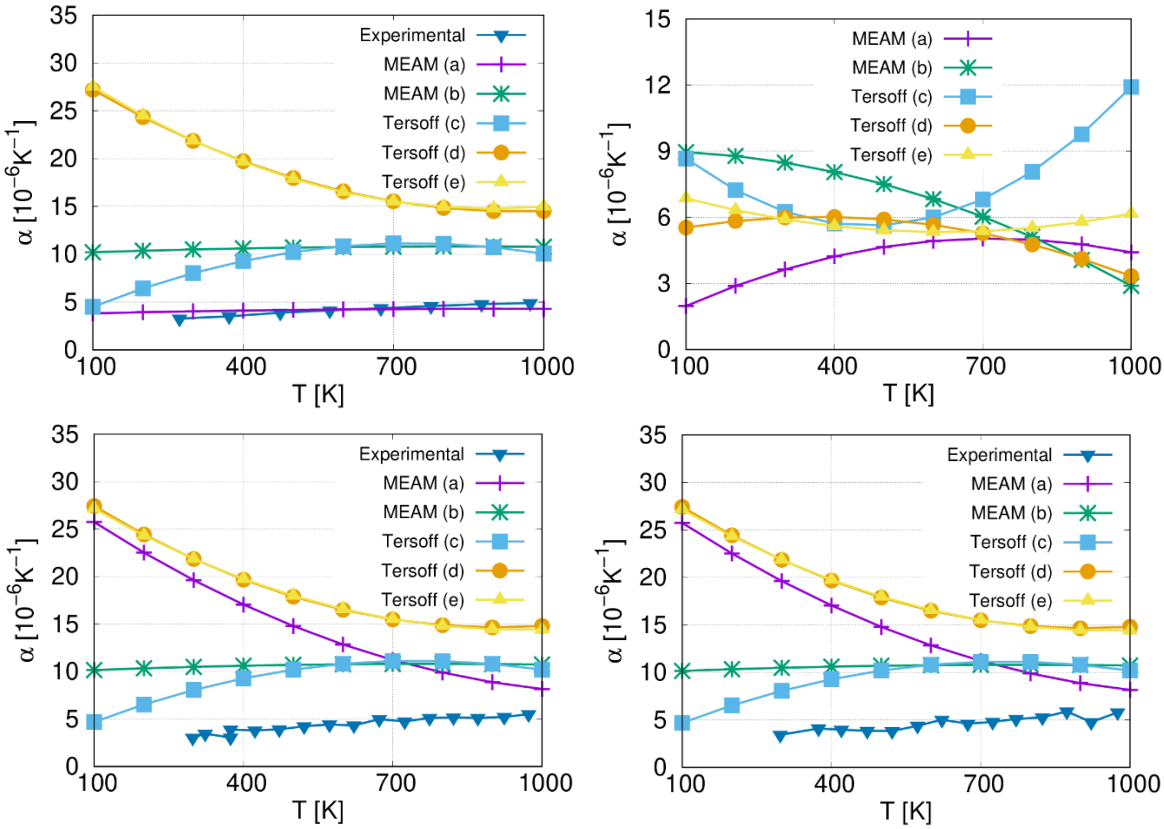

Figure 5.2. Coefficient of thermal expansion with different potentials in comparison with experimental data for 3C-SiC (top-left), a-Si (top-right), and axes X (bottom-left) and Z (bottom-right) of 6H-SiC, at different temperatures[34–37,71].

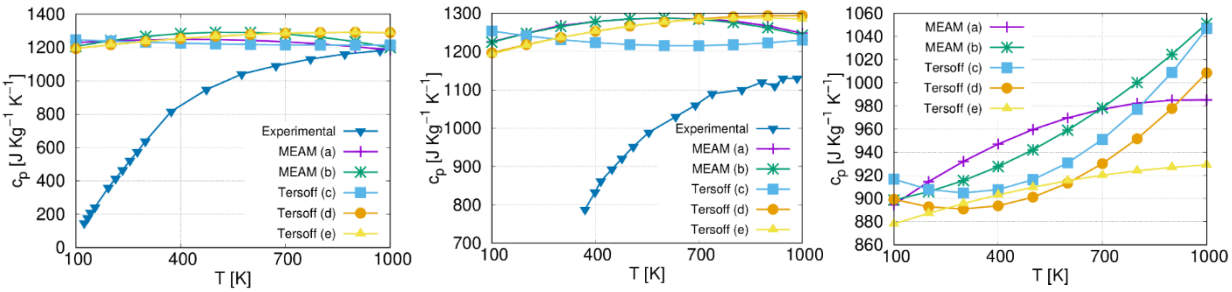

Figure 5.3. Specific heat with different potentials in comparison with experimental data for 3C-SiC (left), 6H-SiC (middle), and a-Si (right) at different temperatures[34–37,71].

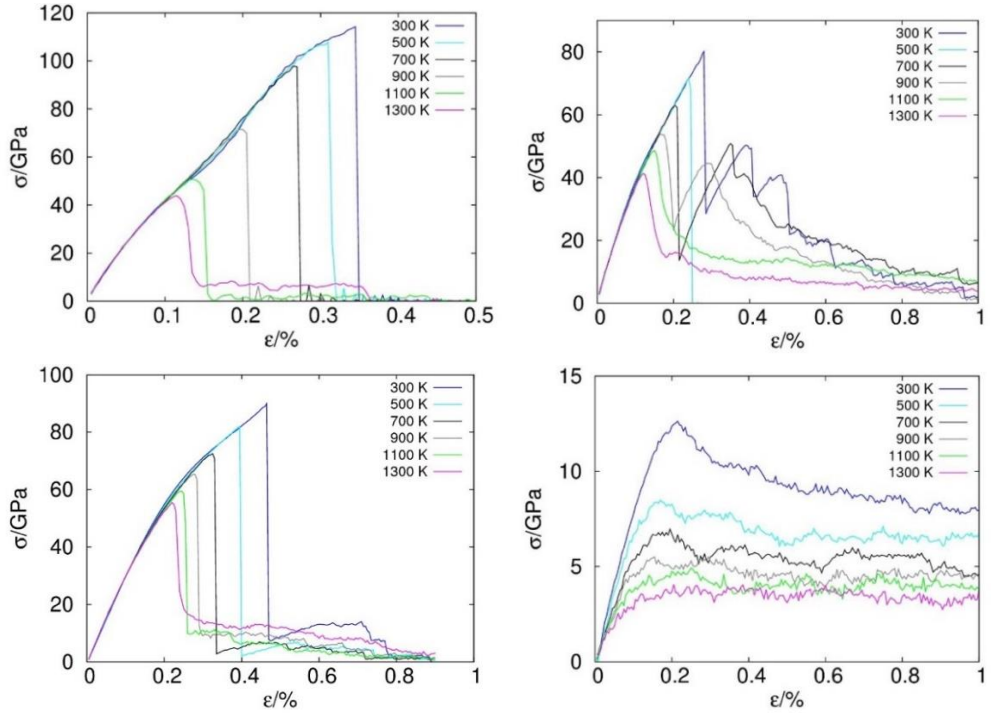

Figure 5.4. Stress-strain curves, calculated for temperatures between 300 and 1300 K of the systems: (Top-Left) 6H-SiC – Z axis, (Top-Right) 6H-SiC – X axis, (Bottom-Left) 3C-SiC, (Bottom-Right) a-Si.

strain curves. The data of stress-strain curves can be fed into the models that permit the calculation of materials at higher scales (microns) and times (milliseconds). The results obtained are shown in Figure 5.4.

In Figure 5.4 we can see that the highest strength values are for hexagonal SiC on its Z axis, which exceeds 110 GPa at 300 K. The next one is the cubic SiC, which is close to 90 GPa. Third, hexagonal SiC in its X and Y axes and finally, as expected, a-Si is the system that will break more easily, not being able to undergo stresses above 13 GPa at room temperature. The failure of the systems is abrupt in the crystalline structures. As expected, in amorphous silicon there is no clear break, although a peak in stress can be seen.

5.3.2. Building the new a-Si/c-SiC composite materials

We have designed, and studied the properties, of two types of nanocomposite materials. The first one is a simple plane, between the pair slab surface of c-SiC, and

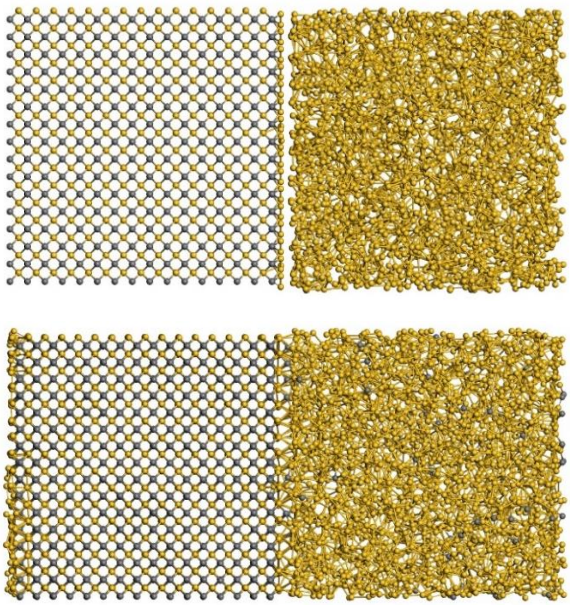

Figure 5.5. Plane interface between the plane slab surface 100 of 3C-SiC, and amorphous Si, before (left) and after (right) the molecular dynamics simulation has been performed.

amorphous Si (see Figure 5.5). This material will provide a reference set of data of the properties of c-Si/a-Si interfaces. The second system we studied is formed by a matrix of a-Si, in which SiC crystalline nanoparticles are embedded. Unlike in the first system, in this system the effect of particle sizes plays a significant role, so that thermostructural properties may be different. We calculated their properties, in order to study whether these materials could be used in thermosolar applications.

The amorphous Si material has been created in such a way as to ensure that the interaction between the two systems is as realistic as possible. The method is based on the use of MD simulations. First, a supercell of crystalline silicon (of 45 Å and 4096 atoms) is heated up (to 3500 K), until a liquid state is reached, and then it is

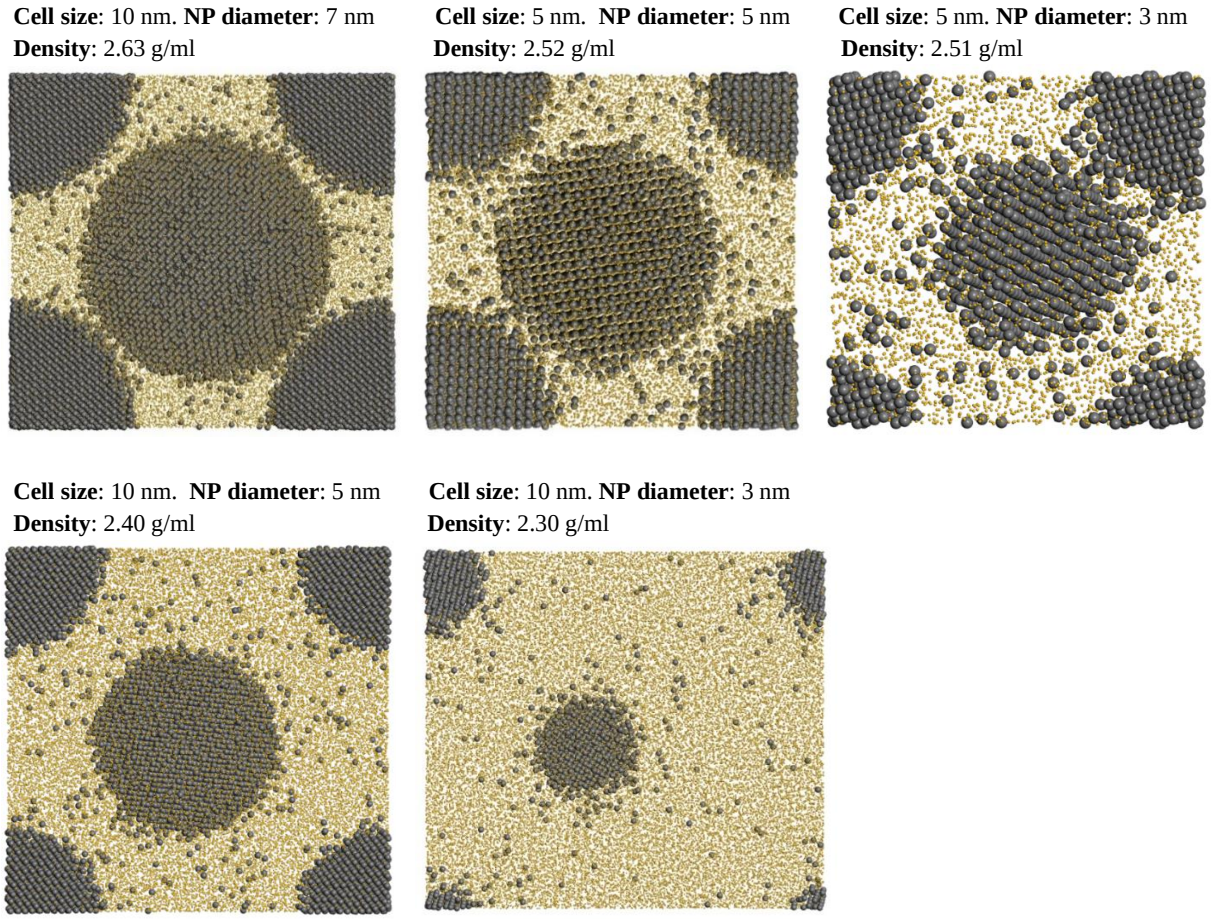

Figure 5.6. Orthographic view of different systems of well-ordered SiC NPs in a BCC symmetry inside an a-Si matrix.

quenched to 500 K, with a cooling rate of 0.5 K/ps. MD calculations are carried out under constant pressure at 1.01325 bars. The equations of motion are integrated using the velocity from the Verlet algorithm with a time step of 0.002 ps.

Once a supercell of a-Si has been thus generated, we proceed to generate the plain interface structure between a-Si and c-SiC. To do that, we created a 35 Å thick slab of crystalline c-SiC, cut to show the non-polar surface with Miller indices (100) on both sides. The amorphous sample is then placed in the vacuum above and below the slab, removing the atoms that are at a distance of less than 2.5 Å away from the c-SiC surface. We then performed a series of NPT MD simulations, starting at 3500 K and going down to 500 K (with a quenching rate of 0.5 K/ps), in order to let the atoms in the interface achieve more stable configurations. Once the system is equilibrated, we performed a production run of 500 ps. During the simulations, both the c-SiC and a-Si are allowed to move freely, but the highly stable c-SiC crystalline structure does not rearrange significantly, as we observe in Figure 5.5. The c-SiC crystal keeps its crystalline structure unaltered, although, interestingly, we do see that some C atoms have left the structure and penetrated into the a-Si region.

A similar procedure is followed to create the second composite material we studied, which is formed by SiC nanoparticles embedded within the a-Si matrix, as shown in Figure 5.6. We have created five systems with different densities: SiC NPs with diameter 3 nm inserted within a-Si filled supercells with sizes of 5 nm and 10 nm, SiC NPs with diameters of 5 nm inserted within a-Si filled supercells with sizes of 8 nm and 10 nm and SiC NPs with a diameter of 7 nm inserted within an a-Si filled supercell of size 10 nm.

5.3.3. Thermostructural properties of a SiC/a-Si plane interface

First, we have studied the thermostructural properties of the plane interface between the slab of cubic SiC and the slab of amorphous Si. The calculated specific heat and Coefficient of thermal expansion are shown in Figure 5.7.

We can see that the specific heat decreases with density at low temperatures, but when the temperature approaches 1000 K the curves of specific heats are similar to each other. On the other hand, the coefficient of thermal expansion has a smaller difference between 100 K and the maximum of the curves when the density is greater. The maximum for the thermal expansion is reached at higher temperatures as density increases, but nevertheless, that maximum is smaller. A further understanding of the mechanical behaviour of these materials can be obtained by analysing their stress-strain curves, shown in Figure 5.8.

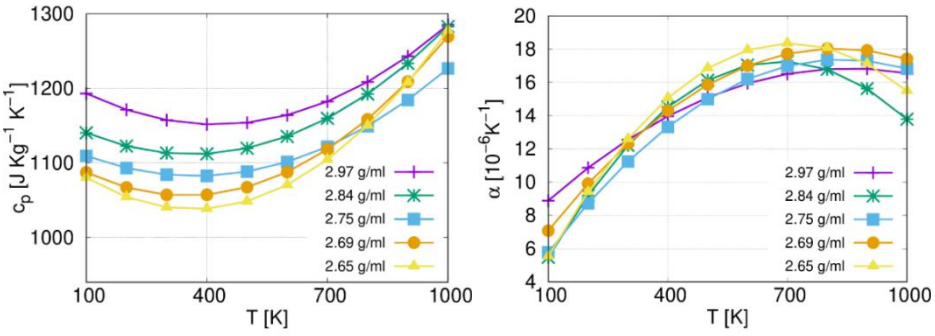

Figure 5.7. Specific heat and Coefficient of thermal expansion of five plane interfaces of 3C-SiC and a-Si with different densities at different temperatures with the Tersoff (c) potential[37].

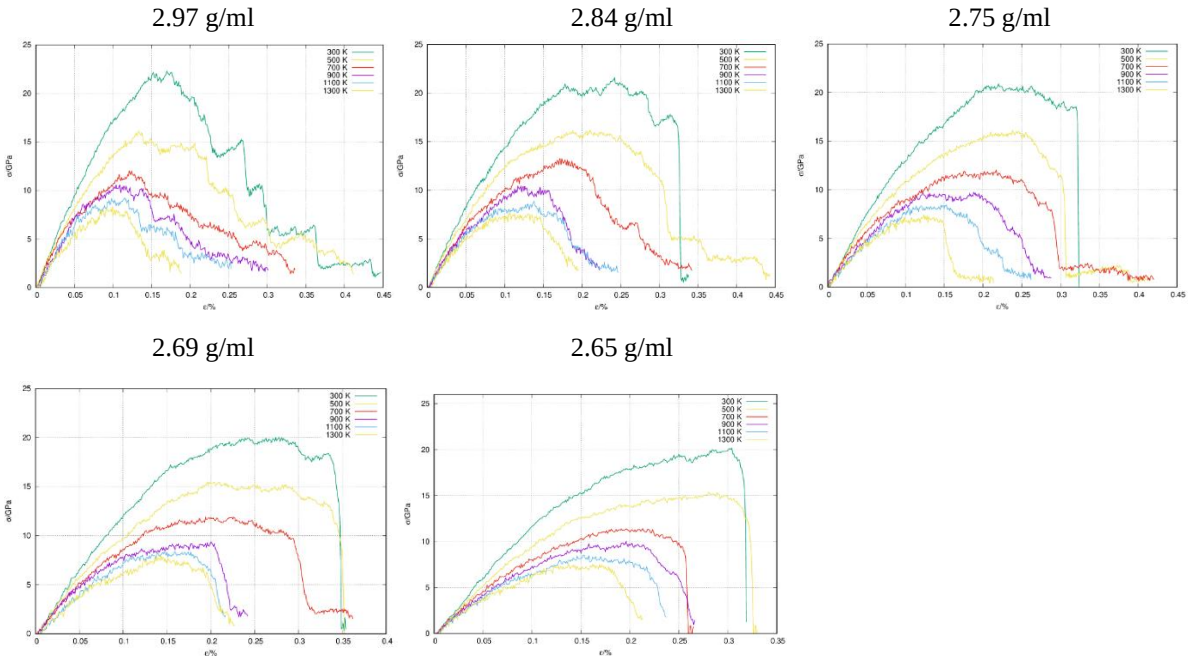

Figure 5.8. Stress-Strain curves for plane interfaces with different densities of 3C-SiC and a-Si at different temperatures with the Tersoff (c) potential[37].

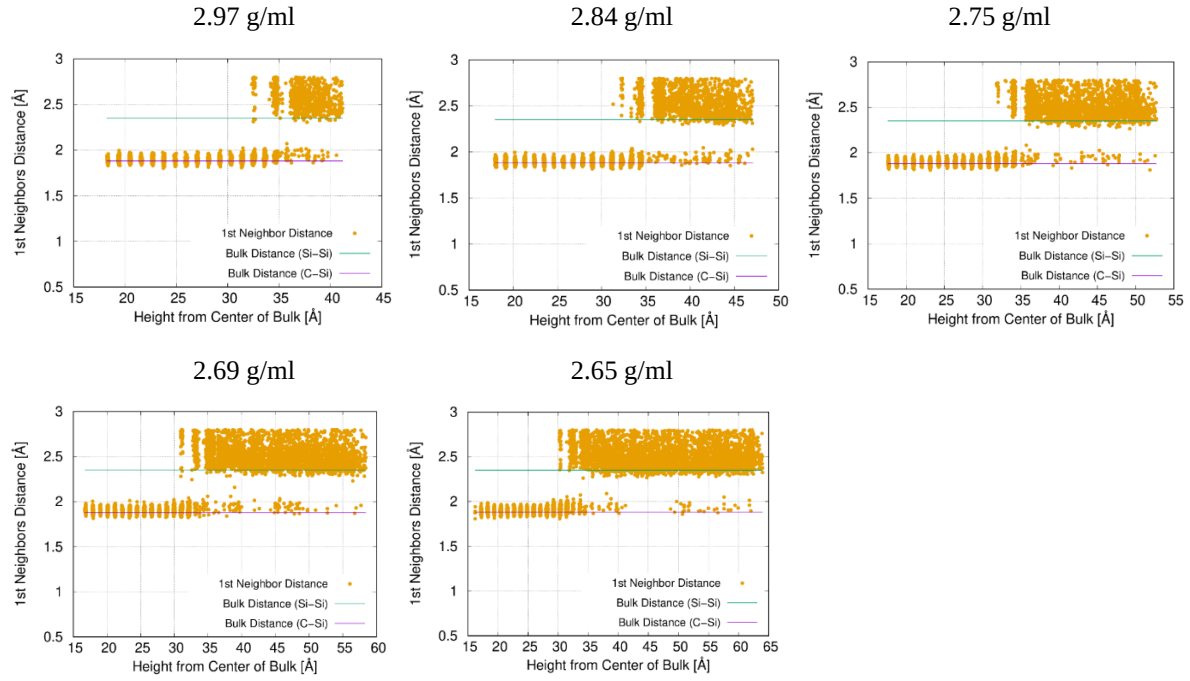

Figure 5.9. 1st neighbor distance of all atom types vs distance to the center of the c-SiC slab. The column of SiC is constant while the column of a-Si increase from top to bottom and from left to right.

We observe that all materials show similar responses, featuring the typical behaviour of brittle materials, since at low strains they show a linear region in which, as strain increases, stress also increases linearly (following Hooke's general law), with the slope being the Young's modulus. And at a certain value, the interatomic forces are not sufficient to withstand the forces exerted externally, and the material yields, starting the region of plastic deformation.

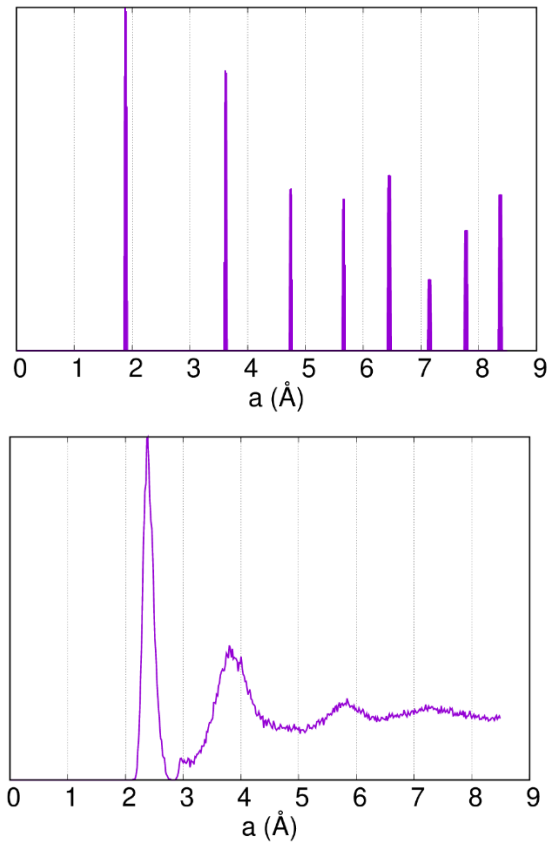

Figure 5.10. Radial Distribution Function of Si-C atoms in cubic 3C-SiC (left) and Si-Si in a-Si (right).

Our simulations show that all of these nanocomposites c-SiC/a-Si materials can withstand maximum stresses of 20 GPa (at room temperature), and can deform up to circa 0.3 %. But at higher temperatures the yield stress decreases rapidly, so that at 1300 K the yield stress is around 7 GPa.

In order to get a better insight into the atomic detail of these interfaces, we have created plots showing the distance between each atom and its first neighbour, as a function of the distance to the centre of the SiC bulk at 300 K. The results are shown in Figure 5.9, where we have included two horizontal lines, corresponding to the distances between Si-C atoms in the bulk phase of c-SiC and between Si atoms in a-Si 2.35 Å.

The plots in Figure 5.9 show a clustering around the two horizontal lines mentioned, at values 1.88 Å and 2.35 Å. As expected, in the region where SiC is placed we only see first neighbour distances around the distance in which we find the first Si-C neighbour. In the region where the amorphous silicon is placed, we observe a much broader distribution, although close to the first neighbour distances found in a-Si. There are two interesting facts, though. The first one is that in the a-Si region there are some atoms with distances close to 2 Å, corresponding to C atoms that have diffused into the a-Si region (as can be seen in Figure 5.5 and in the RDF shown in Figure 5.10). The second one is that there is no abrupt transition between the c-SiC and a-Si materials, there is rather a transitional region of less than 10 Å, in which we observe features of both materials. This is the contact region that binds the two materials together.

5.3.4. Thermostructural properties of SiC NPs in an a-Si matrix

We have also studied the thermostructural properties of the 5 systems we have created inserting SiC NPs within an a-Si matrix. The calculated specific heats and coefficients of thermal expansion of these systems are shown in figure 5.11.

We observe that, as in the case of the plane interface, the specific heat increases as the density increases, but in these new systems, there is almost no variation of the specific heat as temperature changes, i.e. for each density the specific heat is nearly constant in the range of temperatures between 100 and 1000 K. We also observe that the nanoparticulate systems have specific heats that are around 15% lower than the plane interface.

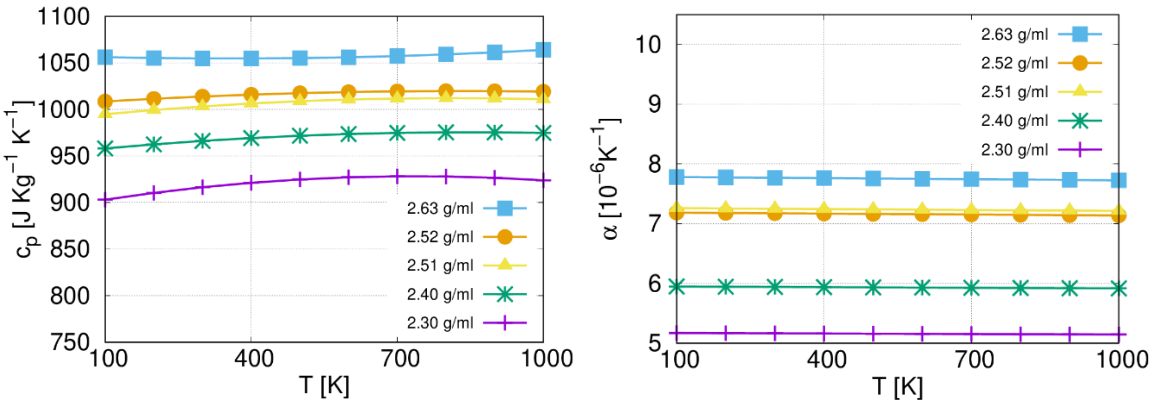

Figure 5.11. Specific heats and coefficients of thermal expansion of the systems with 3C-SiC NPs in an a-Si matrix with different densities at different temperatures with the Tersoff (c) potential[37].

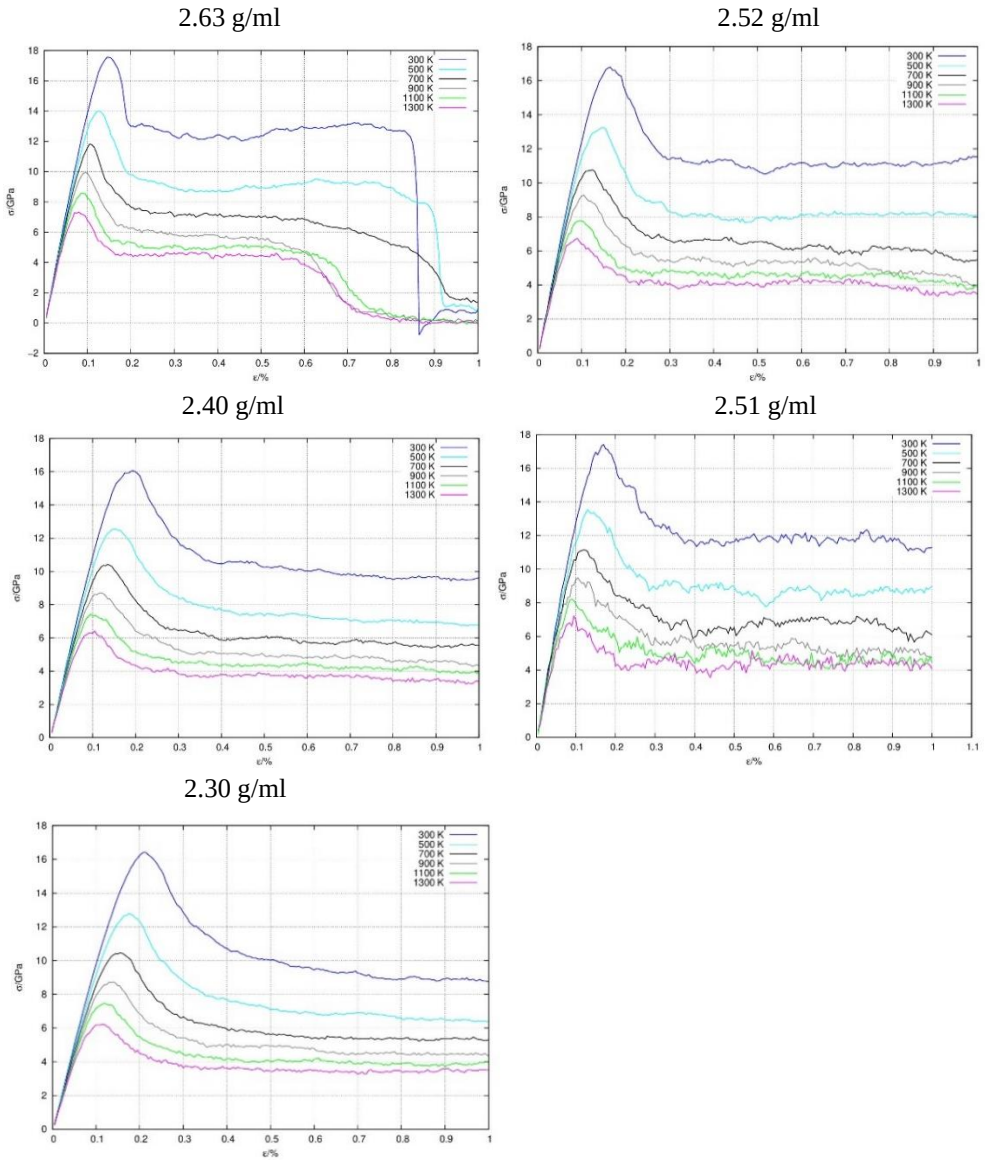

Figure 5.12. Strain-stress curve calculated at different temperatures (from 300 to 1300 K) for 3C-SiC NPs in a matrix of a-Si.

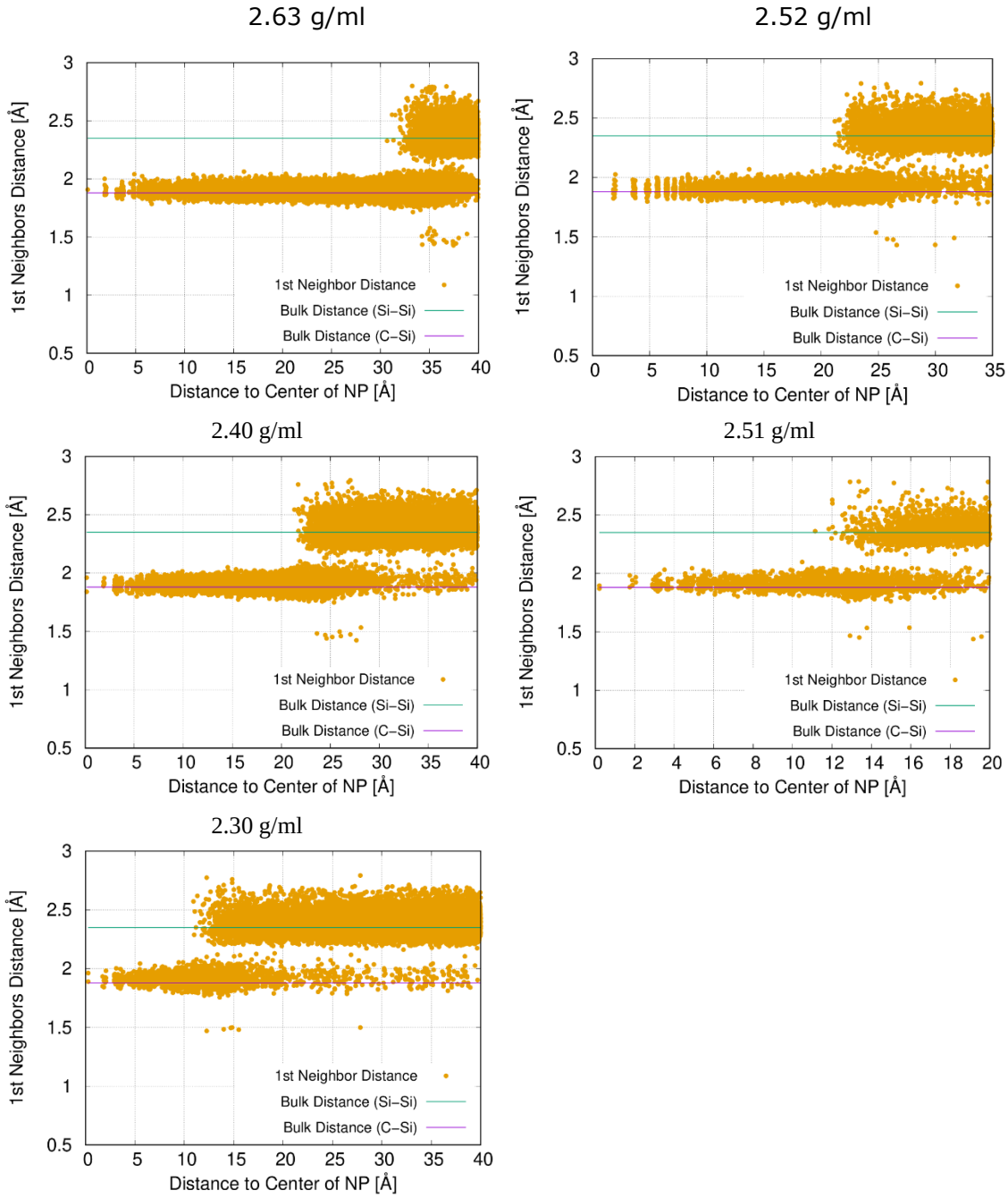

Figure 5.13. First neighbor distance of all atom types vs distance to the center of NP.

Regarding the CTEs, the behaviour of these nanocomposites is also very different to that of the plane interface. In the latter system, there were no significant differences between the curves for the different densities, and there was a strong influence of the temperature, while in the nanoparticulate systems the CTE increases with the density of the system, and there is no dependence with temperature. A positive implication of this fact is that an increase in temperature would have little effect on thermal stresses.

We have also calculated the strain-stress curves of the nanoparticulate systems, which are shown in the following figure.

In these strain-stress curves we can appreciate that the ruptures are not as abrupt as in the plan interface. This is not

surprising, since there is a matrix of amorphous Si that extends throughout all the material, filling all the space connecting the NPs. We observe that the strain supported by these systems is slightly higher than that supported by the amorphous silicon. All systems, regardless of the size of the cell and the nanoparticles, support a strain of between 16 and 18 GPa and a deformation of about 0.2%.

In Figure 5.13 we show the plots of the distances between first neighbors in these systems. In this case the X axis is the distance to the center of the NP

We observe that there is a much higher degree of structural disorder than in the composite materials with plane interfaces, as evidenced by the lack of distances to the center of the NP for which there are no atoms. Only in the system with a density of 2.52 g/ml we see such strips, but in a small core of the NP. We also see that there is a large number of C atoms that have penetrated the a-Si matrix.

5.3.5. Thermoelastic behaviour of SiSiC microstructures

In this section we present the mechanical properties obtained by means of lattice model simulations at the microscale.

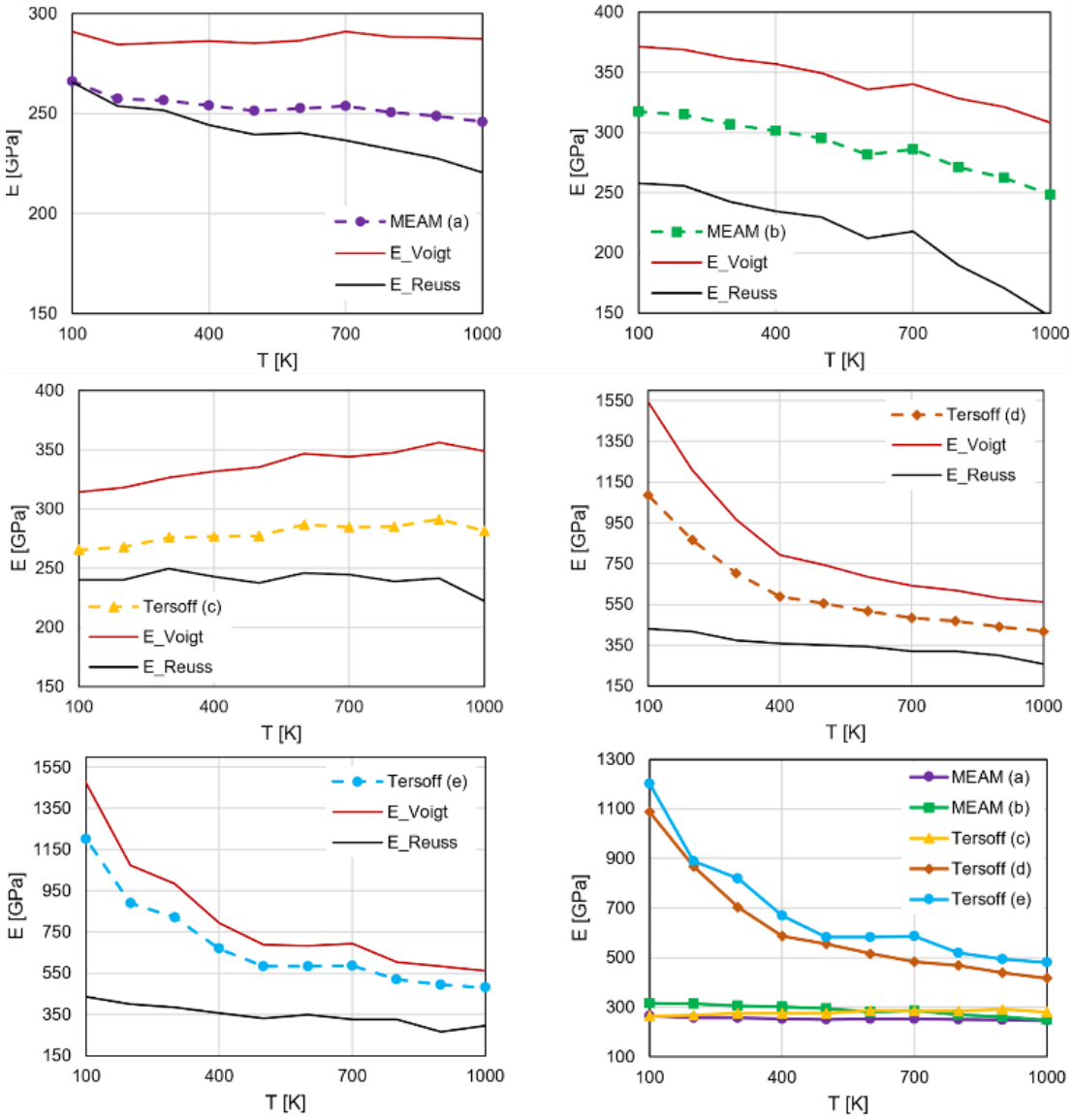

Figure 5.14. Effective Elastic modulus of SiSiC at different temperatures, using different interatomic potentials and comparison with respect to Voigt-Reuss bounds.

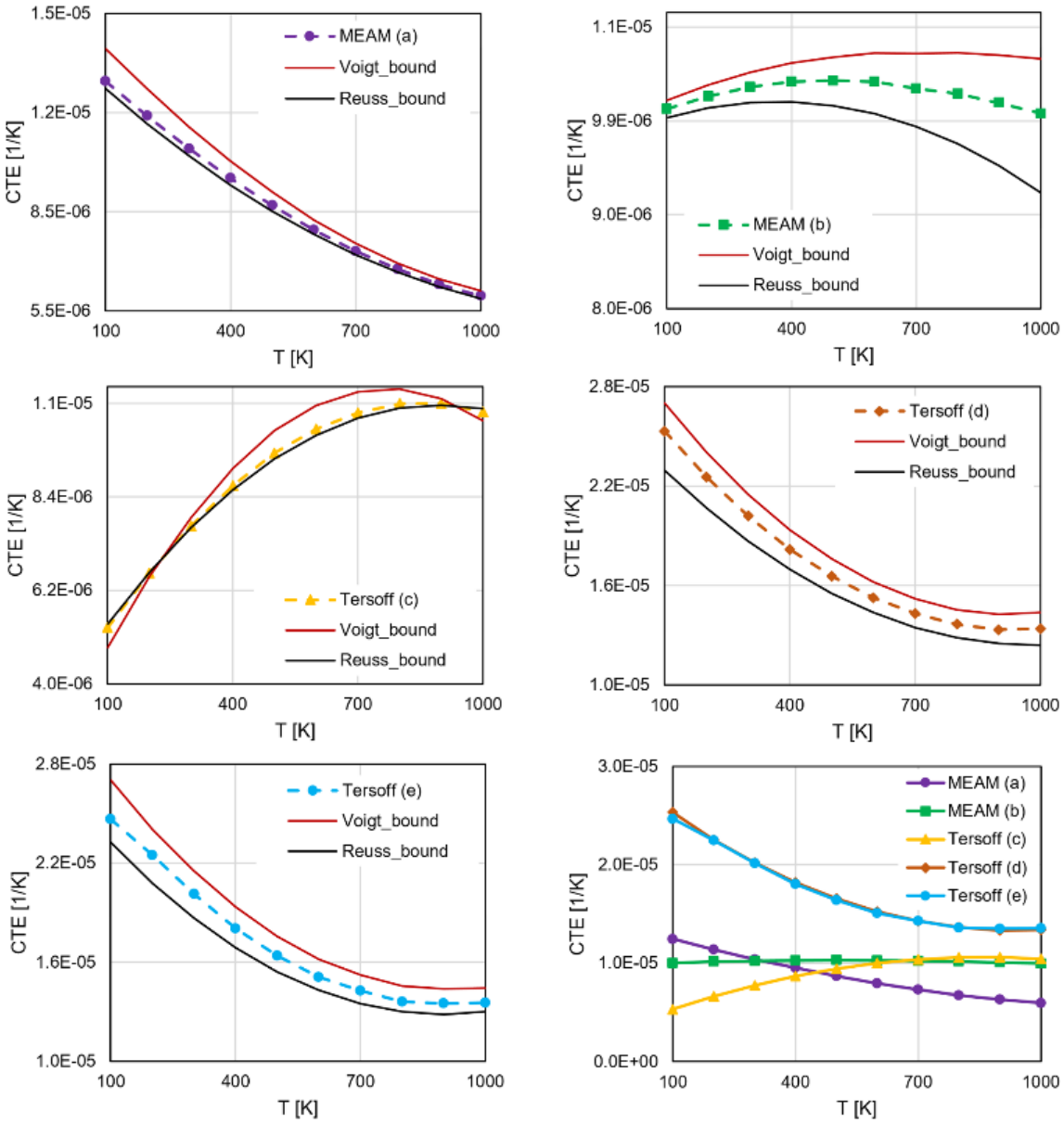

Figure 5.15. Effective Coefficient of Thermal Expansion of SiSiC at different temperatures, using different interatomic potentials and comparison with respect to Voigt-Reuss bounds.

At this level of theory, the mechanical properties obtained using MD simulations for each constituent are applied into the lattice model simulations as local properties. The effective material properties of SiSiC depends on aspects such as the size and geometry of the grains, the amount of free Si, temperature, or presence of pores, among other parameters[233]. Therefore, a numerical tool able to account for these many features is of great importance in material characterization.

In Figure 5.14 we show the results obtained for the elastic modulus, as function of the temperature, for each interatomic potential. The temperatures considered are in the range from 100 to 1000 K, in increments of 100 K, which is exactly the same range as in MD simulations. Due to the lack of experimental information, the results are compared to Voigt-Reuss bounds, which are identified as upper and lower bounds on the effective elastic properties. These bounds are defined as:

$$E_{eff}^{Voigt} = \phi_{a-Si}E_{a-Si} + \phi_{SiC}E_{SiC}$$

$$E_{eff}^{Reuss} = (\phi_{a-Si}/E_{a-Si} + \phi_{SiC}/E_{SiC})^{-1}$$

Where ϕ_{Si} and ϕ_{SiC} are the volume fraction of *Si-matrix* and *SiC-particles*, respectively. E_{a-Si} and E_{SiC} are the elastic moduli obtained by means of MD simulations at different temperatures, using the potentials analysed herein.

The microstructural lattice simulations suggest that the elastic moduli, in all cases except for the Tersoff (c) potential, decrease with temperature, as reported in the literature[234]. Moreover, the resulting effective elastic modulus of the SiSiC microstructure for both MEAM potentials yield values within the range of 200 – 375 GPa reported by Evans et al.[235], or even beyond 400 GPa[236]. In the case of the Tersoff (c) potential, the values are within this range, but the elastic modulus increases with temperature, similarly to what happens with that value of the 3C-SiC and 6H-SiC at MD simulations. The trend of Tersoff (d) and Tersoff (e) results are in agreement with the experimental observations, although the values are much higher between 100 – 400 K.

Another relevant property that describes the thermoelastic behaviour of solids is the CTE, which plays an important role in the design of materials subject to high temperature. The thermal expansion induces stresses if the expansion is restrained, which threatens the integrity and durability of structures. In Figure 5.15 we show the results obtained for the CTE for different potentials, in a range of temperatures from 100 to 1000 K, in increments of 100 K. The results are compared to the Voigt-Reuss bounds, which are identified as upper and lower bounds of the effective CTE of SiSiC. As presented by Milhans et al.[237], these bounds are defined as:

From the results discussed, it can be observed that the CTE is strongly temperature-dependent, except in the case of MEAM (b). Such influence in the simulations is largely due to the large values of the CTE predicted for the SiSiC phases by MD simulations. The numerical predictions are larger than the experimental value[238], which is assumed to be low temperature-dependent and close to $4.5{\cdot}10^{-6}$ 1/K. Only one of the Tersoff (c) potential exhibits a positive tendency as the temperature increases, which is in accordance with other studies in the literature[239]. With regard to the design process, these larger predictions of the CTE will lead to a conservative analysis of the thermal stresses, since lower expansion should take place actually.

5.3.6. Thermomechanical assessment of SiSiC tubes for central receivers

In this section we will complete the upscaling approach as described in section 2.3, covering three length scales, i.e., atomic, micro, and macroscale, showing the implementation of this methodology for the design of tubes in central receivers.

Central receiver systems (CRS) are a class of concentrating solar power plant configurations in which the solar heat radiation reflected by heliostats (i.e., mirrors), which are arranged on the so-called *solar field*, is projected onto a cavity atop a central tower (in the case of single-tower plants) that hosts the receiver[113]. This receiver can be made of several panels

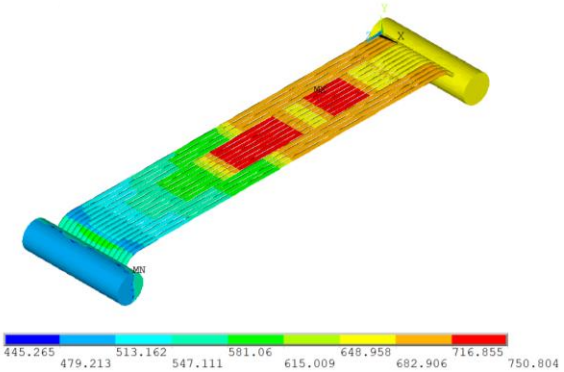

Figure 5.16. Temperature distribution (°C) of a central receiver panel.

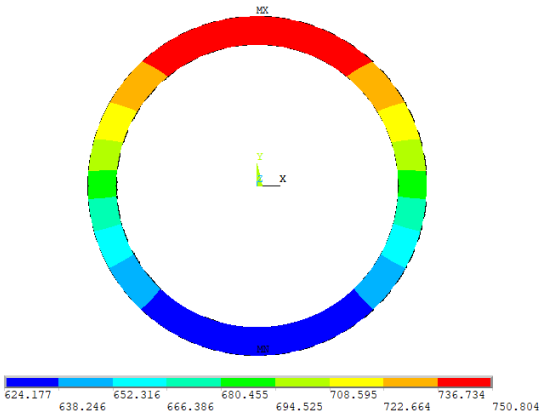

Figure 5.17. Temperature distribution (°C) across an inner tube in the panel.

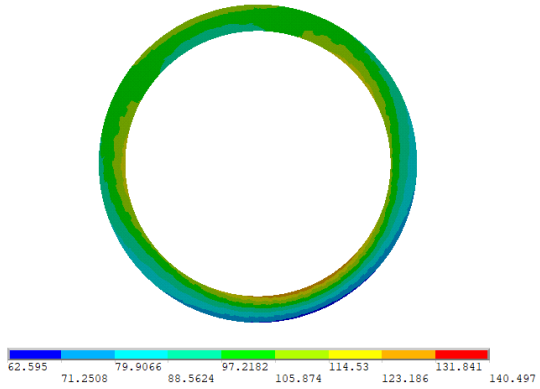

Figure 5.18. Maximum principal stresses (MPa) across a section of the tube for a specific temperature gradient and working pressure.

with tubes aligned so as to absorb the heat radiation, which is then transferred to the heat transfer fluid (HTF).

One of the main objectives in the design of CRS is to increase the efficiency of the plant. This can be achieved by increasing the operating temperature, as is the case of the s-CO_2 Brayton cycle[197]. Of course, there exists a counterpart with respect to the durability of the materials, especially those of the receiver, which will experience the highest temperatures. In Figure 5.16 the temperature distribution in one panel, obtained by means of FEM simulations using Ansys®, is presented. It can be observed that temperatures up to 1000 K can be achieved on the exposed surfaces. However, this distribution is not constant across the section of the tube, and important temperature gradients can be expected in these sections[198,240], as shown in Figure 5.17. In these FEM simulations, different heat transfer mechanisms (i.e., radiation fluxes, convective losses and conductivity) have been considered.

The temperature distribution obtained by means of FEM simulations are sequentially coupled with mechanical FEM simulations that also take into account the working pressure, and the material properties are defined as tabulated temperature-dependent data. Namely, the elastic modulus and thermal expansion coefficients obtained in Section 3.4 and 3.5 are used here to compare the thermomechanical performance of the new nanocomposite with respect to SiSiC tubes. This information is sufficient to obtain the stress state of a piece of the tube, as presented in Figure 5.18. Due to the brittle nature of the material, we will

analyse the maximum principal stresses to check whether the tube withstands such temperature and pressure conditions.

In order to complete the design analysis, we consider different thickness-to-diameter (t/D) ratios, namely from 0.05 to 0.3. This value affects both the temperature distribution and stresses in the tube. Moreover, two temperature-dependent material laws are input in the simulations of SiC (i.e., 2.30 g/ml and 2.65 g/ml) and another five corresponding to the different force fields used in the case of SiSiC. This results in a screening of 42 different design cases, which are summarized in Figure 5.19.

As pointed out above, one of the main design criteria is the maximum principal stress. According to the literature[233,241], the strength of reaction-bonded SiC at the macroscale is within the range of 235 – 310 MPa, at room temperature. Moreover, this value may increase with temperature as a result of

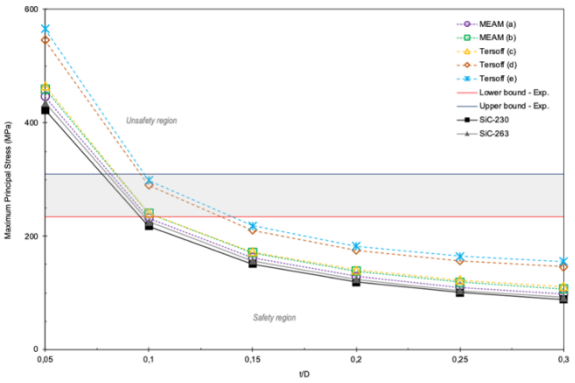

Figure 5.19. Maximum principal stresses in the tube for different designs (t/D ratios) and material properties against experimental bounds[233,241].

oxidation processes that take place at high temperature[233]. Again, these values depend on the microstructural properties.

Finally, we can state from the simulations that SiC230 and SiC263 exhibit lower stresses at these operating conditions, satisfying the safety conditions for t/D > 0.10. Besides, the SiSiC tubes here designed, with t/D > 0.15, are safe under these extreme conditions (normal operating conditions tend to be smoother). It must be remarked that the highest values of the maximum principal stresses are quite localized, and the average value is expected to be 25% lower. When comparing the stresses of SiC230 and SiC263 with respect to Erhart potential (Tersoff c), which is the same force field used in the former simulations, the principal stresses in the newly designed material is ca. 20% lower. In light of these results, and taking into account the excellent thermal stability of this type of material, we can conclude that the new material is a suitable option in solar energy harvesting, offering an excellent thermomechanical behavior, within the safety region with less amount of material when compared to ordinary SiSiC.

5.4. Conclusions

We have designed a new type of SiC-based material with potential applications in thermosolar receivers. These materials are formed by a matrix of amorphous silicon, in which SiC nanoparticles are inserted and show better thermomechanical performance than other SiSiC materials. We have then used Molecular Dynamics simulations to study the thermostructural properties of the designed materials, for 5 different composites, of varying density, percentage of the two forming materials, etc. We have compared the thermostructural properties of these materials with those of a material formed by layers of SiC and a-Si, and we have found that the nanoparticulate systems are less brittle than the materials with SiC crystals, since the presence of a-Si forming an extended matrix provides the system with a behavior more similar to non-crystalline materials.

Since the goal of this work is to design new materials that could be used in thermosolar applications, we have developed a multiscale methodology to investigate the performance of the materials at three scales of observation. First, at the atomic scale, we use MD simulations to gather information about essential material properties of single phases and design new nanocomposites. Then, at the mesoscale, we have introduced the use of the so-called lattice model to study the influence of grain sizes, polycrystal composition, among other important microstructural features. Finally, at the macroscale, we can study the performance of these materials when used within an engineering environment, as is the case of the tubes of a thermosolar receiver. As shown in this work, the lack of experimental information can be overcome by the use of atomistic simulations. However, the feasibility of these newly developed nanomaterials can be only assessed throughout several scales of observation, since carrying out this screening by means of MD simulations only is impracticable. Therefore, its combination to upper-scale techniques, such as finite

element methods, in a seamless multiscale fashion, is called to play a fundamental role in the validation of new solutions at relevant environments, reinforcing *in silico* design as a route to explore new material designs.

Conclusions

The first block of conclusions of this thesis focuses on the design and improvement of the force fields needed to study nanostructured materials with renewable energy applications. As all the materials used have an FCC symmetry, we will start with a study of the existing force fields for this symmetry, to then optimize the one that best behaves. The studies and designs are found in chapters 2 and 3 of this document.

1.- It is possible to fit the parameters of a force field to reproduce experimental observables as exactly as desired. This can be seen in Chapter 2, where we use an automated iterative fitting algorithm. We asign a fitness value to fit the parameters in the desired direction until we obtain an error as small as we need in structural properties. The risk involved in making this type of fittings is that we force the mathematical models in the direction of the chosen observables, which may worsen the reproduction of observables that are not taken into account.

2.- The method used in Chapter 3 is qualitatively different from the previous one. The difference is that we use as an observable the electron density of a cell, calculated with quantum methods. The calculation of the electron density has been carried out for Nickel, Chromium, Molybdenum and Iron. Thus, we fit the analogous parameters in our classic model. In this way, we are removing the numerical dependence between the potential parameters. This type of method does not force the mathematical model in the direction of the experimental observables. Therefore, we must check that we are correctly describing the structural properties of the material after fitting. On the one hand, we have a model that is independent of the experiments, but on the other hand, we cannot get as close to the experimental results as we want.

3.- Analytical and numerical homogenisation approaches for the Inconel 625 give practically identical curves. The difference in MD for elastic constants is only 2.5% compared to polycrystal homogenization. The potential that we develop starting from quantum calculations is consistent and brings results very close to those at higher scales.

The simulations show aging in which Chromium, Iron and Molybdenum atoms form small clusters. This observation is due to the fact that its most stable symmetry is the BCC versus the FCC of Nickel.

4.- We have carried out a study on five force fields that describe elastic and structural properties of 3C-SiC, 6H-SiC and a-Si. We determined that the one that describes them more precisely is the one developed by Erhart-Albe.

The second block of conclusions refers to the different designs and applications of materials studied with desirable properties in renewable energy applications. Materials range from nanoparticles and combinations of these with other materials to porous metallic materials designed from COFs, MOFs and zeolites.

5.- Nickel-Chromium nanoparticles behave similarly to bulk in simulations performed if they have a diameter of 5 nanometers or more. We also observe that the cell parameters decrease as the diameter of the nanoparticle decreases.

6.- Two Nickel-Chromium nanoparticles of 5 nanometers in contact keep their structures like two separate nanoparticles in the sintering process. Therefore, they

could be used in catalysis applications or solar-thermal receivers, as they are resistant to damage caused by aggressive environments and high temperatures.

7.- A new family of materials has been designed from a theoretical point of view. We have used structures such as zeolites, MOFs, COFs or their modifications as a template to build a negative replica. Some of these novel structures, composed of metals such as Platinum and Nickel, are stable at more than 1000 K in molecular dynamics of 100 nanoseconds. These materials combine the properties of porous and metallic materials, and besides, their pores are ordered just like their original templates. We have called them Ordered Nanoporous Metals. All this makes of these materials a discovery with possible applications in catalysis and separation.

Not all negative replicas were stable. We have observed that we can establish a relationship between the PLD of the templates and the stability of these materials in each type of metal.

8.- We have designed a ceramic material made up of 3C-SiC nanoparticles within an amorphous silicon matrix following a BCC symmetry. From molecular dynamics simulations we established that these systems are less fragile than those in which there is only crystalline silicon carbide. This would mean an improvement in the behavior of the materials used in thermo-solar receivers by increasing the working temperature to obtain a higher energy efficiency.

Once again, molecular simulation has been shown to be a useful tool to complement experimental data when designing force fields for various materials. With the help of quantum calculations, we can even fit the parameters of a force field without the experimental data. Furthermore, thanks to molecular simulation, we have been able to design materials that have proven to be experimentally feasible.

Conclusiones

El primer bloque de conclusiones de esta tesis se centra en el diseño y mejora de los campos de fuerza necesarios para estudiar materiales nanoestructurados con aplicaciones en el campo de las energías renovables. Como todos los materiales utilizados tienen una simetría FCC, comenzaremos con un estudio de los campos de fuerza existentes para esta simetría, para luego optimizar el que mejor se comporte. Los estudios y diseños se encuentran en los capítulos 2 y 3 de este documento.

1.- Es posible ajustar los parámetros de un campo de fuerza para reproducir observables experimentales con la precisión deseada. Esto se puede ver en el Capítulo 2, donde usamos un algoritmo de ajuste iterativo automatizado. Asignamos un valor de *fitness* para ajustar los parámetros en la dirección deseada hasta que obtengamos un error tan pequeño como sea necesario en las propiedades estructurales. El riesgo que conlleva realizar este tipo de ajustes es que forzamos los modelos matemáticos en la dirección de los observables elegidos, lo que puede empeorar la reproducción de observables que no se están teniendo en cuenta.

2.- El método utilizado en el Capítulo 3 es cualitativamente diferente al anterior. La diferencia es que usamos como observable la densidad electrónica de una célula, calculada con métodos cuánticos. El cálculo de la densidad electrónica se ha realizado para níquel, cromo, molibdeno y hierro. Por lo tanto, ajustamos los parámetros análogos en nuestro modelo clásico. De esta forma, estamos eliminando la dependencia numérica entre los parámetros potenciales. Este tipo de método no fuerza al modelo matemático en la dirección de los observables experimentales. Por tanto, debemos comprobar que estamos describiendo correctamente las propiedades estructurales del material después del ajuste. Por un lado, tenemos un modelo que es independiente de los experimentos, pero por otro lado, no podemos acercarnos tanto a los resultados experimentales como queremos.

3.- Las curvas de homogeneización analítica y numérica del Inconel 625 son prácticamente idénticas. La diferencia en MD para las constantes elásticas es solo del 2.5% en comparación con la homogeneización de policristales. El potencial que desarrollamos a partir de los cálculos cuánticos es consistente y da resultados certeros en escalas superiores a la atómica.

4.- Hemos realizado un estudio sobre cinco campos de fuerza que describen propiedades elásticas y estructurales de 3C-SiC, 6H-SiC y a-Si. Determinamos que el que los describe con mayor precisión es el desarrollado por Erhart-Albe.

El segundo bloque de conclusiones habla de los diferentes diseños de materiales estudiados con propiedades interesantes para aplicaciones en el campo de las energías renovables. Los materiales van desde nanopartículas y combinaciones de estas con otros materiales hasta materiales metálicos diseñados a partir de COFs, MOFs y zeolitas.

5.- Las nanopartículas de Níquel-Cromo se comportan de manera similar al *bulk* si su diámetro es superior a 5 nanómetros. Además, observamos que los parámetros de celda disminuyen con el diámetro de la nanopartícula.

6.- Dos nanopartículas de Níquel-Cromo de 5 nanómetros en contacto mantienen sus estructuras como dos nanopartículas separadas en el proceso de sinterización.

Por tanto, podrían utilizarse en aplicaciones de catálisis o receptores solares térmicos, ya que son resistentes a los daños provocados en dichos entornos.

7.- Se ha diseñado una nueva familia de materiales desde un punto de vista teórico. Hemos utilizado estructuras como zeolitas, MOFs, COFs o sus modificaciones como plantilla para construir una réplica negativa. Algunas de estas estructuras, compuestas por metales como el Platino y el Níquel, son estables a más de 1000 K en dinámicas moleculares de 100 nanosegundos. Estos materiales combinan las propiedades de los materiales porosos y metálicos, y además, sus poros están ordenados. Los hemos llamado Metales Nanoporosos Ordenados. Todo ello hace de estos materiales un hallazgo con posibles aplicaciones en catálisis y separación.

No todas las réplicas negativas fueron estables. Hemos observado que podemos establecer una relación entre el PLD de las plantillas y la estabilidad de estos materiales en cada tipo de metal.

8.- Hemos diseñado un material cerámico compuesto por nanopartículas de 3C-SiC dentro de una matriz de silicio amorfo siguiendo una simetría BCC. A partir de simulaciones de dinámica molecular se establece que estos sistemas son menos frágiles que el carburo de silicio cristalino. Esto supondría una mejora en los receptores termosolares aumentando la temperatura de trabajo para obtener una mayor eficiencia energética.

Una vez más, la simulación molecular ha demostrado ser una herramienta útil para complementar los datos experimentales al diseñar campos de fuerza para diversos materiales. Con la ayuda de cálculos cuánticos, incluso podemos ajustar los parámetros de un campo de fuerza sin los datos experimentales. Además, gracias a la simulación molecular, hemos podido diseñar materiales que han demostrado ser viables experimentalmente.

Bibliography

[1] R.L. Johnston, in: Front. Nanosci., Elsevier, 2012, pp. 1–42.

[2] H.W. Sheng, M.J. Kramer, A. Cadien, T. Fujita, M.W. Chen, Phys. Rev. B - Condens. Matter Mater. Phys. 83 (2011) 1–20.

[3] W. Liu, A. Tkatchenko, M. Scheffler, Acc. Chem. Res. 47 (2014) 3369–3377.

[4] S. Li, Q. Wei, Y. Shi, Z. Zhu, D. Zhang, J. Mater. Sci. Technol. 31 (2015) 946–952.

[5] M. Besson, P. Gallezot, C. Pinel, Chem. Rev. 114 (2014) 1827–1870.

[6] Z. Gentry, A. Sakamoto, M. Corey, N. Thongchua, K. Patel, (2014).

[7] T. Borowski, A. Brojanowska, M. Kost, H. Garbacz, T. Wierzchoń, Vacuum 83 (2009) 1489–1493.

[8] S. Chandra, A. Kumar, P.K. Tomar, J. Saudi Chem. Soc. 18 (2014) 437–442.

[9] A. Sharma, J. Hickman, N. Gazit, E. Rabkin, Y. Mishin, Nat. Commun. 9 (2018) 4102.

[10] A. Grano, F. Sayler, J. Smått, M. Bakker, Mater. Lett. (2013).

[11] Y.K. Moon, J.K. Lee, J.G. Kim, M.Y. Jung, J.B. Lee, S.H. Kim, Curr. Appl. Phys. 9 (2009) 928–932.

[12] S.-H. Park, H.-S. Kim, Thin Solid Films 550 (2014) 575–581.

[13] J. Lee, J. Kim, T. Hyeon, Adv. Mater. 18 (2006) 2073–2094.

[14] C. Baerlocher, L. McCusker, D. Olson, Atlas of Zeolite Framework Types, 2007.

[15] N. Stock, S. Biswas, Chem. Rev. 112 (2012) 933–969.

[16] M. Eddaoudi, J. Kim, N. Rosi, D. Vodak, J. Wachter, M. O'Keeffe, O.M. Yaghi, Science 295 (2002) 469–72.

[17] C. Rösler, R. a. Fischer, CrystEngComm 17 (2015) 199–217.

[18] J. Liu, L. Chen, H. Cui, J. Zhang, L. Zhang, C.-Y. Su, Chem. Soc. Rev. 43 (2014) 6011–6061.

[19] A. Phan, C.J. Doonan, F.J. Uribe-Romo, C.B. Knobler, M. O'Keeffe, O.M. Yaghi, Acc. Chem. Res. 43 (2010) 58–67.

[20] I. McCue, E. Benn, B. Gaskey, J. Erlebacher, Annu. Rev. Mater. Res. 46 (2016) 263–286.

[21] H.-J.H. Qiu, J.J.L. Kang, P. Liu, A. Hirata, T. Fujita, M.W. Chen, J. Power Sources 247 (2014) 896–905.

[22] B.C.C.B. Tappan, S.A.A.S. Steiner, E.P.P. Luther, Angew. Chem. Int. Ed. Engl. 49 (2010) 4544–65.

[23] Y. Ding, M. Chen, MRS Bull. 34 (2009) 569–576.

[24] E.M. Bringa, J.D. Monk, A. Caro, A. Misra, L. Zepeda-Ruiz, M. Duchaineau, F. Abraham, M. Nastasi, S.T. Picraux, Y.Q. Wang, D. Farkas, Nano Lett. 12 (2012) 3351–3355.

[25] X. Gao, X. Pei, D.W. Gardner, C.S. Diercks, S. Lee, B. Rungtaweevoranit, M.S. Prevot, C. Zhu, S. Fakra, R. Maboudian, Adv. Mater. 31 (2019) 1–9.

[26] G.C. Rybicki, J. Appl. Phys. 78 (1995).

[27] M. A. Capano, R. J. Trew, MRS Bull. 22 (1997) 19–23.

[28] W.J. Choyke, G. Pensl, MRS Bull. 22 (1997) 25–29.

[29] B.-J. Lee, M.I. Baskes, H. Kim, Y.K. Cho, (n.d.).

[30] B.-J.B. Lee, J.J.W. Lee, Calphad 29 (2005) 7–16.

[31] K.-H.H.K. Kang, T. Eun, M.M.-C.C.M. Jun, B.-J.J.B. Lee, J. Cryst. Growth 389 (2014) 120–133.

[32] L. Hozer, Y.-M. Chiang, J. Mater. Res. 11 (1996) 2346–2357.

[33] M. Baskes, Phys. Rev. B (1992).

[34] B.B.-J. Lee, Calphad 31 (2007) 95–104.

[35] J. Tersoff, Phys. Rev. B 49 (1994) 16349–16352.

[36] R. Devanathan, T. de la Rubia, W. Weber, J. Nucl. Mater. (1998).

[37] P. Erhart, K. Albe, Phys. Rev. B 71 (2005) 35211.

[38] V. Fock, Zeitschrift For Phys. 61 (1930) 126–148.

[39] D. Hartree, … W.H. the R.S. of L., undefined 1935, 149 (1935) 210–231.

[40] J.C. Slater, Phys. Rev. 35 (1930) 210–211.

[41] J.C. Slater, Phys. Rev. 81 (1951) 385–390.

[42] J. Thijssen, (2007).

[43] P. Hohenberg, W. Kohn, Phys. Rev. 136 (1964) B864–B871.

[44] E. Polak, G. Ribiere, Rev. Française d'informatique Rech. Opérationnelle. Série Rouge 3 (1969) 35–43.

[45] J. Nocedal, S.J. Wright, eds., Numerical Optimization, New York, n.d.

[46] R.H. Byrd, J.C. Gilbert, J. Nocedal, Math. Program. 89 (2000) 149–185.

[47] J.D. Gale, A.L. Rohl, Mol. Simul. 29 (2003) 291–341.

[48] D. Frenkel, B. Smit, Understanding Molecular Simulation : From Algorithms to Applications, n.d.

[49] R. Ferrando, J. Jellinek, R.L. Johnston, Chem. Rev. 108 (2008) 845–910.

[50] G. Meetham, M. Van de Voorde, (2000).

[51] A. Vita, G. Cristiano, C. Italiano, L. Pino, S. Specchia, Appl. Catal. B Environ. 162 (2015) 551–563.

[52] K. Sato, K. Kawano, A. Ito, Y. Takita, K. Nagaoka, ChemSusChem 3 (2010) 1364–1366.

[53] H. Inokawa, T. Ichikawa, H. Miyaoka, Appl. Catal. A Gen. 491 (2015) 184–188.

[54] H.C. Yu, X.Y. Huang, F.H. Lei, X.C. Tan, Y.C. Wei, H. Li, Electrochim. Acta 141 (2014) 45–50.

[55] W. Qu, L. Zhang, G. Chen, Biosens. Bioelectron. 42 (2013) 430–433.

[56] J. Lif, M. Skoglundh, L. Löwendahl, Appl. Catal. A Gen. 228 (2002) 145–154.

[57] J. Sehested, J.A.P. Gelten, S. Helveg, Appl. Catal. A Gen. 309 (2006) 237–246.

[58] J. Perelaer, P.J. Smith, D. Mager, D. Soltman, S.K. Volkman, V. Subramanian, J.G. Korvink, U.S. Schubert, J. Mater. Chem. 20 (2010) 8446.

[59] J.R. Weertman, C. Koch, Process. Prop. Appl. (Norwich William Andrew Publ. Chap 1 (2002).

[60] J.H. Li, X.D. Dai, S.H. Liang, K.P. Tai, Y. Kong, B.X. Liu, Phys. Rep. 455 (2008) 1–134.

[61] Y. Mishin, M.J. Mehl, D.A. Papaconstantopoulos, A.F. Voter, J.D. Kress, Phys. Rev. B - Condens. Matter Mater. Phys. 63 (2001) 2241061–22410616.

[62] R.A. Johnson, Phys. Rev. B 39 (1989) 12554–12559.

[63] G. Bonny, D. Terentyev, R.C. Pasianot, S. Poncé, A. Bakaev, Model. Simul. Mater. Sci. Eng. 19 (2011) 085008.

[64] S. Plimpton, J. Comput. Phys. 117 (1995) 1–19.

[65] G. Kresse, J. Furthmüller, Phys. Rev. B 54 (1996) 169.

[66] P. Janthon, S.M. Kozlov, F. Viñes, J. Limtrakul, F. Illas, J. Chem. Theory Comput. 9 (2013) 1631–1640.

[67] J.D. Gale, J. Chem. Soc. Faraday Trans. 93 (1997) 629–637.

[68] J.D. Gale, A.L. Rohl, Mol. Simul. 29 (2003) 291–341.

[69] G. Simmons, H. Wang, (1971).

[70] A.P. Sutton, J. Chen, Philos. Mag. Lett. 61 (1990) 139–146.

[71] M.I.M. Baskes, Phys. Rev. B 46 (1992) 2727–2742.

[72] R.W. Smith, G.S. Was, Phys. Rev. B 40 (1989) 10322–10336.

[73] F. Abe, T. Tanabe, Zeitschrift Fuer Met. 76 (1985) 420–425.

[74] L. Kaufman, Calphad 1 (1977) 1.

[75] E.E. Lahteenkorva, J.T. Lenkkeri, J. Phys. F Met. Phys. 11 (1981) 767–773.

[76] B.H. Rabin, W.D. Swank, R.N. Wright, Nucl. Eng. Des. 262 (2013) 72–80.

[77] A.J. Logsdail, N.J. Cookson, S.L. Horswell, Z.W. Wang, Z.Y. Li, R.L. Johnston, J. Phys. Chem. C 114 (2010) 21247–21251.

[78] Y. Mishin, M. Asta, J. Li, Acta Mater. 58 (2010) 1117–1151.

[79] A. Jain, Y. Shin, K.A. Persson, Nat. Rev. Mater. 1 (2016) 15004.

[80] D.W. Boukhvalov, D.R. Dreyer, C.W. Bielawski, Y.W. Son, ChemCatChem 4 (2012) 1844–1849.

[81] F. Wang, C. Di Valentin, G. Pacchioni, J. Phys. Chem. C 115 (2011) 8345–8353.

[82] M. Jaidann, S. Roy, H. Abou-Rachid, L.S. Lussier, J. Hazard. Mater. 176 (2010) 165–173.

[83] R. Demichelis, B. Civalleri, M. Ferrabone, R. Dovesi, in: Int. J. Quantum Chem., 2010, pp. 406–415.

[84] C.-R. Zhang, Z.-J. Liu, Y.-H. Chen, H.-S. Chen, Y.-Z. Wu, W. Feng, D.-B. Wang, Curr. Appl. Phys. 10 (2010) 77–83.

[85] K. Burke, J. Chem. Phys. 150901 (2012) 1–9.

[86] O.A. von Lilienfeld, I. Tavernelli, U. Rothlisberger, D. Sebastiani, Phys. Rev. Lett. 93 (2004) 153004.

[87] F. Ercolessi, J.B. Adams, Europhys. Lett. 26 (1994) 583–588.

[88] D. Porezag, T. Frauenheim, T. Köhler, G. Seifert, R. Kaschner, Phys. Rev. B 51 (1995) 12947–12957.

[89] S. Rani, A.K. Agrawal, V. Rastogi, Mater. Today Proc. 5 (2018) 477–486.

[90] M. Sarvghad, S. Delkasar Maher, D. Collard, M. Tassan, G. Will, T.A. Steinberg, Energy Storage Mater. 14 (2018) 179–198.

[91] R. Sykora, M. Zetek, Procedia Eng. 100 (2015) 1424–1433.

[92] S.J. Zinkle, K.A. Terrani, L.L. Snead, Curr. Opin. Solid State Mater. Sci. 20 (2016) 401–410.

[93] B. Habibi, N. Delnavaz, RSC Adv. 6 (2016) 31797–31806.

[94] T. Odedairo, J. Ma, Y. Gu, J. Chen, X.S. Zhao, Z. Zhu, J. Mater. Chem. A 2 (2014) 1418–1428.

[95] Y. Ge, Z. Zhu, Z. Ma, D. Wang, J. Electrochem. Soc. 165 (2018) E162–E170.

[96] L. Chen, Z. Yang, B. Jha, G. Xia, J.W. Stevenson, J. Power Sources 152 (2005) 40–45.

[97] J.C.W. Mah, A. Muchtar, M.R. Somalu, M.J. Ghazali, Int. J. Hydrogen Energy 42 (2017) 9219–9229.

[98] K. McNamara, S.A.M. Tofail, Phys. Chem. Chem. Phys. 17 (2015) 27981–27995.

[99] J. García-Torres, C. Gispert, E. Gómez, E. Vallés, Phys. Chem. Chem. Phys. 17 (2015) 1630–1636.

[100] N.I. Papanicolaou, G.C. Kallinteris, G.A. Evangelakis, D.A. Papaconstantopoulos, M.J. Mehl, J. Phys. Condens. Matter 10 (1998) 10979–10990.

[101] P. Brommer, A. Kiselev, D. Schopf, P. Beck, J. Roth, H.-R. Trebin, Model. Simul. Mater. Sci. Eng. 23 (2015) 074002.

[102] Y.K. Shin, H. Kwak, C. Zou, A. V. Vasenkov, A.C.T. van Duin, J. Phys. Chem. A 116 (2012) 12163–12174.

[103] J.A. Olmos-Asar, A. Rapallo, M.M. Mariscal, Phys. Chem. Chem. Phys. 13 (2011) 6500.

[104] B. Waldher, J. Kuta, S. Chen, N. Henson, A.E. Clark, J. Comput. Chem. 31 (2010) NA-NA.

[105] L.-P. Wang, J. Chen, T. Van Voorhis, J. Chem. Theory Comput. 9 (2013) 452–460.

[106] P. Brommer, F. Gähler, Model. Simul. Mater. Sci. Eng. 15 (2007) 295–304.

[107] M. Wen, J. Li, P. Brommer, R.S. Elliott, J.P. Sethna, E.B. Tadmor, Model. Simul. Mater. Sci. Eng. 25 (2017) 1–18.

[108] L. Vanduyfhuys, S. Vandenbrande, T. Verstraelen, R. Schmid, M. Waroquier, V. Van Speybroeck, J. Comput. Chem. 36 (2015) 1015–1027.

[109] H. Fang, P. Kamakoti, J. Zang, S. Cundy, C. Paur, P.I. Ravikovitch, D.S. Sholl, J. Phys. Chem. C 116

(2012) 10692–10701.

[110] H. Fang, P. Kamakoti, P.I. Ravikovitch, M. Aronson, C. Paur, D.S. Sholl, Phys. Chem. Chem. Phys. 15 (2013) 12882.

[111] J.B. Gadhe, R.B. Gupta, AIChE Annu. Meet. Conf. Proc. 2005 (2005) 4577–4585.

[112] C.K. Ho, B.D. Iverson, Renew. Sustain. Energy Rev. 29 (2014) 835–846.

[113] F. Montero-Chacón, S. Zaghi, R. Rossi, E. García-Pérez, I. Heras-Pérez, X. Martínez, S. Oller, M. Doblaré, Finite Elem. Anal. Des. 127 (2017) 31–43.

[114] T.M. Pollock, S. Tin, J. Propuls. Power 22 (2006) 361–374.

[115] J.M. Ortiz-Roldan, A.R. Ruiz-Salvador, S. Calero, F. Montero-Chacón, E. García-Pérez, J. Segurado, I. Martin-Bragado, S. Hamad, Phys. Chem. Chem. Phys. 17 (2015) 15912–15920.

[116] G. Simonelli, R. Pasianot, E.J. Savino, MRS Proc. 291 (1992) 567.

[117] G. Kresse, J. Furthmüller, Phys. Rev. B 54 (1996) 11169–11186.

[118] J.P. Perdew, K. Burke, M. Ernzerhof, Phys. Rev. Lett. 77 (1996) 3865–3868.

[119] J.R. Davis, ASM Specialty Handbook: Nickel, Cobalt, and Their Alloys, 2000.

[120] R.W. Wieman, N. G., Weertman, J.R And Siegel, Stress Int. J. Biol. Stress 1 (1992) 185–190.

[121] M.T. Dove, Introduction to Lattice Dynamics, Cambridge University Press, 1993.

[122] J.E. Turney, E.S. Landry, A.J.H. McGaughey, C.H. Amon, Phys. Rev. B 79 (2009) 064301.

[123] G.M. Day, J. a Zeitler, W. Jones, T. Rades, P.F. Taday, J Phys Chem B 110 (2006) 447–456.

[124] M. Sprik, R.W. Impey, M.L. Klein, Phys. Rev. B 29 (1984) 4368–4374.

[125] G. Gao, K. Van Workum, J.D. Schall, J.A. Harrison, J. Phys. Condens. Matter 18 (2006) S1737–S1750.

[126] L.P. Kadanoff, J. Stat. Phys. 137 (2009) 777–797.

[127] H.M. Ledbetter, R.P. Reed, J. Phys. Chem. Ref. Data 2 (1973) 531–618.

[128] G. Martin, N. Ochoa, K. Saï, E. Hervé-Luanco, G. Cailletaud, Int. J. Solids Struct. 51 (2014) 1175–1187.

[129] J.C. Michel, H. Moulinec, P. Suquet, Int. J. Numer. Methods Eng. 52 (2001) 139–160.

[130] M.A. Groeber, M.A. Jackson, Integr. Mater. Manuf. Innov. 3 (2014) 5.

[131] A. Cruzado, B. Gan, M. Jiménez, D. Barba, K. Ostolaza, A. Linaza, J.M. Molina-aldareguia, J. Llorca, J. Segurado, Acta Mater. 98 (2015) 242–253.

[132] S.M. Corporation, Www.Specialmetals.Com 625 (2013) 1–28.

[133] A.F. Clark, Cryogenics (Guildf). 8 (1968) 282–289.

[134] Hightemp metals, (2015).

[135] Z. Wang, E. Denlinger, P. Michaleris, A.D. Stoica, D. Ma, A.M. Beese, Mater. Des. 113 (2017) 169–177.

[136] M. Wang, Y. Yin, J. Zhou, X. Ji, H. Nan, P. Xue, Y. Shi, Int. J. Adv. Manuf. Technol. 90 (2017) 3055–3066.

[137] a. Sarkar, P. Mukherjee, P. Barat, T. Jayakumar, Mahadevan S., S.K. Rai, Int. J. Mod. Phys. B 22 (2008) 3977–3985.

[138] G.K. Dey, S. Albert, D. Srivastava, M. Sundararaman, P. Mukhopadhyay, Mater. Sci. Eng. A 119 (1989) 175–184.

[139] H.K. Kohl, K. Peng, J. Nucl. Mater. 101 (1981) 243–250.

[140] G.P. Dinda, A.K. Dasgupta, J. Mazumder, Mater. Sci. Eng. A 509 (2009) 98–104.

[141] S.K. Rai, A. Kumar, V. Shankar, T. Jayakumar, K.B.S. Rao, B. Raj, Scr. Mater. 51 (2004) 59–63.

[142] F.J. Xu, Y.H. Lv, B.S. Xu, Y.X. Liu, F.Y. Shu, P. He, Mater. Des. 45 (2013) 446–455.

[143] A. Mostafaei, Y. Behnamian, Y.L. Krimer, E.L. Stevens, J.L. Luo, M. Chmielus, Mater. Des. 111 (2016) 482–491.

[144] Ö. Özgün, H. Özkan Gülsoy, R. Yilmaz, F. Findik, J. Alloys Compd. 546 (2013) 192–207.

[145] G. Guo, H. Wang, Phys. Rev. B 62 (2000) 5136–5143.

[146] C. Kittel, R.W. Hellwarth, Phys. Today 10 (1957) 43–44.

[147] D.R. Lide, CRC Press (1990) 2324.

[148] W. Luc, F. Jiao, Acc. Chem. Res. 49 (2016) 1351–1358.

[149] J.M. Thomas, Nat. Catal. 1 (2018) 2–5.

[150] Z. Ma, T. Kyotani, A. Tomita, Chem. Commun. (2000) 2365–2366.

[151] A.S. Nugraha, G. Lambard, J. Na, M.S.A. Hossain, T. Asahi, W. Chaikittisilp, Y. Yamauchi, J. Mater. Chem. A 8 (2020) 13532–13540.

[152] T. Roussel, A. Didion, R.J.M. Pellenq, R. Gadiou, C. Bichara, C. Vix-Guterl, J. Phys. Chem. C 111 (2007) 15863–15876.

[153] T. Roussel, J. Jagiello, R.J.M. Pellenq, M. Thommes, C. Bichara, Mol. Simul. 32 (2006) 551–555.

[154] H. Nishihara, Q.Q.-H. Yang, P.P.-X. Hou, M. Unno, S. Yamauchi, R. Saito, J.I. Paredes, A. Martínez-Alonso, J.M.D. Tascón, Y. Sato, M. Terauchi, T. Kyotani, Carbon N. Y. 47 (2009) 1220–1230.

[155] H. Nishihara, H. Fujimoto, H. Itoi, K. Nomura, H. Tanaka, M.T. Miyahara, P.A. Bonnaud, R. Miura, A. Suzuki, N. Miyamoto, N. Hatakeyama, A. Miyamoto, K. Ikeda, T. Otomo, T. Kyotani, Carbon N. Y. 129 (2018) 854–862.

[156] E. Braun, Y. Lee, S.M. Moosavi, S. Barthel, R. Mercado, I.A. Baburin, D.M. Proserpio, B. Smit, Proc. Natl. Acad. Sci. U. S. A. 115 (2018) E8116–E8124.

[157] Q. Lin, X. Bu, C. Mao, X. Zhao, K. Sasan, P. Feng, J. Am. Chem. Soc. 137 (2015) 6184–6187.

[158] P. Lee, J. Lee, H. Lee, J. Yeo, S. Hong, K.H. Nam, D. Lee, S.S. Lee, S.H. Ko, Adv. Mater. 24 (2012) 3326–3332.

[159] H. Lee, K. Kim, S.H. Kang, Y. Kwon, J.H. Kim, Y.K. Kwon, R. Ryoo, J.Y. Park, Sci. Rep. 7 (2017) 1–9.

[160] S. Plimpton, J. Comput. Phys. 117 (1995) 1–19.

[161] Y. Gan, Z. Sun, Z. Chen, J. Appl. Phys. 118 (2015) 164304-1–5.

[162] E.Z. Da Silva, G.M. Faccin, T.R. Machado, N.G. Macedo, M. De Assis, S. Maya-Johnson, J.C. Sczancoski, J. Andrés, E. Longo, M.A. San-Miguel, J. Phys. Chem. C 123 (2019) 11310–11318.

[163] R.P. Patil, D. Doan, Z.H. Aitken, S. Chen, M.T. Kiani, C.M. Barr, K. Hattar, Y.W. Zhang, X.W. Gu, Nat. Commun. 11 (2020) 1–9.

[164] D.J. Price, C.L. Brooks, J. Chem. Phys. 121 (2004) 10096–10103.

[165] S.L. Mayo, B.D. Olafson, W.A. Goddard, J. Phys. Chem. 101 (1990) 8897–8909.

[166] J.P. Jalkanen, F. Zerbetto, J. Phys. Chem. B 110 (2006) 5595–5601.

[167] K.B. Tarmyshov, F. Müller-Plathe, J. Chem. Phys. 126 (2007) 074702.

[168] D. Dubbeldam, S. Calero, D.E. Ellis, R.Q. Snurr, Mol. Simul. (2015) 1–21.

[169] L. Sarkisov, A. Harrison, Mol. Simul. 37 (2011) 1248–1257.

[170] G. Férey, C. Serre, C. Mellot-Draznieks, F. Millange, S. Surblé, J. Dutour, I. Margiolaki, Angew. Chemie Int. Ed. 43 (2004) 6296–6301.

[171] A. Sonnauer, F. Hoffmann, M. Fröba, L. Kienle, V. Duppel, M. Thommes, C. Serre, G. Férey, N. Stock, Angew. Chemie Int. Ed. 48 (2009) 3791–3794.

[172] S.S.Y. Chui, S.M.F. Lo, J.P.H. Charmant, A.G. Orpen, I.D. Williams, Science 283 (1999) 1148–50.

[173] H. Li, M. Eddaoudi, M. O'Keeffe, O.M. Yaghi, Nature 402 (1999) 276–279.

[174] S. Ma, D. Sun, M. Ambrogio, J.A. Fillinger, S. Parkin, H.C. Zhou, J. Am. Chem. Soc. 129 (2007) 1858–1859.

[175] A.C. Sudik, A.P. Côté, A.G. Wong-Foy, M. O'Keeffe, O.M. Yaghi, Angew. Chemie Int. Ed. 45 (2006) 2528–2533.

[176] D.W. Lewis, A.R. Ruiz-Salvador, A. Gómez, L.M. Rodriguez-Albelo, F.-X. Coudert, B. Slater, A.K. Cheetham, C. Mellot-Draznieks, CrystEngComm 11 (2009) 2272.

[177] N.C. Burtch, S.J. Baxter, J. Heinen, A. Bird, A. Schneemann, D. Dubbeldam, A.P. Wilkinson, Adv. Funct. Mater. (2019) 1904669–1904669.

[178] L.M. Rodriguez-Albelo, A.R. Ruiz-Salvador, A. Sampieri, D.W. Lewis, A. Gómez, B. Nohra, P. Mialane, J. Marrot, F. Sécheresse, C. Mellot-Draznieks, R. Ngo Biboum, B. Keita, L. Nadjo, A. Dolbecq, J. Am. Chem. Soc. 131 (2009) 16078–87.

[179] A.K. Kushwaha, R. Khenata, A. Bouhemadou, S. Bin-Omran, K. Haddadi, J. Electron. Mater. 46 (2017) 4109–4118.

[180] G. Simons, H. Wang, J. Gd. Res. Center.-1965.-34 (1977) 269.

[181] J. Nye, Oxford Univ. Press (1957).

[182] G.J. Leigh, J. Organomet. Chem. 471 (1994) C11–C12.

[183] G.W.C. Kaye, T.H. Laby, Math. Gaz. 10 (1921) 351.

[184] G. V. Samsonov, M.E. Straumanis, Phys. Today 21 (1968) 97–97.

[185] D. Nguyen-Manh, V. Vitek, A.P. Horsfield, Prog. Mater. Sci. 52 (2007) 255–298.

[186] J.E. Mondloch, M.J. Katz, N. Planas, D. Semrouni, L. Gagliardi, J.T. Hupp, O.K. Farha, Chem. Commun. 50 (2014) 8944–8946.

[187] P. Lightfoot, D.A. Woodcock, M.J. Maple, L.A. Villaescusa, P.A. Wright, J. Mater. Chem. 11 (2001) 212–216.

[188] T. Carey, C.C. Tang, J.A. Hriljac, P.A. Anderson, Chem. Mater. 26 (2014) 1561–1566.

[189] Z. Liu, Q. Gao, J. Chen, J. Deng, K. Lin, X. Xing, Chem. Commun. 54 (2018) 5164–5176.

[190] S.R.G. Balestra, R. Bueno-Perez, S. Hamad, D. Dubbeldam, A.R. Ruiz-Salvador, S. Calero, Chem. Mater. 28 (2016) 8296–8304.

[191] H. Fang, M.T. Dove, A.E. Phillips, Phys. Rev. B 89 (2014) 214103.

[192] L. He, F. Weniger, H. Neumann, M. Beller, Angew. Chemie Int. Ed. 55 (2016) 12582–12594.

[193] Y. Ben-Shahar, F. Scotognella, I. Kriegel, L. Moretti, G. Cerullo, E. Rabani, U. Banin, Nat. Commun. 7 (2016) 10413.

[194] C. Chmelik, J. Kärger, Chem. Soc. Rev. 39 (2010) 4864.

[195] F. Stallmach, S. Gröger, V. Künzel, J. Kärger, O.M. Yaghi, M. Hesse, U. Müller, Angew. Chemie Int. Ed. 45 (2006) 2123–2126.

[196] T.G. Grissom, C.H. Sharp, P.M. Usov, D. Troya, A.J. Morris, J.R. Morris, J. Phys. Chem. C 122 (2018) 16060–16069.

[197] P. Dutta, Appl. Therm. Eng. 124 (2017) 624–632.

[198] T. Conroy, M.N. Collins, R. Grimes, Renew. Sustain. Energy Rev. 119 (2020) 109591.

[199] Z. Fang, C. Lu, C. Guo, Y. Lu, D. Gao, Y. Ni, J. Kou, Z. Xu, P. Li, Sol. Energy Mater. Sol. Cells 134 (2015) 252–260.

[200] S. Chu, Y. Cui, N. Liu, Nat. Mater. 16 (2017) 16–22.

[201] D. Rativa, L.A. Gómez-Malagón, Sol. Energy 118 (2015) 419–425.

[202] J.M. Ortiz-Roldan, G. Esteban-Manzanares, S. Lucarini, S. Calero, J. Segurado, F. Montero-Chacón, A.R. Ruiz-Salvador, S. Hamad, Phys. Chem. Chem. Phys. 20 (2018) 18647–18656.

[203] M. Neber, H. Lee, Energy 47 (2012) 481–487.

[204] Z. Wu, C. Caliot, F. Bai, G. Flamant, Z. Wang, J. Zhang, C. Tian, Appl. Energy 87 (2010) 504–513.

[205] A.L. Avila-Marin, Sol. Energy 85 (2011) 891–910.

[206] R.A. Andrievski, Rev. Adv. Mater. Sci. 22 (2009) 1–20.

[207] H.J. Herrmann, S. Roux, in: H.J. Herrmann, S.B.T.-S.M. for the F. of D.M. Roux (Eds.), Random Mater.

Process., North-Holland, Amsterdam, 1990, pp. 159–188.

[208] R. Devanathan, T. Diaz De La Rubia, W.J. Weber, J. Nucl. Mater. 253 (1998) 47–52.

[209] B.-J. Lee, M.I. Baskes, H. Kim, Y. Koo Cho, Phys. Rev. B 64 (2001) 184102.

[210] B.-J. Lee, M.I. Baskes, Phys. Rev. B 62 (2000) 8564–8567.

[211] J. Tersoff, Phys. Rev. B 37 (1988) 6991–7000.

[212] J. Tersoff, Phys. Rev. B 39 (1989) 5566–5568.

[213] E. Schlangen, E.J. Garboczi, Eng. Fract. Mech. 57 (1997) 319–332.

[214] G. Lilliu, J.G.. van Mier, M.R.A. van Vliet, Trans. Model. Simul. 21 (1999) 515–524.

[215] A. Arslan, R. Ince, B.L. Karihaloo, J. Eng. Mech. 128 (2002) 57–65.

[216] M. Yip, Z. Li, B.-S. Liao, J.E. Bolander, Int. J. Fract. 140 (2006) 113–124.

[217] Z. Qian, G. Ye, E. Schlangen, K. van Breugel, in: Key Eng. Mater., 2011, pp. 65–68.

[218] Y. Wang, P. Mora, J. Mech. Phys. Solids 56 (2008) 3459–3474.

[219] K. Hitti, P. Laure, T. Coupez, L. Silva, M. Bernacki, Comput. Mater. Sci. 61 (2012) 224–238.

[220] F. Montero-Chacón, J. Marín-Montín, F. Medina, Comput. Mater. Sci. 90 (2014) 157–170.

[221] K. Terada, T. Miura, N. Kikuchi, Comput. Mech. 20 (1997) 331–346.

[222] A.C.E. Reid, S.A. Langer, R.C. Lua, V.R. Coffman, S.-I. Haan, R.E. García, Comput. Mater. Sci. 43 (2008) 989–999.

[223] U. Täffner, V. Carle, U. Schäfer, M.J. Hoffmann, ASM Handb. Mettallography Microstruct. 9 (2004).

[224] G.R. Sawyer, T.F. Page, J. Mater. Sci. 13 (1978) 885–904.

[225] M. Singh, J. Mater. Sci. 33 (1998) 5781–5787.

[226] M. Singh, D.R. Behrendt, Mater. Sci. Eng. A 187 (1994) 183–187.

[227] Z.P. Bažant, M.R. Tabbara, M.T. Kazemi, G. Pijaudier-Cabot, J. Eng. Mech. 116 (1990) 1686–1705.

[228] S. Song, C. Bao, Y. Ma, K. Wang, J. Eur. Ceram. Soc. 37 (2017) 2569–2574.

[229] D. Feldman, J.P. Jr, W. Choyke, L. Patrick, Phys. Rev. (1968).

[230] T.C. Chiang, J. Dumas, Y.R. Shen, Solid State Commun. 28 (1978) 173–176.

[231] M. Szabadi, P. Hess, A.J. Kellock, H. Coufal, J.E.E. Baglin, Phys. Rev. B 58 (1998) 8941–8948.

[232] X. Zhang, J.D. Comins, A.G. Every, P.R. Stoddart, W. Pang, T.E. Derry, Phys. Rev. B 58 (1998) 13677–13685.

[233] O.P. Chakrabarti, S. Ghosh, J. Mukerji, Ceram. Int. 20 (1994) 283–286.

[234] R. Ji, Y. Liu, Y. Zhang, B. Cai, X. Li, C. Zheng, J. Mech. Sci. Technol. 27 (2013) 177–183.

[235] R.S. Evans, D.L. Bourell, J.J. Beaman, M.I. Campbell, Proceeding Solid Free. Fabr. Symp. (2003) 414–422.

[236] M. Salamone, S., Karandikar, P., Marshall, A., Marchant, D., & Sennett, in: Mech. Prop. Perform. Eng. Ceram. Compos. III, 2007, pp. 101–109.

[237] J. Milhans, S. Ahzi, H. Garmestani, M.A. Khaleel, X. Sun, B.J. Koeppel, Mater. Des. 30 (2009) 1667–1673.

[238] P. Colombo, V. Sglavo, E. Pippel, J. Woltersdorf, J. Mater. Sci. 33 (1998) 2405–2412.

[239] L.L. Snead, T. Nozawa, Y. Katoh, T. Byun, 371 (2008) 329–377.

[240] A. Montoya, M.R. Rodríguez-Sánchez, J. López-Puente, D. Santana, Sol. Energy 174 (2018) 912–922.

[241] Q.W. Huang, L.H. Zhu, Mater. Lett. 59 (2005) 1732–1735.

Appendices

Appendix 1

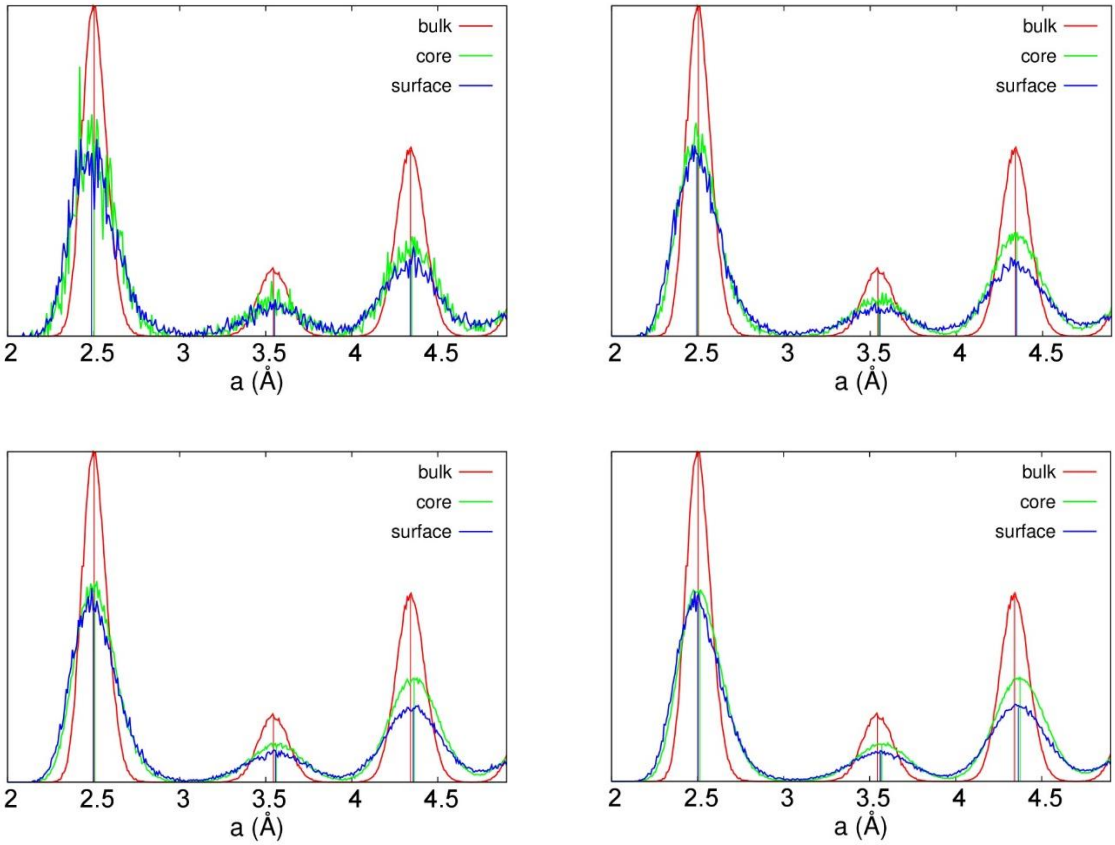

Figure A1. Ni-Ni RDFs of the core and of the outer 1nm thick layer of the Ni nanoparticles of sizes (from top to bottom) 3 nm, 5 nm, 7 nm, and 10 nm. The RDFs are obtained from the last structures of the simulations at 300 K, which accounts for the high level of noise. In order to get a better insight into how the RDFs change, a Gaussian function has been fitted to each of the peaks, and the positions of the center of the Gaussians are shown as vertical lines. The RDF of the fcc Ni bulk structure at 300 K is also shown for comparison.

Appendix 2

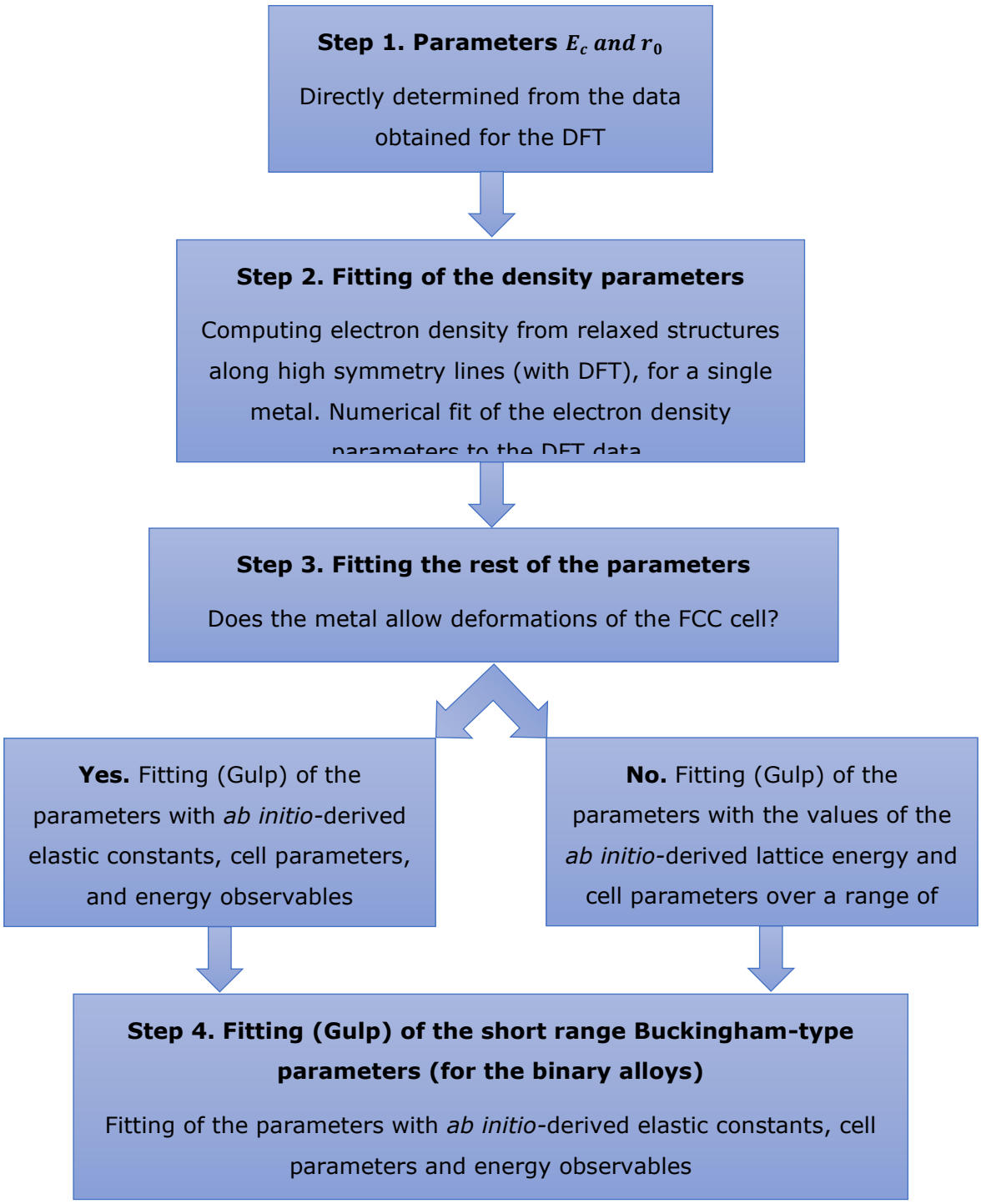

Figure A2. Algorithm developed to carry out the fitting of the potential parameters of the alloy.

Table A1. Simulated and experimental cell parameters of Inconel 625 (Ni-Cr-Mo-Fe).

Temp. (K)	Force field	Exp1	Exp2	Exp3	Exp4	Exp5
120	3.612	3.590	3.591	3.592	3.594	3.598
160	3.613	3.592	3.593	3.594	3.596	3.600
212	3.616	3.594	3.595	3.596	3.598	3.602
296	3.620	3.598	3.600	3.601	3.603	3.607
332	3.622	3.600	3.602	3.602	3.604	3.608
368	3.624	3.602	3.603	3.604	3.606	3.610
468	3.630	3.608	3.609	3.610	3.612	3.616
534	3.634	3.611	3.613	3.614	3.616	3.620
566	3.636	3.613	3.614	3.615	3.617	3.621
626	3.640	3.617	3.618	3.619	3.621	3.625
652	3.641	3.618	3.619	3.620	3.622	3.626
684	3.643	3.620	3.621	3.622	3.624	3.628
712	3.645	3.622	3.623	3.624	3.626	3.630
776	3.649	3.626	3.627	3.628	3.630	3.634
814	3.653	3.628	3.629	3.630	3.632	3.636
848	3.655	3.630	3.631	3.632	3.634	3.638
878	3.657	3.632	3.633	3.634	3.636	3.640
952	3.662	3.637	3.638	3.639	3.641	3.645
988	3.666	3.639	3.640	3.641	3.643	3.647

Table A2. Simulated monocrystalline elastic constants from MD.

T (K)	C11	C12	C44
1	248.734	176.959	127.911
100	246.141	175.832	127.686
200	240.281	172.210	124.588
300	232.955	167.911	121.833
400	225.697	163.315	116.486
500	218.018	158.131	113.255
600	209.366	152.790	109.031
700	200.877	147.152	105.793
800	192.757	141.867	100.537
900	184.796	137.665	95.306
1000	175.966	131.369	89.953

Appendix 3

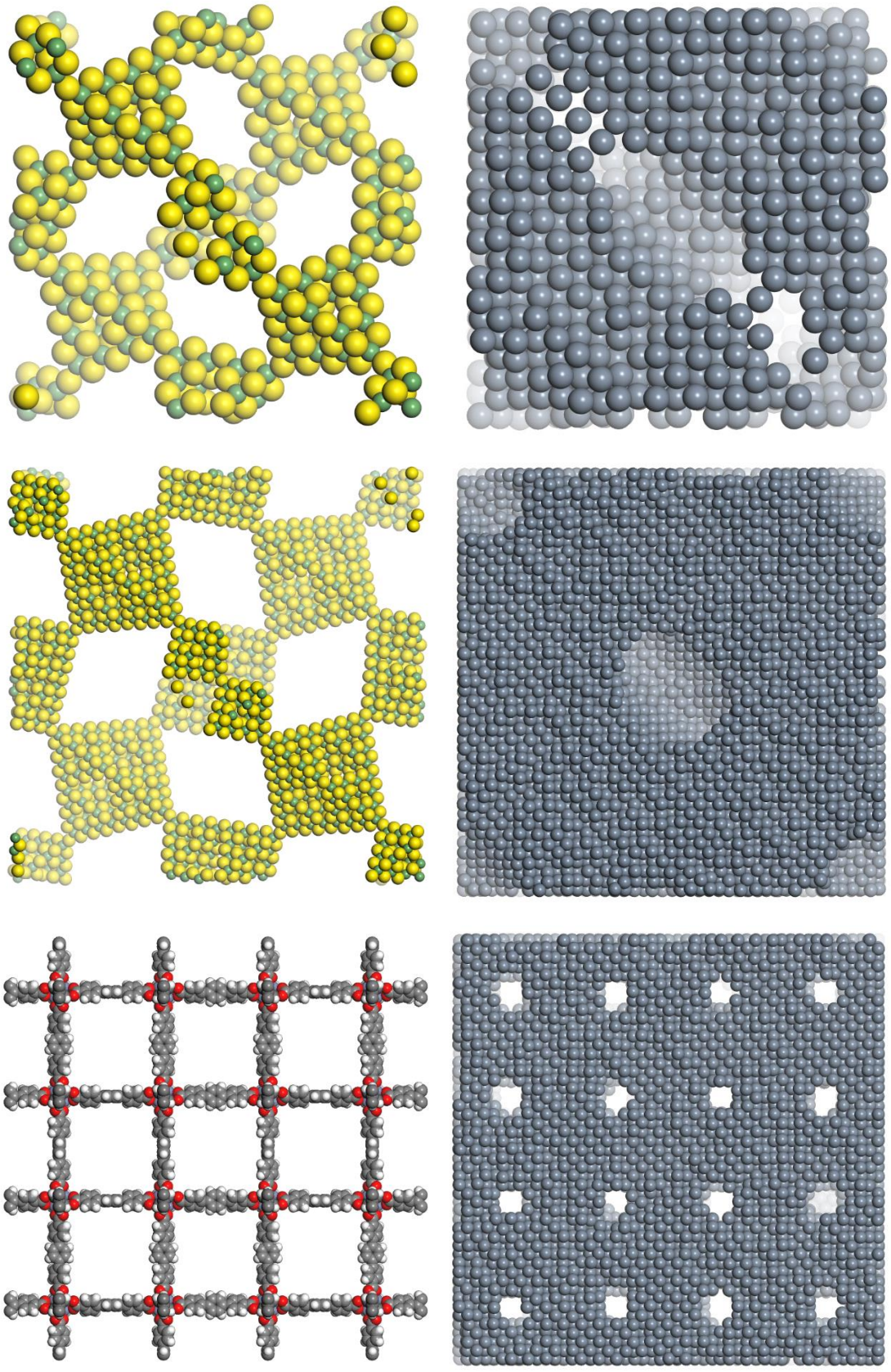

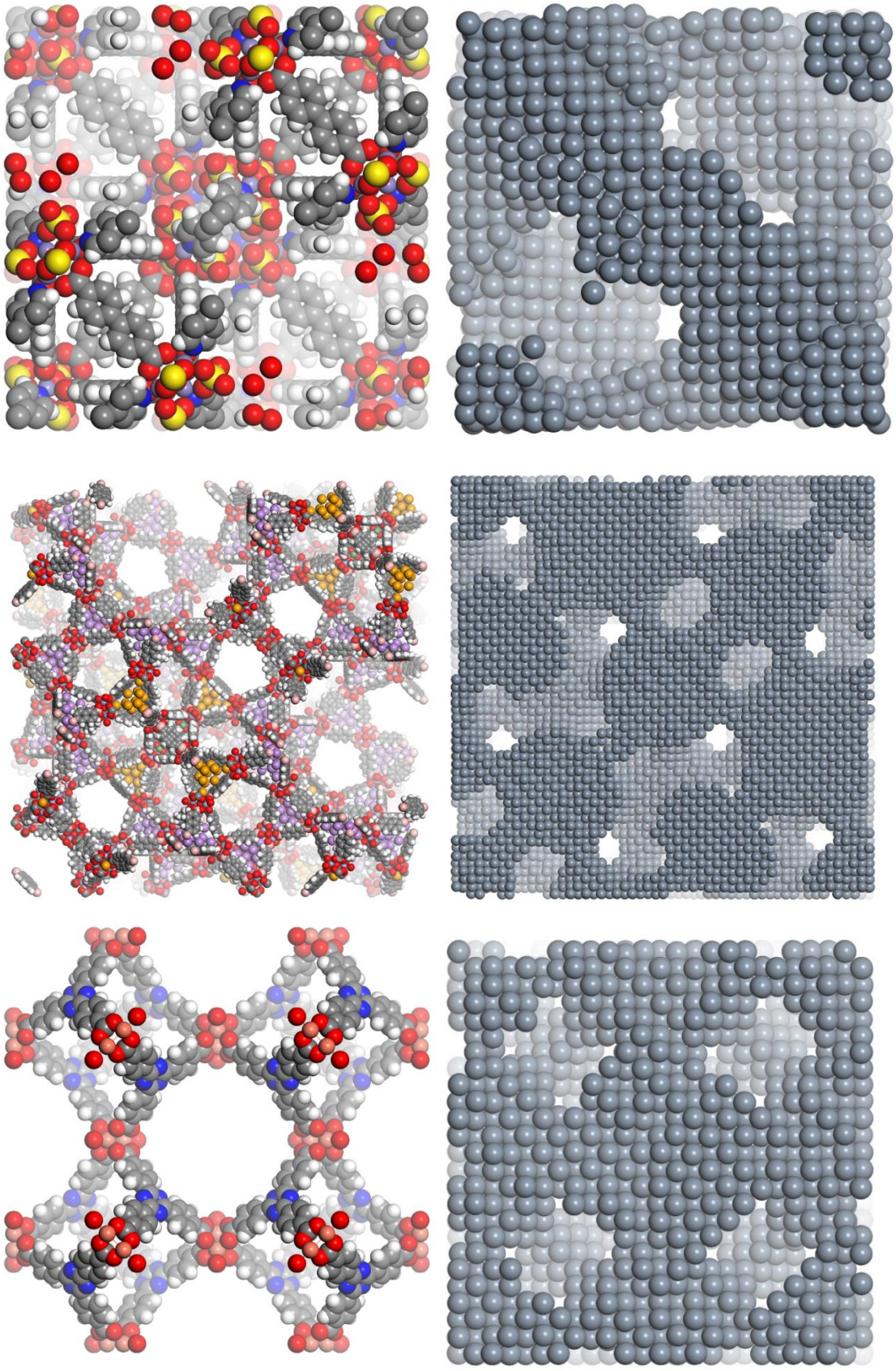

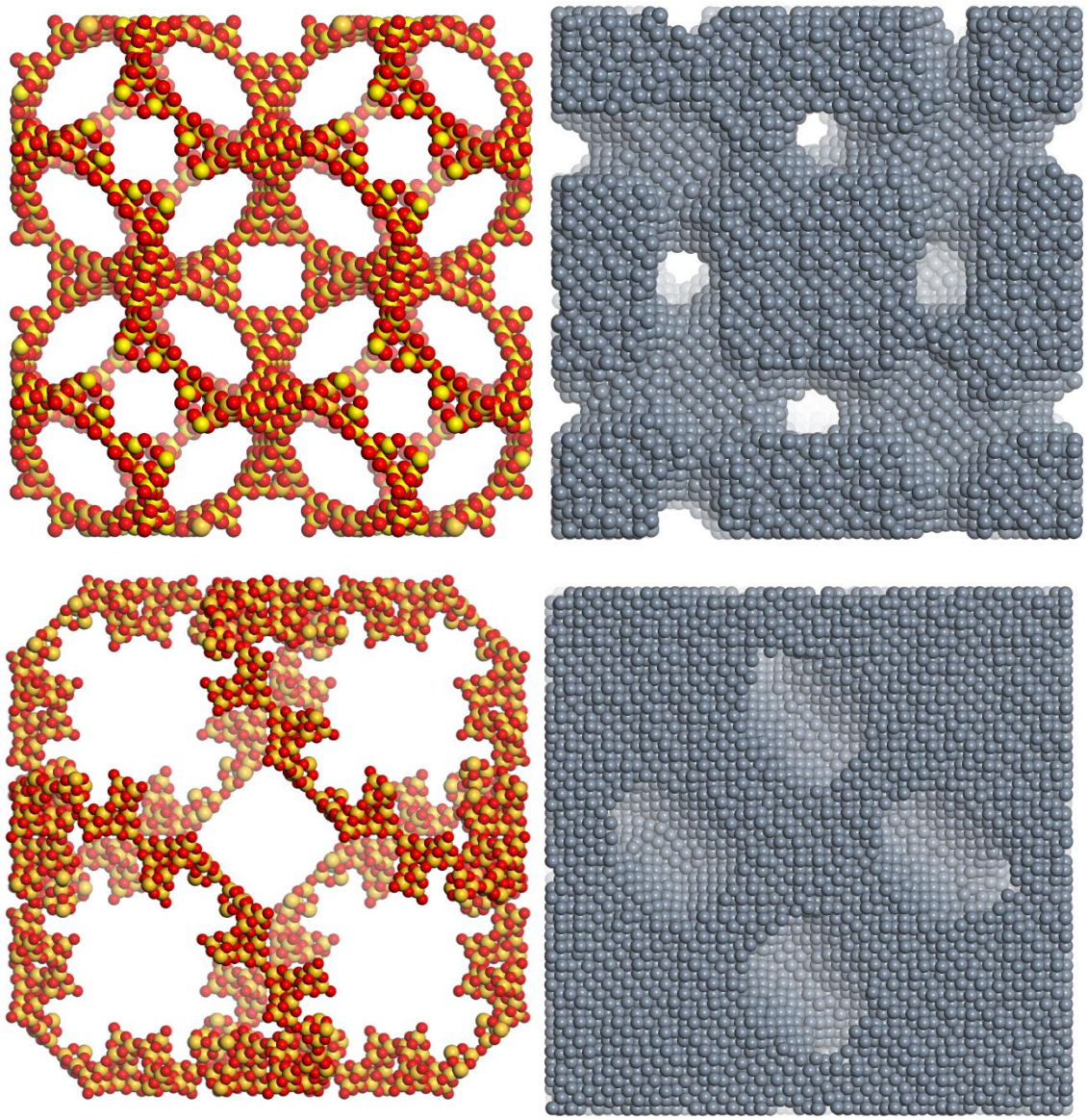

Figure A3. Templates (left) and ONMs (right) of the eight stable structures. From top to bottom: CRI-ST3, CRI-ST4, IRMOF16, MOF-500, NDC-MIL101, PCN-6P, SOD-ST3, SOD-ST4.

S4.- Empirical formula for the critical PLD of stable ONM

The critical PLD of the template structure is given by

PLDc = 2Rvdw + 7.50Ratom, according to the following scheme:

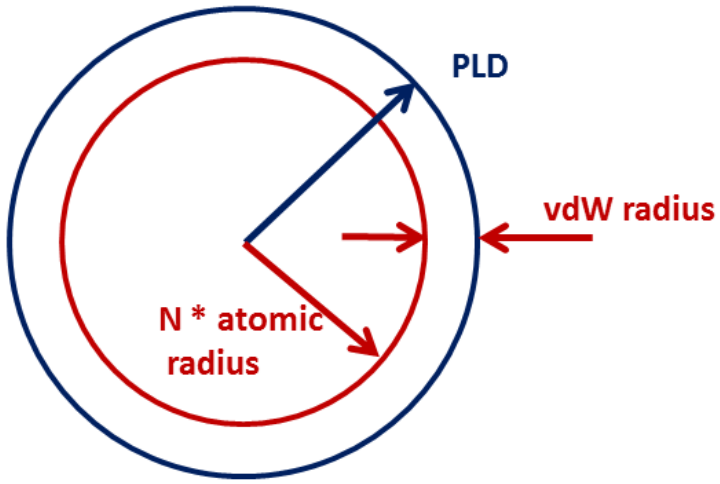

For Pt N = 7.5 was get, which also provides a Pt – Pt distance within 1 % as compared to experimental Pt structure.

Table A3.- Porosity of template MOFs and ST solids

Porosity and stability label of template MOFs and ST solids: Stability (label, unstable, medium stability, high stability), PLD (pore limiting diameter Å), LCD (large cavity diameter Å), AccHVF (accessible Helium void fraction), AccFreeVolFrac (accessible freee volume fraction), AccSAVolum (accessible volumetric surface area m^2/cm^3).

Solid	Stability	PLD	LCD	AccHVF	AccFreeVolfrac	AccSAvolum
MOF simulated						
MOF_HKUST	Unst.	6.37	12.74	0.685	0.634	1645.98
MOF_IRMOF1	Unst.	7.80	15.03	0.820	0.771	2047.65
MOF_IRMOF16	Med.	17.10	25.19	0.933	0.904	1245.96
MOF_MIL100	Unst.	8.61	26.38	0.680	0.653	1320.32
MOF_MIL101	Unst.	13.31	33.3	0.787	0.747	1154.75
MOF_NDC_MIL101	Med.	15.31	40.97	0.883	0.765	1028.82
MOF_MOF500	Unst.	10.12	19.56	0.762	0.714	1574.68
MOF_PCN6p	Med.	14.76	22.86	0.872	0.849	1499.37
Supertetrahedra simulated						
ST_cri_GeS2_ST2	Unst.	7.40	9.54	0.883	0.719	2039
ST_cri_GeS2_ST3	High	18.34	22.83	0.933	0.866	1057.49
ST_cri_GeS2_ST4	High	42.96	52.27	0.965	0.935	438.99
ST_SOD_GeS2_ST2	Unst.	7.58	18.17	0.895	0.765	1666.82
ST_SOD_GeS2_ST3	Med.	18.59	40.72	0.942	0.885	900.92
ST_SOD_GeS2_ST4	High	42.24	86.77	0.969	0.944	387.06
MOF experimental						
MOF_BUT12	High	16.94	23.93	0.799	0.759	1204.19
MOF_MOF808	High	10.80	17.77	0.716	0.698	1599.88
MOF_PCN777	High	28.17	33.52	0.894	0.882	729.84

Appendix 4

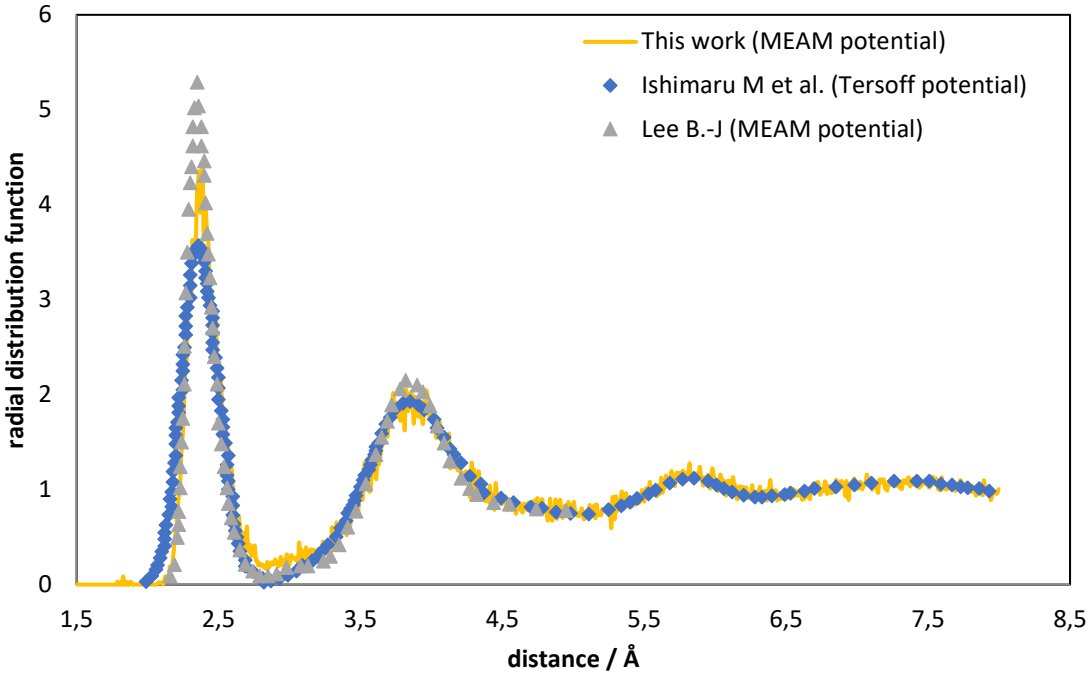

Figure A4. Calculated silicon – silicon radial distribution functions for a-Si at 500 K

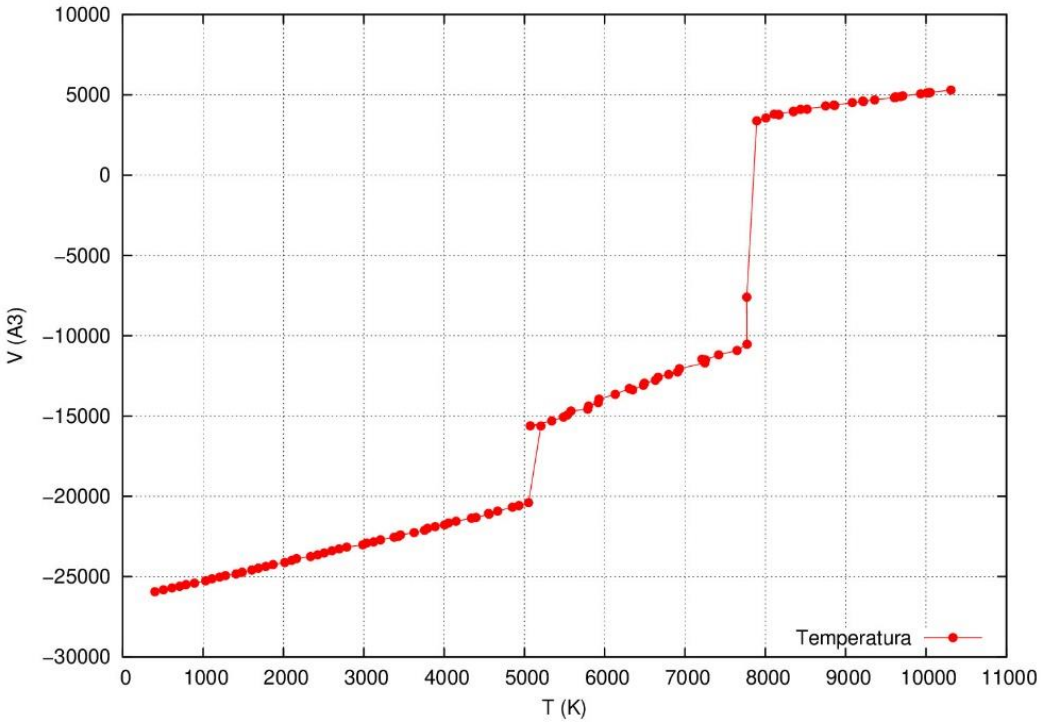

Figure A5. Volume – Temperature to observe the overestimated melting point of the systems.

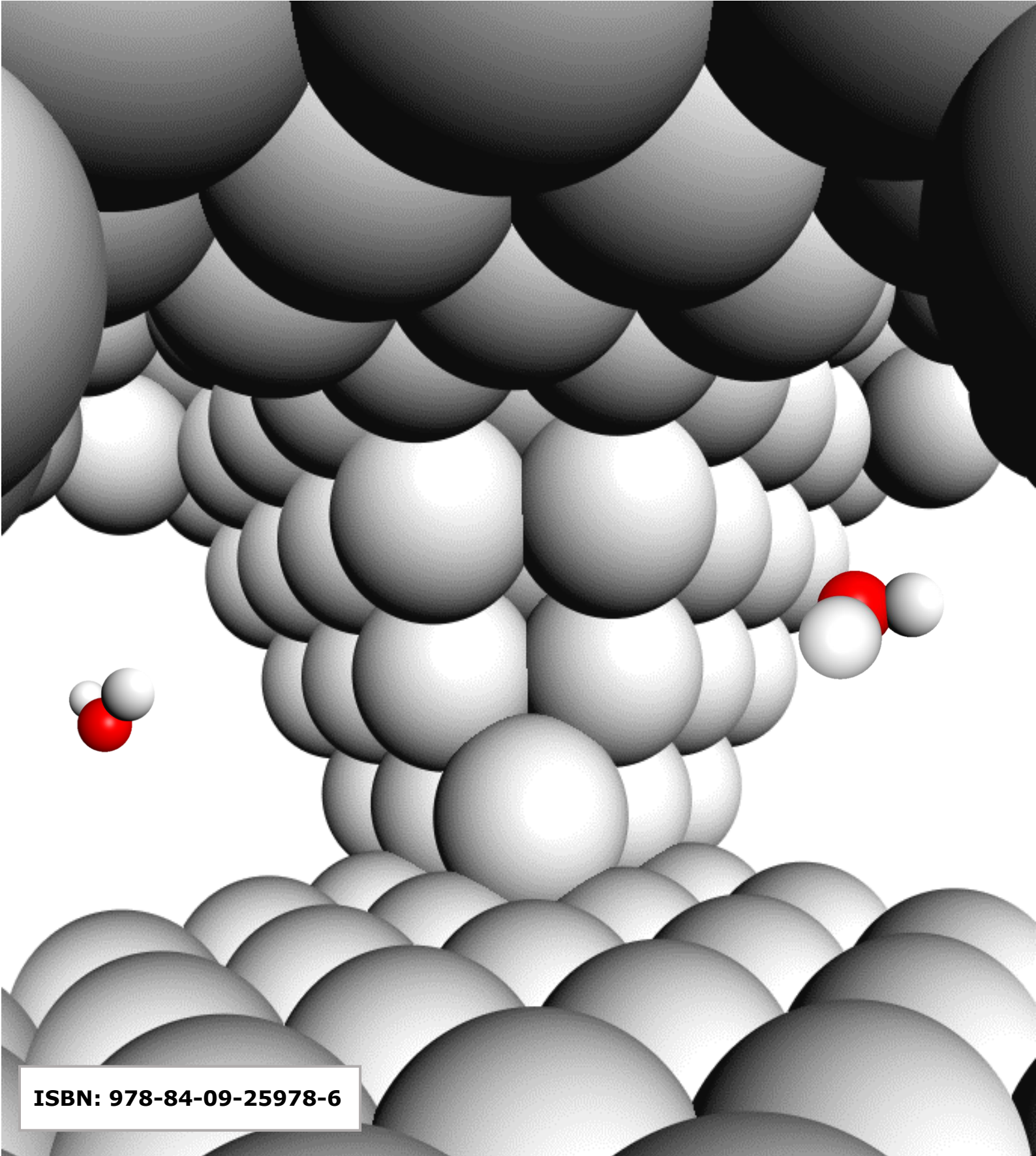

ISBN: 978-84-09-25978-6

UNIVERSIDAD PABLO DE OLAVIDE SEVILLA